STUDIES ON CERTAIN VANADIUM PENTOXIDE BASED SEMICONDUCTING OXIDE GLASSES EXHIBITING MAJORITY CHARGE CARRIER REVERSAL PHENOMENON

A Thesis Submitted
in Partial Fulfilment of the Requirements
for the Award of the Degree of
Doctor of Philosophy

by

Bachaspatimayum Indrajit Sharma

DEPARTMENT OF PHYSICS
INDIAN INSTITUTE OF TECHNOLOGY GUWAHATI
GUWAHATI-781039
INDIA

JUNE, 2002

Dedicated
to
my Parents

Certificate

It is certified that the work contained in the thesis entitled " STUDIES ON CERTAIN VANADIUM PENTOXIDE BASED SEMICONDUCTING OXIDE GLASSES EXHIBITING MAJORITY CHARGE CARRIER REVERSAL PHENOMENON" by B. Indrajit Sharma, a student in the Department of Physics, Indian Institute of Technology, Guwahati for the award of degree of Doctor of Philosophy has been carried out under my supervision and that this work has not been submitted elsewhere for a degree.

27 June, 2002

Dr. A. Srinivasan
Department of Physics
Indian Institute of Technology Guwahati
Guwahati - 781039

Acknowledgements

I would like to express my profound gratitude to Dr. A. Srinivasan for introducing me to the world of glass science. I am grateful to him for his continuous guidance, tiredless effort, constant encouragement and keen interest in the progress of my work. I will try my level best to follow his advice and imbibe his qualities in future. It gives me a great sense of pride and joy for having been associated with his research group over the past few years.

I am grateful to Dr. Sasanka Ghosh for his constant encouragement and support during my Ph.D work. My thanks are due to all faculty members of Physics Department for their help and suggestions.

It is my pleasure to acknowledge with gratitude the help received from Mr. Sidananda Sarma, Mr. Lokesh Chakraborty, Mr. Chandan Borgohain, Mr. Madan Deka and Mr. Dibakar Deb during my research work.

My sincere thanks to Dr. P. S. Robi, Mr. Ramananda Das and Mr. Rituraj Saikia for their help with the microhardness measurements. I would like to thank all the members of the mechanical workshop, IIT Guwahati for their help in fabrication of various mechanical parts required for the experimental set up.

I am very much fortunate to have Mr. Akhyaya Kumar Pattanaik as my senior and his expertise in the field of Differential Scanning Calorimeter was a great help to me. I thank him for the many discussions I had with him. I take this opportunity to thank all my colleagues in the Department of Physics, Chemistry and Humanities & Social Sciences, IIT Guwahati.

I am pleased to express my cordial gratitude to my friend Ms. Bina Devi and also to all my friends, both in and outside the campus for their affection and encouragement.

I am grateful to the office staff of the Academic Section for the smooth and efficient processing of all official matter.

I thank the Indian Institute of Technology, Guwahati for providing me an institute fellowship to pursue my Ph. D work.

I am deeply indebted to my parents, brothers and sisters for their constant encouragement and moral support.

Last but not the least my sincere thanks are due to all those persons who helped me in whatever form during my stay at IIT Guwahati, whom I may have inadvertently forgotten to mention in this acknowledgement.

27/06/2002

B. Indrajit sharma

Preface

Vanadium pentoxide (V_2O_5) based glasses form an important class of amorphous semiconductors. V_2O_5 based glasses are normally n-type semiconductors. The possibility of obtaining p-type semiconductors in some V_2O_5 based ternary glasses has been pointed out in the literature. After a careful study of the glass-forming region of known V_2O_5 based glass systems coupled with thermoelectric power (TEP) measurements, three glass systems, namely, $xV_2O_5.20SnO.(80\text{-}x)TeO_2$ glasses ($18 \leq x \leq 50$), $xV_2O_5.40CaO.(60\text{-}x)P_2O_5$ glasses ($10 \leq x \leq 30$) and $xV_2O_5.40CaO.(60\text{-}x)B_2O_3$ glasses ($10 \leq x \leq 30$) were identified for the present investigations. These three glass systems exhibit a reversal in the carrier type from n-type to p-type when the composition x was systematically varied.

Bulk glass samples belonging to the three glass systems were prepared by melt quenching technique. The as-quenched samples were characterized using X-ray diffraction technique, TEP measurement and differential scanning calorimeter (DSC). TEP measurements revealed that the carrier reversal occurs near 23 mol % V_2O_5 in V_2O_5-SnO-TeO_2 glasses. In V_2O_5-CaO-P_2O_5 and V_2O_5-CaO-B_2O_3 glasses, the carrier reversal was observed at 20 mol % V_2O_5. The ratio of vanadium ions, $\frac{V^{5+}}{V^{4+}}$ in various glass compositions was estimated by iodometric titration. Density of the glass samples was measured using Archimedes' principle. Optical band gap of the glasses was determined using a spectrophotometer. Microhardness of the various glass compositions was measured using a Vicker's microhardness tester. DSC studies were under taken to investigate the non-isothermal behaviour of the glass samples. The d.c. electrical conductivity of the glasses was measured between 100 K and 480 K, in order to

understand the conduction mechanism in these glasses. All the experimental data were analysed using existing theoretical formalisms. The thesis is arranged in six chapters.

Chapter I serves as a brief introduction to glasses and the contents of this thesis. The motivation behind the thesis work is briefly stated at the end of this chapter.

Chapter II discusses the experimental techniques used in the present investigations. The basic principle and the theory behind the experiments, the experimental set up and the measurement / estimation procedure leading to the determination of the physical properties are discussed here.

In chapter III, the experimental studies on V_2O_5-SnO-TeO_2 glasses are presented. It starts with a review of earlier work done on V_2O_5-SnO-TeO_2 glasses followed by the present studies. The occurrence of the carrier reversal in $xV_2O_5.20SnO.(80-x)TeO_2$ glasses ($18 \leq x \leq 50$) is first established using TEP and vanadium ion ratio. The variation of density, optical band gap and microhardness of the glass samples as a function of V_2O_5 mol % is then discussed within the frame of existing models. Results of DSC studies and dc electrical conductivity studies are then presented. The salient results of the present studies on $xV_2O_5.20SnO.(80-x)TeO_2$ glasses are summarised at the end.

Chapter IV and V are devoted to the study on V_2O_5-CaO-P_2O_5 and V_2O_5-CaO-B_2O_3 glass systems, respectively. These chapters are arranged in the same sequence as chapter III.

Chapter VI is the concluding chapter which attempts to generalise the results obtained on V_2O_5 based glasses. Possibilities of future work in this area are also pointed out.

References cited in the thesis are listed at the end of the thesis.

Contents

Chapter 1

Introduction

A glass is an X-ray amorphous solid which exhibits the glass transition. Glass transition is defined as that phenomenon in which a solid amorphous phase exhibits a more or less sudden change in the derivative thermodynamic properties such as heat capacity and expansion coefficient, from crystal-like to liquid-like values [1]. Glasses are generally obtained by freezing in supercooled liquids at a sufficiently rapid rate to avoid crystallization. This process leads to the formation of a non-crystalline solid where the structural disorder of the liquid is retained in the solid state. Glasses can be prepared by methods other than the melt quenching technique such as physical vapour deposition, application of intense shock waves, mechanical alloying, etc. [2].

From the fundamental standpoint, glasses present a challenge to the study of solids which lack the spatial periodicity (long-range order) typical of a crystal. The description of these structures meets with well-known difficulties and the interpretation of the experimental results is seriously hampered [1, 3, 4]. The scientific interest in these materials is due to the complexities in understanding the nature of the amorphous state and the realization that they are low cost material with potential applications [1, 5].

Short-range order, which is a fundamental characteristic of a solid is a result of the chemical bonding between the atoms in the solid. Since amorphous materials do not possess long-range order, the chemical bonding in these materials is directly responsible for most of their properties. Just as in crystalline materials, the bonding in amorphous materials could be covalent (eg., As_2Se_3, V_2O_5-TeO_2), ionic (eg., KNO_3-$Ca(NO_3)_2$, BeF_2), metallic (eg., Zr-Cu, Ni-Nb), Van der Waals' (eg., isopentane, ortho-terphenyl) or

hydrogen bond (eg., H_2O, $KHSO_4$) [1, 3]. V_2O_5 based oxide glasses form an important class of amorphous semiconductors. Semiconducting behaviour in oxide glasses was first observed in the V_2O_5-P_2O_5 system [6]. Glassy semiconductors containing transition metal oxides such as V_2O_5 and a wide range of oxides like P_2O_5, B_2O_3, TeO_2, GeO_2, CaO, SrO etc., have attracted lot of attention [7, 8, 9] for their interesting electrical properties. Of these, the V_2O_5-TeO_2 glasses have been given special attention [10, 11, 12, 13] due to their high electrical conductivity. The presence of vanadium in two valence states [i.e., V^{4+} and V^{5+}] in glasses containing V_2O_5 influences the electrical conduction mechanism in these glasses [14, 15]. The electrical conduction in these glasses is attributed to hopping of electrons from an ion of low valence state (V^{4+}) transition metal to an ion of high valence state (V^{5+}). The process can also be regarded as the migration of a polaron [16]. Our present knowledge of the conduction mechanism at different temperature regions and related properties of the oxide semiconducting glasses is far from being satisfactory [17].

1.1. Phenomenology of glass transition

The nature of the glass transition is very complex and even now is poorly understood. When a liquid is cooled, one of the following two events may occur. Either crystallization may take place at the melting point T_m or else the liquid will become "supercooled" for temperatures below T_m. The supercooled liquid becomes more and more viscous with decreasing temperature, and may ultimately attain viscosity values typical of a solid. At this stage the supercooled is said to have gone to the glassy state. The changes occurring in a liquid as it is cooled can be understood readily by monitoring the change in its

volume as a function of temperature as illustrated in figure 1.1. The crystallization process is manifested by an abrupt change in volume at T_m, where as glass formation is characterized by a gradual change in slope [1, 18, 19]. The region over which the change of slope occurs is termed the glass transition region. Similar behaviour is also exhibited by other thermodynamic variables such as entropy S and enthalpy H.

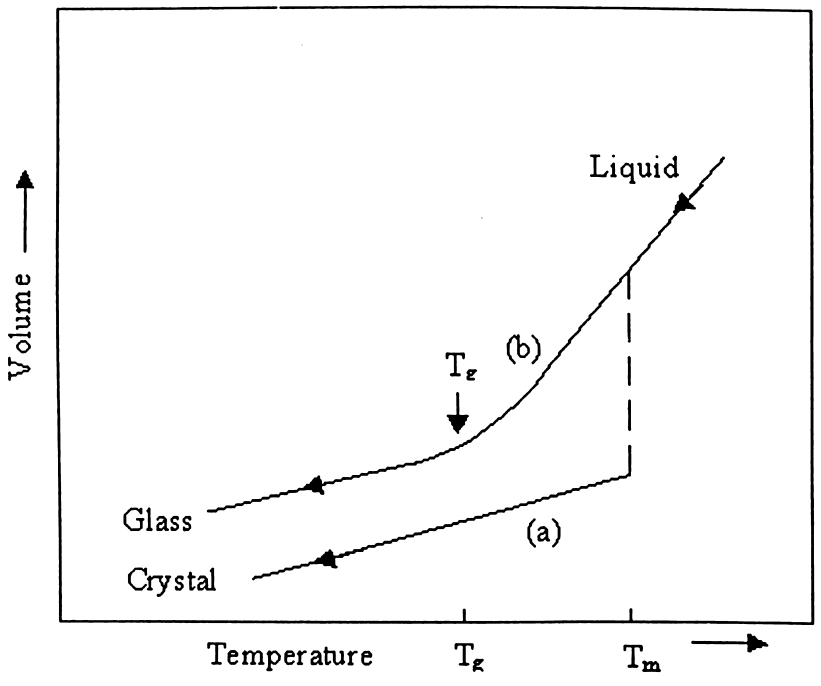

Figure 1.1: Volume change in a liquid forming (a) a crystal (b) or a glass.

The definition of the order of a phase transition in the Ehrenfest scheme is the order of the lowest derivative of Gibbs free energy (G), which shows a discontinuity at the transition point [20]. For liquid-crystal transition at solidification (or melting) temperature T_m, the volume $V = \left(\frac{\partial G}{\partial P}\right)_T$ is discontinuous. Hence liquid-crystal transition is a first order transition. But in liquid-glass transition, the thermodynamic variables such as V, S, H are continuous and the quantities which are the second order derivative of

Gibbs free energy such as thermal expansion $\alpha_T = \frac{1}{V}\left(\frac{\partial^2 G}{\partial P \partial T}\right)$, compressibility $K_T = -\frac{1}{V}\left(\frac{\partial^2 G}{\partial P^2}\right)_T$ and heat capacity $C_P = -T\left(\frac{\partial^2 G}{\partial T^2}\right)_P$ are discontinuous. Hence the glass transition is a manifestation of a second order phase transition [1].

The heat capacity C_{Pg} of the glass is different from the heat capacity C_{Pl} of the supercooled liquid. The excess heat capacity ΔC_p at the glass transition is then defined as the difference between the specific heat values of the glass and supercooled liquid. Angell [21] proposed that glasses exhibiting a small ΔC_p at T_g show a strong resistance to structural degradation in the liquid state. He termed such glasses as "strong". On the other hand, glasses exhibiting large ΔC_p at T_g were termed as "fragile". Fragility is a term used to characterise and quantify the anomalous non-Arrhenius transport behaviour which develops in most glass forming liquids as they approach the glass transition [21]. A small ΔC_p is correlated with minimum fragility. The correlation of minimum fragility with minimum ΔC_p is expected from the Adam-Gibbs equation [22],

$$\eta = \eta_o e^{\frac{C}{TS_c}} \qquad (1.1)$$

where η is the viscosity, and η_o and C are constants. The parameter S_c is the configurational entropy and is given by the expression,

$$S_c = \int_{T_k}^{T} \left(\frac{\Delta C_p}{T}\right) dT$$

where T_k is the Kauzmann temperature (T_k is the temperature at which S_c extrapolates to

zero [23]). When ΔC_p is very small, S_c is almost temperature independent and the Adam-Gibbs equation becomes the Arhenius equation. The slope of the Arrhenius plot [i.e., ln(η) versus 1/T plot] is minimum when ΔC_p is minimum. The minimum Arrhenius slope is then related to minimum fragility.

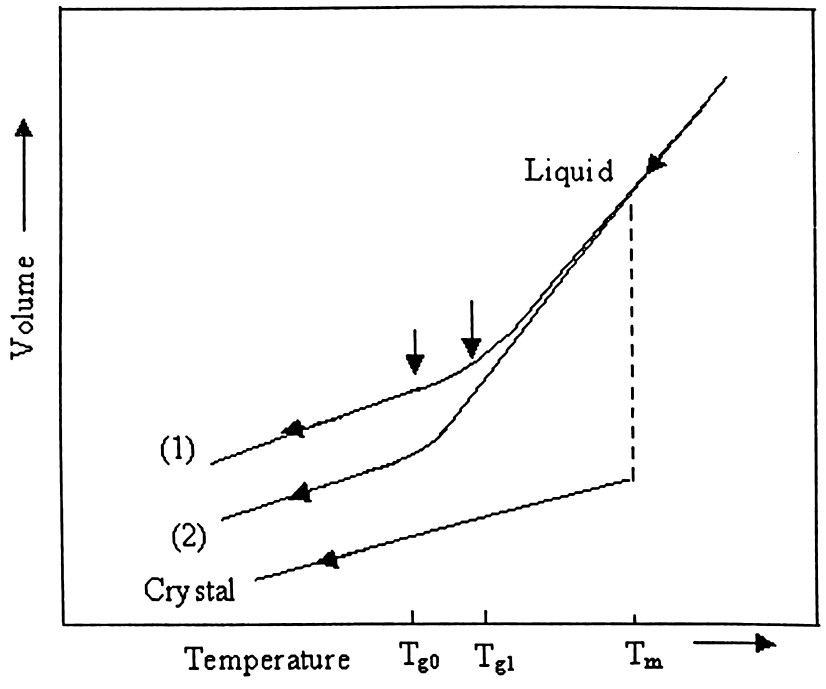

Figure 1.2: Variation in T_g of a glass forming liquid with cooling rate. Curve (2) corresponds to a slower cooling rate than curve (1).

The glass transition temperature T_g depends on the rate of cooling of the supercooled liquid [1]. The slower the rate of cooling, the larger is the region for which the liquid may be supercooled and hence lower is the glass transition temperature (figure 1.2). Thus the glass transition temperature of a particular material is not an intrinsic property. Instead, it is dependent on its thermal history of the material. T_g is related to the cooling rate q by,

$$q = q_o e^{-\frac{1}{c}\left(\frac{1}{T_g} - \frac{1}{T_m}\right)} \qquad (1.2)$$

where c and q_o are constants [24]. The experimentally measured value of T_g is not unique. The value of T_g depends on the time scale of the experiment used to observe it.

A parameter K_g, characterising the tendency to form glass, which involves the glass transition temperature T_g, the melting temperature T_m and the crystallization temperature T_c has been defined by Hruby [25] as,

$$K_g = \frac{T_c - T_g}{T_m - T_c} \qquad (1.3)$$

If $(T_c - T_g)$ is large and $(T_m - T_c)$ is small, the inhibition to the process of nucleation and crystallization is strong and consequently the glass forming tendency of the system is high.

T_g is also defined in terms of the experimental time scale as that temperature at which the liquid attains a certain viscosity η, characteristic of a solid ($\sim 10^{13}$ poise). The viscosity of glass forming liquids changes very rapidly in the region of the glass transition temperature. A wide variety of theories of relaxation have been developed based on distinct microscopic models [26]. An empirical relation for viscosity at equilibrium was given by the Vogel-Fulcher-Tamman equation, which is expressed as,

$$\eta = \eta_0 \exp\left[\frac{A}{T - T_0}\right] \qquad (1.4)$$

where η_o, A and T_o are constants. This equation is the most successful expression for describing $\eta(T)$ [27, 28].

1.2. Structure of glass

Knowledge of the structural arrangements of atoms in a solid substance is an essential prerequisite to a detailed understanding of its physical and chemical properties. This is as true for amorphous solids as for crystalline materials [3, 29]. The structure of a crystalline solid is solved once the structure within the unit cell is known. This unit cell is the fundamental building block of the structure and repeating it in a periodic fashion in space generates the structure of the crystal as a whole. Such a procedure is impossible for a non-periodic (amorphous) solid for which the unit cell may be regarded as being infinite in extent. The structure of many amorphous solids is in fact not totally random at least on certain length scales. There may be a considerable degree of local ordering despite the lack of periodicity [30] in amorphous materials. Therefore a length scale may be arbitrarily defined, which separates microscopic structure from macroscopic structure [31]. Diffraction methods (X-ray, neutron or electron) can be used to determine the frequency with which the given interatomic distances occur in a glass sample. With diffraction data it is possible to get information on the second and third co-ordination spheres around an atom and the interconnection of the regions of short-range order [32].

Molecular spectroscopic methods, especially infrared and Raman spectroscopy have been found to be extremely valuable methods of structural exploration in heteronuclear glass forming systems [33]. The structural information obtained primarily relate to the short-range order regions and their symmetry. Spectroscopic methods based on atomic properties that are influenced by the chemical environment such as photoelectron spectroscopy, nuclear magnetic resonance spectroscopy, Mossbauer spectroscopy and absorption spectroscopy can also be used for structural elucidation.

Hoppe et al [34] have studied the structure of glassy V_2O_5 (prepared by rapid quenching) using X-ray diffraction technique. They reported that the glassy V_2O_5 is formed of VO_4, VO_5, and VO_6 units. They pointed out that the vanadium atom had a mean number of 4.8 oxygen neighbours. The V-V coordination number of about five indicated that the structural units are most likely linked by V-O-V bridges. Crystalline P_2O_5 exists in three polymorphic forms; hexagonal, orthorhombic and tetragonal [35]. The phosphorous-oxygen tetrahedron in each of these forms is different. The melts of all the three crystalline forms of P_2O_5 can easily be supercooled to form glass. P_2O_5 glass structure depends on the polymorphic form of the P_2O_5 used as starting material. Figure 1.3(a) shows a structure of P_2O_5 glass [29]. V_2O_5 glass structure is more complicated, but has many similarities with the P_2O_5 glass structure [36]. The structure of crystalline B_2O_3 consists of infinite chains of BO_3 triangles. All such triangles are connected by B-O at all three corners to form a completely linked network. Krogh-Moe [37] and Griscom [38] have reviewed the structure of B_2O_3 glass. Nuclear magnetic resonance studies confirm the existence of plane trigonal BO_3 units in B_2O_3 glass [39, 40]. The BO_3 units join to form either boroxol rings or boroxol groups. These units are connected by oxygen atoms in such a manner that the B-O-B angle becomes variable with the possibility of the twisting out of the plane of the boroxol group. Figure 1.3(b) and 1.3(c) show the B_2O_3 glass and boroxol ring structures respectively. Wright et al [41] have summarized the structural information available on vanadate glasses. On the basis of the neutron diffraction study of V_2O_5 -P_2O_5, V_2O_5-BaO and V_2O_5-PbO glasses, they noted that there is a vanadate network composed of interconnected distorted trigonal bipyramids. According to them, the vanadium-oxygen co-ordination polyhedron and the linkage

between them appeared to be less regular than those observed in phosphate glasses and crystals.

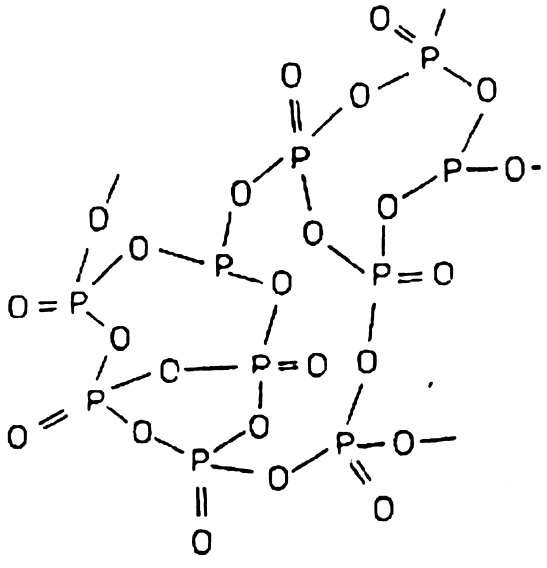

(a)

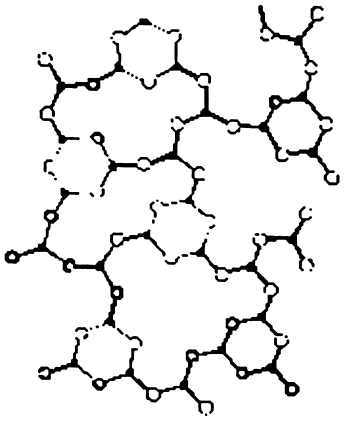

(b)

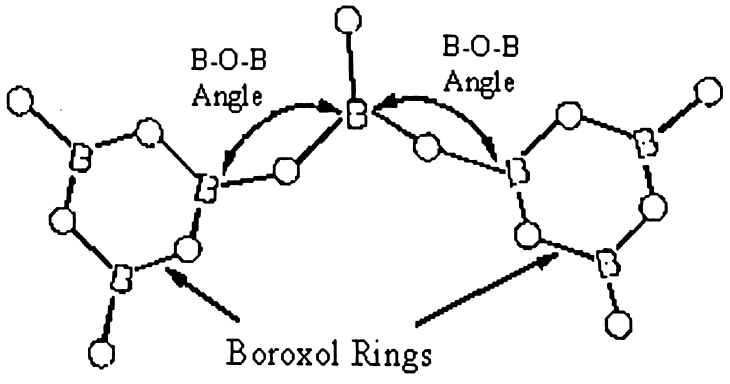

(c)

Figure 1.3: (a) P_2O_5 glass (b) B_2O_3 glass (filled circles are Boron atoms and open circles are oxygen atoms), and (c) Boroxol ring structures

Diffraction patterns of covalent glasses

In the diffraction pattern of covalent glasses, there is a common feature widely observed which is regarded as a signature of the medium range order (MRO) called "first sharp diffraction peak" (FSDP) or "prepeak" [42, 43]. The FSDP occurs at a value of scattering

vector $\vec{k}$ in the range 1-2 Å^{-1} in the structure factor $\vec{S}(\vec{k})$ of covalent network glasses [44]. FSDP exhibits anomalous behaviour as a function of temperature, pressure and composition. The FSDP intensity generally increases with increasing temperature [45] and decreases with increasing pressure [46]. The intensity of FSDP decreases markedly upon the addition of modifiers atoms. This behaviour has been observed in alkali silicate glasses upon the addition of Na_2O [47], in Ag-Ge-Se and Ag_2S-GeS_2 glasses [48] and Ag_2O-B_2O_3 [42, 49] glasses. A number of suggestions have put forward to understand the structural origin of the FSDP [30, 50]. Elliot proposed that the FSDP is a prepeak in the concentration-concentration structure factor, arising from the chemical ordering of interstitial voids around cation-centred clusters in the structure [42, 43].

A second peak is observed in the $\vec{S}(\vec{k})$ of network glasses at $\vec{k}$ ~2.91 Å^{-1} such as in the case of v-SiO_2 [44] which behaves in the same anomalous fashion as the FSDP. This second peak is termed as the "second sharp diffraction peak"(SSDP). The behaviour and structural origin of SSDP can be understood in exactly the same manner as the FSDP, namely as a prepeak originating from the chemical ordering of voids in the structure [51]. Elliot's intuitive model has been successful in explaining the temperature dependence of the intensity of FSDP and SSDP of As_2Se_3 glass [52] and the pressure dependence of intensity of FSDP of $GeSe_2$ glass [46].

Network models

The first really successful attempt to categorize materials into glass formers and non-glass formers was made by Zachariasen in 1932 [53]. Zachariasen proposed that those materials, which are most likely to form glasses, would have an internal energy only slightly larger in the amorphous state as compared to the crystalline state. The

internal energy of a solid is related to its structure [27]. Zachariasen assumed that the oxygen polyhedra found in oxide crystals would also occur in glasses, the only difference being the relative orientation of the polyhedra should be variable in glasses giving rise to a non-periodic structure [54]. The difference in structure of glassy and crystalline forms of a hypothetical two-dimensional oxide, say, A_2O_3 is shown in figure 1.4(a) and 1.4(b) [18].

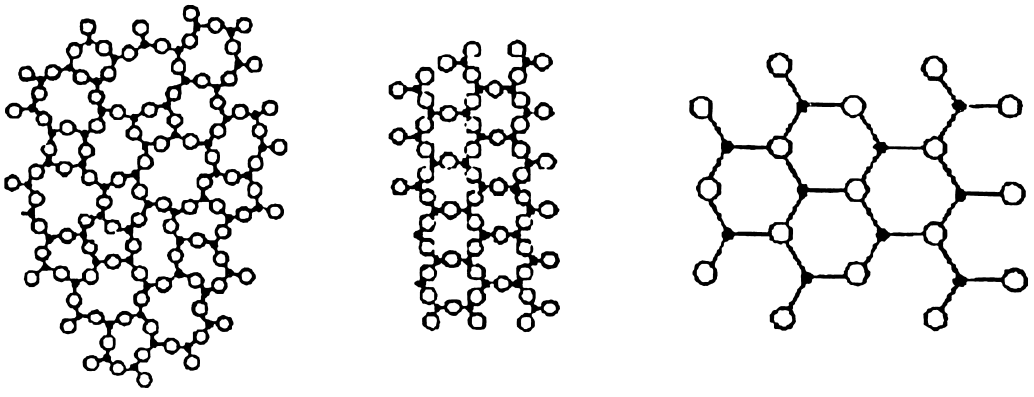

(a) (b) (c)

Figure 1.4: Atomic structural representation of (a) a A_2O_3 glass, and (b) a A_2O_3 crystal. (c) Structural representation of a hypothetical crystalline compound AO (Filled circles are cations).

Thus, both the crystalline and the glassy forms are composed of AO_3 triangles joined to each other at corners, except that the glassy form has disorder introduced by changes in the A-O-A bond angles and A-O bond length. The triangles or O-A-O angles themselves need not be deformed much. It is easy to realize why the compound AO {figure 1.4(c)} would not form a glass [2, 18, 55]. If the cation polyhedra were triangles then the co-ordination of A around O would also be 3. This clearly would imply sharing of oxygen by 3A's and hence an ordering would follow simply from topological

restraints. Zachariasen therefore defined a glass as a substance that can form extended three-dimensional networks lacking periodicity with energy content comparable with that of the corresponding crystal network. Accordingly, he laid down four cycles for glass formation in compound A_mO_n:

1. An oxygen atom is linked to no more than two atoms of A.
2. The oxygen coordination around A is small say 3 or 4.
3. The cation polyhedra share corners not edges or faces.
4. At least three corners are shared.

Thus oxides, of the type AO and A_2O should not and indeed do not form glasses. The rules are satisfied for oxides of the form A_2O_3 provided the oxygens form triangles around each A atom, and for oxides of the form AO_2 and A_2O_5 if the oxygens form tetrahedra. Subsequently Zachariasen modified the original rules to take account of complex glasses, which contained non-glass forming oxides in addition. The modified rules are

1M. A high proportion of (network forming) cations are surrounded by oxygen tetrahedra or triangles

2M. The oxygen polyhedra only share corners with each other.

3M. Some oxygen atoms are linked to only two cations and do not form additional bonds with any other cations.

These rules imply that oxide glasses must contain substantial proportions of glass forming cations or other cations, which can substitute isomorphously (eg. Al^{3-}, Si^{4+}). Any other cations (eg. Na^{+}) present are termed network modifiers [56] since they disrupt the otherwise perfectly connected continuous random network. Consider the case of addition

of Na_2O to SiO_2. The action of the modifier is to break up the continuous silica network by introducing "dangling or nonbridging oxygens". This process is shown in figure 1.5 and is not limited to silica glass only, but can occur in other oxide systems [57, 58] as well. The nonbridging oxygens carry a single negative charge and are compensated by a Na^+ ion nearby. The chemical formula of an oxide glass may be written as A_mB_nO where m and n may not be integers. A represents network forming cation and B is the network modifying cation. An interesting intermediate class of oxides including TeO_2, MoO_3, Bi_2O_3, Al_2O_3, Ga_2O_3 and V_2O_5 do not by themselves form glasses but will do so when mixed with other (modifier) oxides [59, 60].

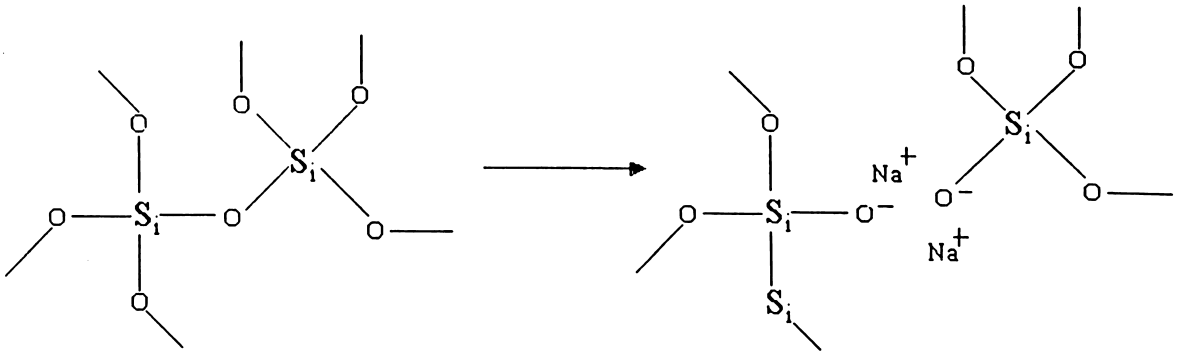

Figure 1.5: Schematic illustration of the effect of the addition of alkali oxide (eg. Na_2O) to silica . Each molecule of Na_2O added converts a bridging oxygen into two nonbridging oxygens (negatively charged).

Recent results show that network glasses possess well-defined medium range order (MRO) thus limiting the usefulness of the above simple model. The presence of MRO would imply that the relative orientation of neighbouring tetrahedra is probably non-random, which is contrary to the above model [43]. The random covalent network model [61] and the chemically ordered network model [62] have been proposed to understand the nature bonding in binary alloy systems such as A_xB_{1-x} , where A and B are

in columns a and b of the periodic table. They have coordination number $n_a = (8-a)$ and $n_b = (8-b)$ as given by the 8-N rule (neglecting the effect of any coordination defects such as dangling bonds). In general, A-A, A-B and B-B bonds can coexist in an alloy with an arbitrary composition and the two models can describe the distribution of such bonds.

1.3. Electrical properties of amorphous semiconductors

In an amorphous structure there is no concept of a reciprocal space. So one cannot write the electron states in the form of bands [63]. An appropriate description, however, would be to use the density of states N(E) defined such that N(E)dE is the number of electron states per unit volume having energies between E and E+dE. The integral of the density of states function along with the occupancy factor f(E) within energy band levels, gives the total number 'n' of carriers within the band. For instance, for the conduction band

$$n = \int_{E_c}^{\infty} N(E) f(E) dE \qquad (1.5)$$

The total conductivity σ may then be written as,

$$\sigma = -e \int_{0}^{\infty} N(E) \beta(E) k_B T \frac{\partial f(E)}{\partial E} dE \qquad (1.6)$$

where e is the electronic charge and k_B is the Boltzmann constant, β(E) is the mobility of the charge carrier having an energy E. There are essentially two different models that describe for the density of states in amorphous solids. The fundamental premise of both the models is the tailing of states into the gap at both the valence and conduction edges (E_V and E_C, also called mobility edges) because of structural fluctuations such as bond

angle distortion.

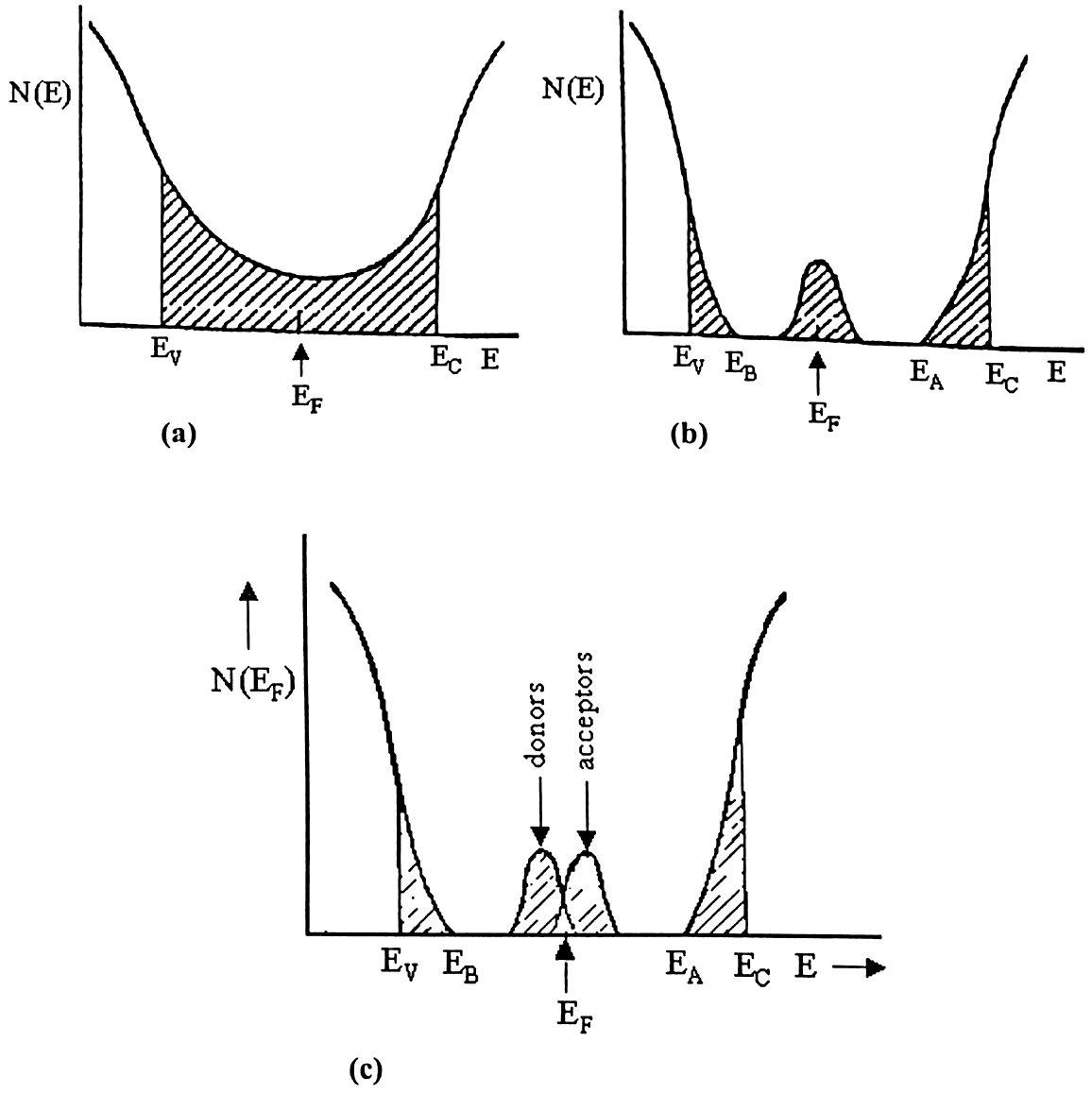

Figure 1.6: (a) The CFO model, showing tailing of states causing overlap. (b) The Davis-Mott model, showing a band of compensated levels near the middle of the gap. (c) The Marshall-Owen model.

In the extreme case of the Cohen-Fritzsche-Ovshinsky (CFO) model [64], the tailing is so pronounced that they actually overlap in the mid-gap {figure 1.6(a)}. It may be shown that the electron states lying within the mobility gap are the ones that are

localized. The Fermi energy is essentially pinned in the mid-gap. By pinning, one means that the zero temperature position of the Fermi level does not shift much with the addition of a few donors or acceptors. The primary objection to the CFO model is the high transparency observed in the chalcogenite glasses below a well-defined absorption edge, which implies the presence of an actual gap within the tailing.

The second model is due to the Davis and Mott [65], which suggests that the tailing of the localized states is confined to a fraction of an electron volt within the gap, along with a band of compensated levels originating from the defects such as dangling bonds and vacancies near the mid-gap {figure 1.6(b)}. A dangling bond means a broken or unsatisfied bond. The true gap in the Davis Mott model is (E_A-E_B). In a modification by Marshall and Owen [66], the mid-gap band was split into donor and acceptor bands with a little overlap {figure 1.6(c)}. The Fermi level was assumed to be pinned in the mid-gap in this model too.

1.3.1. d.c. electrical properties

D.C. electrical conductivity of an amorphous semiconductor can be understood from the Davis and Mott model. According to Davis and Mott, there are three regions of conductivity of an amorphous semiconductor. They are (i) extended state conduction (ii) conduction in band tails and (iii) conduction in localized states at the Fermi energy E_F.

Case (i): Conduction in extended states means the conduction of electrons excited above E_C or holes below E_V {figure 1.6(b)}. Conductivity in extended states is characterized by large mobility, which according to Mott [61] decreases sharply at the mobility edge E_C (or E_V). This conductivity has the form,

$$\sigma \cong \sigma_1 e^{\left[-\frac{E_C - E_F}{2k_B T}\right]} \qquad (1.7)$$

where the pre-exponential factor σ_1 is given by,

$$\sigma_1 = e N(E_C) k_B T \mu_C \qquad (1.8)$$

where $N(E_C)$ is the density of states at the mobility edge E_C and μ_C is the mobility.

Case (ii): Conduction in band tails is thermally assisted by emission or absorption of a phonon and involves a hopping energy ΔW_H, in addition to the activation energy $(E-E_F)$ required to raise the electron to the appropriate localized state at E. This conductivity has the form,

$$\sigma \cong \sigma_2 e^{[-(E_A - E_F + \Delta W_H)/k_B T]} \qquad (1.9)$$

where σ_2 is a pre-exponential factor and E_A is the energy of the conduction band tail.

Case (iii): In the third region, the electrical conductivity is thermally activated. The conduction in this region has different conduction mechanism in high and low temperature regions. In the high temperature region, the conductivity is characterized by the Mott-Austin relation [14, 67],

$$\sigma T = \sigma_o e^{-\frac{W}{k_B T}} \qquad (1.10)$$

where, W is the activation energy for conduction, T is the absolute temperature and k_B is the Boltzmann constant. The pre-exponential factor σ_o could be expressed as,

$$\sigma_o = \frac{C_V(1-C_V)\upsilon_o e^2}{Rk_B} e^{(-2\alpha R)} \qquad (1.11)$$

where ν_0 ($\sim 10^{13}$ sec^{-1}) is the optical phonon frequency, C_V the ratio of the amount of reduced transition metal ion to that of total transition metal ion (eg., in the case of vanadium, $C_V = V^{4+}/V^{tot}$, where $V^{tot} = V^{4+}+V^{5+}$), and α is the rate of wave function decay for the hopping electron. R the average spacing between transition metal ions which is given by $R=\left(\frac{1}{N}\right)^{\frac{1}{3}}$ where N is the state density of transition metal ions. In the case of vanadate glasses, N is calculated from the empirical relation,

$$N=2\left[\text{density}\times\left(\frac{\text{wt.}V_2O_5}{\text{Mol.wt.}V_2O_5}\right)N_A\right] \qquad (1.12)$$

where $wt.V_2O_5$ = wt. percentage of V_2O_5, $Mol.wt.V_2O_5$ = molecular weight of V_2O_5 and N_A = Avogadro's number. Figure 1.7 shows the plot of $\ln(\sigma T)$ vs 1000/T for a typical V_2O_5 based semiconducting glass. The linearity of the conductivity data in high temperature region shows that equation (1.10) is valid for this part of the data. The conduction is attributed to hopping of electron from high valence state V^{5+} to low valence state V^{4+} in vanadate glasses.

According to the Mott-Austin model the conduction in high temperature region is termed as small polaron hopping (SPH) conduction. If the rate of wave function decay α is very small such that the exponential factor in equation (1.11) $e^{(-2\alpha R)} \rightarrow 1$, then the conduction mechanism is referred to as adiabatic SPH conduction. This varied SPH mechanisms can also be explained from the value of polaron bandwidth j using Holstein proposal [68]. The temperature dependence of the d.c. conductivity according to Holstein is given by,

$$\sigma = \left(\frac{\pi e^2 j^2}{R h k_B T}\right)\left[\left(\frac{\pi}{W k_B T}\right)\frac{\sinh\left(\frac{h\upsilon_o}{2k_B T}\right)}{\left(\frac{h\upsilon_o}{2k_B T}\right)}\right]^{\frac{1}{2}} e^{-\left(\frac{W+GW_P}{2k_B T}\right)} \qquad (1.13)$$

where $W = W_H + W_D/2$ for $T > \theta_D/2$, W_D is the distortion energy and W_H is the hopping energy (equal to half the binding energy of small polaron W_P) and θ_D is the Debye temperature. W_P is estimated from the relation, $W_P = 2W_H$. The parameter G is given by,

$$G = [\tanh(h\nu_o/2k_B T)]/(h\nu_o/2k_B T) \qquad (1.14)$$

The polaron bandwidth j must satisfy one of the following condition, namely,

$$j > \Phi = (2k_B T W_H/\pi)^{1/4}(h\nu_o/\pi)^{1/2} \quad \text{(adiabatic)} \qquad (1.15)$$

$$j < \Phi = (2k_B T W_H/\pi)^{1/4}(h\nu_o/\pi)^{1/2} \quad \text{(non-adiabatic)} \qquad (1.16)$$

The mobility μ for adiabatic and non-adiabatic SPH regime can be obtained by the following equations [69].

$$\mu = \left(\frac{\upsilon_o e R^2}{k_B T}\right) e^{-\frac{W_H}{k_B T}} \quad \text{(adiabatic)} \qquad (1.17)$$

$$\mu = \left(\frac{e R^2}{k_B T}\right)\left(\frac{2\pi}{h}\right)\left(\frac{\pi}{4W_H k_B T}\right)^{\frac{1}{2}} j^2 e^{-\frac{W}{k_B T}} \quad \text{(non-adiabatic)} \qquad (1.18)$$

Carrier concentration N_C is related to the mobility μ by the relation,

$$\sigma = N_C e \mu \qquad (1.19)$$

N_C can be calculated by substituting the value of μ calculated from equation (1.17) and (1.18) in (1.19).

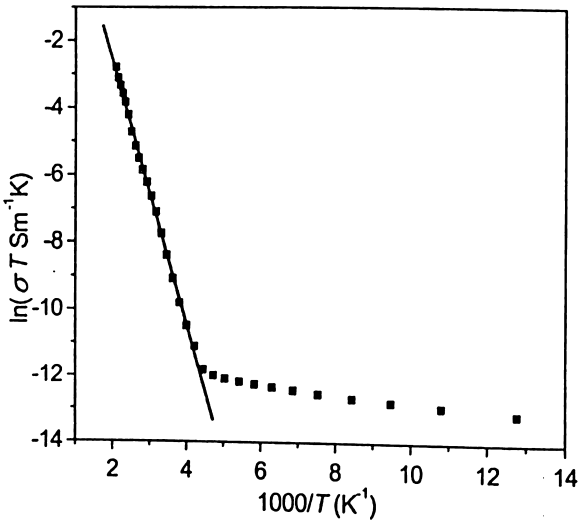

Figure 1.7: Conductivity data of a typical vanadate glass exhibiting a deviation from relation (1.10), there by showing the occurrence of a different conduction mechanism at low temperatures.

In low temperature range [as illustrated by the plot's deviation from linearity in figure 1.7 and hence from SPH behaviour], Mott's treatment of variable range hopping [70, 71] leads to a temperature dependent conductivity of the form,

$$\sigma = B e^{-A/T^{1/4}} \qquad (1.20)$$

where, A and B are parameters related to the localized wave function α, density of states at the Fermi energy $N(E_F)$, optical phonon frequency ν_o ($\sim 10^{13}$ sec^{-1}) and the Boltzmann constant k_B, and are given by the expressions,

$$A = 2.06\left[\frac{\alpha^3}{k_B N(E_F)}\right]^{\frac{1}{4}} \qquad (1.21)$$

$$B = \left[\frac{e^2}{2\sqrt{8\pi}}\right]\upsilon_o\left[\frac{N(E_F)}{\alpha\, k_B T}\right]^{\frac{1}{2}} \qquad (1.22)$$

The parameters α and $N(E_F)$ can be evaluated from the slope of a plot of $\ln(\sigma T^{1/2})$ vs $T^{-1/4}$ and from the intercept. The hopping distance R_{VRH} in VRH regime and hopping energy W_o can be obtained from α and R_{VRH} values using the relations [67],

$$R_{VRH} = \left[\frac{9}{(8\pi\alpha N(E_F)k_B T)}\right]^{\frac{1}{4}} \qquad (1.23)$$

$$W_o = \frac{3}{(4\pi R^3_{VRH} N(E_F))} \qquad (1.24)$$

At low temperatures, the polaron binding energy becomes lower than the disorder energy W_d and hence it is reasonable to assume that $W_o = W_d$ [72, 73]. Based on this assumption, Mott parameters $N(E_F)$ and R_{VRH} can be calculated. Further, for the occurrence of VRH conduction, the requirement $\alpha R_{VRH} > 1$ and $W_d \geq k_B T$ (eg., W_d 0.019 eV at 230 K) should be satisfied.

1.3.2. a.c. electrical properties

The temperature and frequency dependence of a.c. conductivity follows the universal empirical relation,

$$\sigma(\omega) = A\omega^s \qquad (1.25)$$

where A is a temperature dependent constant, ω is the angular frequency and the frequency exponent $s \leq 1$ [74, 75, 76]. A.C. conductivity increases linearly with increasing frequency for all glasses at different isotherms. At higher temperatures the increase become faster. This is generally attributed to the hopping of electrons controlled by the electric field in addition to the thermal excitation energy in the low temperature range and to band-band transitions or hopping over a barrier in the higher temperature

range.

Various models have been proposed to clarify the mechanism of a.c. conductivity in disordered materials. The quantum mechanical tunnelling (QMT) model was first proposed by Pollac and Gebelle [77] to interpret the impurity conduction in n type-silicon. In this model the a.c. conductivity is given by the expression,

$$\sigma_{ac}=Ce^2 k_B T\alpha^{-1}[N(E_F)]^2\omega R^4_\omega \qquad (1.26)$$

where C is a numerical constant, $N(E_F)$ is the density of state at Fermi level, α is the spatial decay parameter for localized wave function and R is the distance between the hopping sites. From equation (1.26) it is clear that the a.c. conductivity is linearly dependent on temperature.

Applying QMT to amorphous materials, Austin and Mott [78] proposed phonon assisted hopping of localized electrons. They extended their theory of polaron hopping in doped oxides which lead to variable range hopping in the d.c. regime and applied it to a.c. hopping. Using the proposition that all short-range hops contributed to the a.c. conductivity, the resulting formula was arrived at.

$$\sigma=\frac{\pi}{3}\frac{e^2}{k_B T}[N(E_F)]^2\alpha^{-5}\omega\left[\ln\left(\frac{1}{\tau_o\omega}\right)\right]^4 \qquad (1.27)$$

The correlated barrier-hopping (CBH) model [75] has been widely applied to glassy semiconductors. In this model, correlated barrier hopping of bipolarons (i.e. two electrons hopping between charged defects D^+ and D^-) has been proposed to interpret the frequency dependence of conductivity in glasses. The theory has been successful in

explaining many low temperature features. However, it does not explain the high temperature behavior so well particularly in the low frequency range. Shimakawa [79] suggested that D^o states are produced by thermal excitation of $D^+$and the single polaron hopping (i.e. one electron hopping between D^o and D^+ or D^-) contributes at high temperatures.

The overlapping large polaron-tunneling (OLPT) model [80] has also been proposed to understand the a.c. conductivity of glasses. According to this model the a.c. conductivity is given by,

$$\sigma_{ac}(\omega) = \frac{\pi^4}{12} e^2 (k_B T)[N(E_F)]^2 \frac{\omega R_\omega^4}{2\alpha k_B T + W_{HO} r_p / R_\omega^2} \qquad (1.28)$$

The correlated barrier-hopping model has been found to be most appropriate to explain the frequency and temperature dependencies of the a.c. conductivity and its frequency exponent. Other models explain some of the observed behaviours within a specific range of temperature or a certain value of polaron radius.

1.3.3. Thermoelectric power

The thermo electric power also known as Seebeck coefficient is mathematically defined as $Q = -\frac{\Delta V}{\Delta T}$, where ΔV is the thermo e.m.f developed due to the temperature difference ΔT across the surface of a material. For the case of band conduction in extended states, the variation of Seebeck coefficient with temperature is given by [1],

$$Q = \pm \frac{k_B}{e}\left(\frac{\Delta E_s}{k_B T} + A\right) \qquad (1.29)$$

where the positive and negative signs denote p-type and n-type conduction respectively, e is the electronic charge, k_B is the Boltzmann constant, T the absolute temperature, ΔE_s the activation energy for thermo electric power and A is a constant dependent on the mechanism of the electrical transport. A = 1, for the case of amorphous semiconductors exhibiting conduction in extended states.

Heikes proposed a model [81, 82] based on hopping mechanism to understand the Seebeck coefficient of semiconducting oxide glasses. In this model, the carrier is assumed to be trapped by its own distortional effect around a site. Carrier motion is possible by discrete jumps while a jump can only take place if the distortions around the initial and final sites are equivalent. A simple calculation in which the interactions are restricted to nearest neighbours leads to

$$Q = \frac{k_B}{e}\left[\frac{\Delta G_c}{2k_B T}\left(\frac{C}{A} - 1\right) + \ln\frac{c_o - c'}{c'}\right] \qquad (1.30)$$

where ΔG_c is the activation energy for the jump, c' is the concentration of freed carriers, c_o is the concentration of accessible sites, A is the energy required to remove the distortion around the initial site and C is the energy required to distort the final site and the ratio C/A is close to unity. In general, the first term in equation (1.30) is relatively small. The term "freed" originates from the fact that for very low carrier concentration and at low temperatures, the carriers are supposed to be trapped at sites neighbouring an impurity. For high concentrations and at higher temperature, it is no longer necessary to consider the freeing of carriers. In the case of semiconducting oxide glasses the carrier concentrations are generally very high, so that at any temperature in excess of room temperature, one can disregard the freeing of carriers. For these reasons, equation (1.30)

can be approximated to,

$$Q=\left(\frac{k_B}{e}\right)\ln\left[\frac{(c_o-c)}{c}\right] \qquad (1.31)$$

where c is now the concentration of carriers. It should be noted that the narrow band theory leads to a very similar expression for Q [82, 83].

For semiconducting oxide glasses, equation (1.31) has to be slightly modified. In a glass containing vanadium ions, only a small fraction of the V^{5+} ions is reduced to V^{4+}. It may be assumed that the additional electron located at the latter acts as a charge carrier and conduction takes place by the transfer of the electron from V^{4+} to V^{5+}. Then,

$$c = [V^{4+}] \ ; c_o = [V^{4+}+ V^{5+}] \text{ and } (c_o- c)/c = [V^{5+}]/[V^{4+}]$$

where the square brackets denote concentrations. Then the Seebeck coefficient for semiconducting oxide glasses in general becomes,

$$Q=\left(\frac{k_B}{e}\right)\ln\frac{[\text{high valence ions}]}{[\text{low valence ions}]} \qquad (1.32)$$

where e is the charge of the electron having the negative sign. If $[V^{5+}]/[V^{4+}] > 1$, then Q will be negative and if $[V^{5+}]/[V^{4+}] < 1$, Q will be positive.

1.3.4. Hall effect

When a magnetic field is applied perpendicular to a semiconductor carrying current, a voltage is developed across the specimen in the direction perpendicular to both the current and magnetic field. This phenomenon is known as Hall effect. If $H_{\perp}$ is the magnetic field applied perpendicular to the direction of flow of current density J_σ, then

the electric field F_H developed perpendicular to H_H and the current density J_σ in the electron-conducting solids are related to a parameter called Hall coefficient R_H [19, 29] given by,

$$R_H = \frac{F_H}{J_\sigma H_H} = \frac{1}{ne} \quad \text{or} \quad \frac{1}{pe} \tag{1.33}$$

where n and p are the electron and hole charge density. This enables one to determine the charge carrier sign in the case of unipolar conduction (or majority charge carrier type in the case of a semiconductor). The equation

$$\mu_H = |R_H|\sigma \tag{1.34}$$

gives the hall mobility μ_H of the semiconductor. The mobility in non-crystalline semiconductors is much smaller and the mean free path length is in the order of the interatomic distances. So the scattering mechanism cannot be predicted using conventional models. Chalcogenide glasses have a negative Hall coefficient, which at first seems surprising in view of the positive sign of the Seebeck coefficient. This contradictory result is viewed as a unique anomaly of vitreous semiconductors [84, 85]. However, in the case of $TlAsTe_2$ glass, the R_H showed the same sign as Q [85]. An explanation based on a configuration of three interacting centers has been proposed to interpret the observed differences in the sign of R_H and Q [86].

1.3.5. Majority charge carrier reversal (MCCR) phenomenon

In a crystalline semiconductor, one can change the sign of the majority charge carriers by controlled addition of impurities (dopants). It is thus natural to make an attempt to

change the sign of charge carrier in amorphous semiconductors and explore its potential in applications. Chalcogenide glasses are p-type semiconductors with the Fermi energy level pinned near the valence band. Shattering the myth that the Fermi energy level in these glasses could not be unpinned, Toghe et al [87] demonstrated that n-type glasses could be obtained in chalcogenide glasses. This majority charge carrier reversal in bulk Ge-M (M = S, Se, Te) glasses could be achieved with the addition of appropriate amounts of either Bi or Pb [87, 88]. Two models proposed to understand the sign reversal in Bi modified Ge-Se glasses are significant. The first model attributed the sign reversal to the destabilization of the balance between the charged defect centers present in the glass on the addition of additives (Bi or Pb), which are present in different charged configuration [89]. The second model treats the carrier reversal as due to the percolation of rigid clusters (which are strong n-type conductors) [90].

Vanadium pentoxide based glasses are generally n-type semiconductors [6]. As already mentioned, vanadium ions exist in V^{5+} and V^{4+} states in these glasses. In n-type glasses, the ratio of the higher valence ion to the lower valence ion, namely, $\frac{V^{5+}}{V^{4+}} > 1$. If V^{5+} and V^{4+} ion concentration could be controlled such that $\frac{V^{5+}}{V^{4+}} < 1$, then one can obtain p-type glasses in this system. This observation was empirically proposed by Allersma and Mackenzie [91], many years ago. However, not much attention has been given to this phenomenon in oxide glasses as shown by a general lack of reports in the literature on such glasses.

1.4. Optical properties of glasses

Amorphous solids are optically isotropic. However, macroscopic inhomogeneties result in small variations in the refractive index of these solids. In amorphous materials the k-vector conservation in photon-phonon interactions is no longer valid (since these materials do not have a well defined reciprocal space). So all phonons can take part in first order interactions with light. Hence, the entire phonon density of states appear in the infrared and Raman spectra which result in a broad band instead of the discrete line spectrum observed in crystals. Amorphous materials have a forbidden gap and hence an absorption edge. In chalcogenide glasses, the density of states is determined by the topological disorder, ring statistics of the network and nature of the molecular units [92].

In oxide glasses, UV absorption edges shift to higher energies where the electrons participate in stronger chemical bonds [18]. Thus, in B_2O_3, SiO_2, and P_2O_5 glasses, the UV edge moves from 170 to 160 to 145 nm. Presence of nonbridging oxygens reduces the average chemical bond strength, and hence the UV edge shifts to longer wavelengths. Consequently, optical band gap decreases. Yu et al [93] studied the optical absorption of V_2O_5-P_2O_5 glasses. They found that there is a fundamental absorption edge in the range 2.34 eV to 2.8 eV, which arises from a direct forbidden electron transition. Moustafa et al [94] found that the optical band gap of barium vanadate glasses doped with Fe_2O_3 varied from 2.27 eV to 1.99 eV. The change in the optical band gap was attributed to the distortion of the field around the vanadium ions accompanying matrix modification with the addition of Fe_2O_3.

Optical absorption

The absorption edge in amorphous semiconductors can be generally separated into three regions [95] with absorption coefficients $\beta \geq 10^4$ cm^{-1} , $1 \leq \beta \leq 10^4$ cm^{-1} and $\beta \leq 1$ cm^{-1} and are referred to as the high absorption (A) region, the exponential (B) region and the tail (C) region of the absorption curve {figure 1.8}. The first two regions arise due to transitions within a fully coordinated system perturbed by defects, while the third region arises due to transitions involving defect states directly.

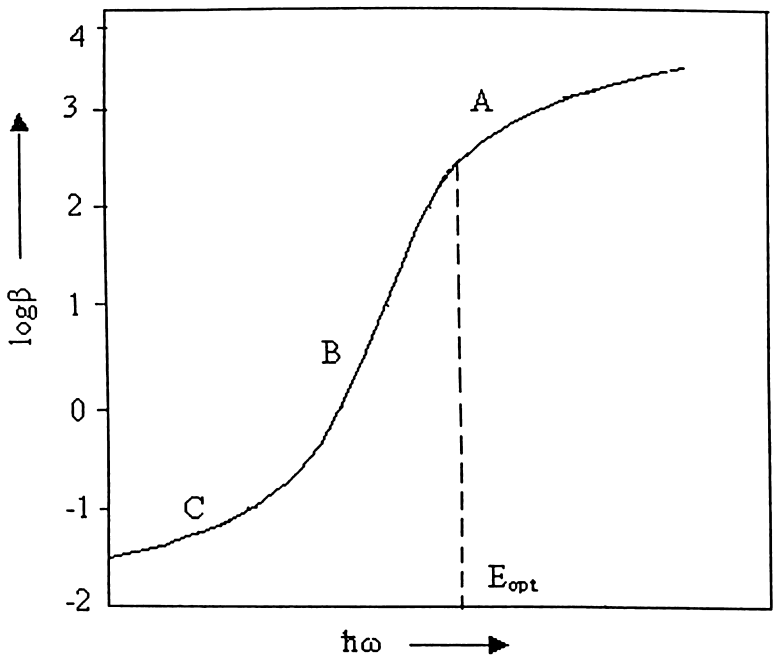

Figure 1.8: Regions A, B, C of a typical absorption curve

In the high absorption region, the absorption coefficient has the following frequency dependence:

$$h\nu\beta(\nu) = B(h\nu - E_0)^r \qquad (1.35)$$

where ν is the frequency, B is a constant , E_0 is the optical band gap and r is a constant. r = 2, if the band edges are both parabolic. Exception to this quadratic frequency dependence is observed in a-Se and some multicomponent glasses. From the above

expression an empirical definition for the optical band gap can be made. In amorphous materials, all pairs of extended states with energy difference hν can contribute to optical absorption. A plot of $[h\nu\beta(\nu)]^{1/2}$ vs. hν for which $\beta^{1/2} \rightarrow 0$, gives the optical band gap E_{opt}.

In the intermediate absorption region, β(ν) assumes the form,

$$\beta(h\nu) = C e^{h\nu/E_e} \qquad (1.36)$$

where E_e is the energy characterizing the slope and C is a constant. E_e is independent of temperature at low temperatures and has the value 0.05 eV to 0.08 eV for most chalcogenide glasses. The origin of this exponential tail is not clear. Disorder induced potential fluctuations [96, 97] and strong electron-phonon interactions [98] have been suggested as possible reasons for the exponential absorption. In the weak absorption tail region, the strength and the shape of the absorption tail are found to depend on the preparation, purity and the thermal history of the material [99].

1.5. Other physical properties of glasses

1.5.1. Density and Molar volume

Density a substance is defined as the mass per unit volume. Density is a bond sensitive property [2, 100]. The dependence of density upon temperature is through the volume thermal expansion coefficient. Since glasses may, in general, be regarded as solutions, a more useful property is the molar volume V, defined as the volume of one-gram mole of glass. Then one can proceed to define partial molar volumes of the structural units constituting the glass. The partial molar volume v_i of a species i in a solution is defined [18] by,

$$v_i = \left(\frac{\partial V}{\partial n_i}\right)_{n_j, T, P} \qquad (1.37)$$

where $V = n_i v_i + n_j v_j$, and n_i, n_j are the molar fractions of the species i and j. In essence, the total molar volume is treated as an extensive property in terms of the partial molar volumes of individual species or structural groups. The partial molar volume information can be extracted from the density data of glasses where the constituents have been systematically varied. The molar volume V_m can be determined from the relation,

$$\text{Molar volume} = M/\rho \qquad (1.38)$$

where M is the mass of one mole of glass and ρ is the density. On the other hand, V_m can be expressed [101] by an additive relation of the form,

$$V_m = \Sigma n_i V_i \qquad (1.39)$$

where n_i is the number per mole of the structural unit and V_i is its volume.

The dependence of density upon cooling rate, temperature and composition [102] can be studied from the volume variation of a supercooled liquid as it transforms into glass. Except for a few anomalous cases, such as silica, a fast-cooled glass generally has a higher volume, and hence a lower density, relative to a slow-cooled glass of the same composition. The thermal expansion coefficient of most glasses increases sharply in the glass transition region and beyond. Thus, the effects of temperature variation on the density of a glass are usually small in the glassy state [103].

The molar volume of oxygen ion V_o^* can also be considered as a physical parameter related to density. It is calculated from an empirical relation. For example,

molar volume of oxygen ion for the V_2O_5–SnO-TeO_2 glass system is calculated from the relation,

$$V_o^{\bullet} = \frac{[\{M(V_2O_5) - 16C_v\}x + M(TeO_2)y + M(SnO)z]}{[\rho(5 - C_v)x + 2y + z]} \qquad (1.40)$$

where ρ is the density of the glass composition, $C_v = \frac{V^{4+}}{V_{total}}$ (where $V_{total} = V^{4+} + V^{5+}$), x,y,z and $M(V_2O_5)$, $M(TeO_2)$, M(SnO) are the molar fraction and molecular weight of V_2O_5, TeO_2, SnO respectively.

1.5.2. Microhardness

Interest in the microhardness of materials is at least twofold. There is a general interest in material properties as such and secondly, there is a desire to obtain an understanding of the microhardness based on the models, which involve structural parameters on an atomic scale [104]. Vicker's indentation measurements of microharness will be discussed in chapter 2 of this thesis in detail. Vicker's Hardness number (VHN) [104] is given by

$$VHN = \frac{2F\sin\frac{\theta}{2}}{d^2} \qquad (1.41)$$

where F is the load applied, θ is angle of the Vicker's pyramidal indenter (which is 136°) and d is the length of diagonal in micrometers.

Although the physics of hardness is still not understood completely, one can discuss hardness in relation to elastic moduli and bond strength parameters according to the model of Yamane and Mackenzie [104] using elastic moduli to constrain the effective bond strength. Hardness of any material is the result of a complex process of deformation during indentation, the nature of which is even more cryptic in the case of glasses because of our limited knowledge of the glass structure. During the process of indentation

the material undergoes both compression and shear resulting in the observed deformation, which comprises of elastic deformation, flow and densification [105, 106]. The bond strength of a certain compound determines the ratio of recoverable and irreversible deformation. A high bond strength causes high elastic moduli preventing breakage, while a small bond strength results in a higher percentage of bond breaking concomitant irreversible, plastic flow. This concept led Yamane and Mackenzie [104] to estimate Vicker's hardness, VHN from the square root of the bond strength, the bulk modulus B and the shear modulus G,

$$VHN = C\sqrt{\alpha BG} \qquad (1.42)$$

where C is a proportional constant and α is the bond strength factor. From equation (1.42) it is evident that the VHN decreases as the elastic moduli of the glass decreases. This behaviour has been observed in many glasses [35, 105].

If the experimental data on elastic moduli B and G are available, the above relation may be used to calculate a semi-theoretical VHN and to compare this with the measured hardness VHN. It has been found that the microhardness is related to the dilatometric softening point T_d, which is usually obtained from thermal expansion curves. T_d is defined [35] as the temperature at which the glass sample reaches a maximum length in a length versus temperature curve when heated. It has been found that microhardness systematically decreases with a decrease in the softening temperature [107].

1.6. Some features of the present work

A brief statement of the motivation behind the thesis work and a general perspective of the approach used are given here. Vanadium tellurite glasses generally exhibit n-type

semiconductor behavior [13]. The interesting electronic conduction mechanisms exhibited by these glasses have already been highlighted in this chapter. The strong dependence of the electrical properties on the ratio of V^{4+} and V^{5+} ions in these glasses has led to application as oxygen gas sensors [108]. However, a perusal of some of the leading texts on glasses [1, 2, 18, 29, 35, 109, 110] would show the general lack of information on these glasses. The majority charge carrier reversal (MCCR) phenomenon observed in semiconducting glasses is most certainly worthy of investigation, as this phenomenon holds a lot of promise in device applications. The breakdown of the myth that chalcogenide glasses cannot be doped has generated a lot of activity on the MCCR phenomenon in Pb and Bi modified chalcogenide glasses. However, neither the MCCR phenomenon in oxide glasses nor the physical properties of oxide glasses exhibiting this novel phenomenon have been given much attention in the literature. The available information on V_2O_5 glasses exhibiting MCCR is summarised below.

Recently Mori et al reported the possibility of obtaining p-type semiconductor in $xV_2O_5.20SnO.(80\text{-}x)TeO_2$ glass system, where $20 \leq x \leq 50$ [70]. A single composition of glass, namely, $20V_2O_520SnO60TeO_2$ was reported to be a p-type semiconductor while the rest were n-type. This research group has also studied the d.c. electrical properties of these glasses [72, 111]. Kennedy and Mackenzie reported the feasibility of obtaining p-type compositions in V_2O_5-CaO-P_2O_5 and V_2O_5-CaO-B_2O_3 glasses [7, 91] more than four decades ago. In their pioneering work, they showed that the Seebeck coefficient (Q) of these glasses are related to the ratio of vanadium ions $\frac{V^{5+}}{V^{4+}}$ as predicted by the empirical relation (1.32). Subsequent to this early work, no further studies have been reported on these two glass systems.

It is evident from the literature survey that the glass systems V_2O_5-SnO-TeO_2, V_2O_5-CaO-P_2O_5 and V_2O_5-CaO-B_2O_3 provide the opportunity to explore the majority charge carrier reversal (MCCR) phenomenon in oxide glasses. There is a general lack of systematic experimental studies in these three glass systems as indicated by the literature survey. Hence these three glass systems were taken up for study in this thesis work. The primary aim was to prepare good quality glasses in these systems and to establish the occurrence of MCCR in these glass systems. This would involve the measurement of Seebeck coefficient and estimation of the ratio of vanadium ions $\frac{V^{5+}}{V^{4+}}$ in various glass compositions. Understanding the d.c. electrical conduction mechanism(s) in these glasses as a function of temperature (100 K to 400 K) would provide the next set of interesting information on these glasses.

Although a wide variety of physical properties of these glasses could be studied, the present thesis work is limited to the following. Differential scanning calorimeter (DSC) studies on the glasses provide information on the glass structure and stability. Visible spectrophotometry allows one to estimate the optical bandgap of the glasses, which is a characteristic property of amorphous semiconductors. Density and microhardness are two other properties that provides information on the network structure.

The heat capacity jump at T_g could be correlated to the fragility of the glass. Electrical properties are in general, structure sensitive. From these studies, it would be interesting to look for any features occurring at the composition at which the conduction type change is observed. Although a straight forward correlation between an electronic phenomenon such as MCCR and a physical property of non-electronic origin is not

possible, the reported work on Bi and Pb modified Ge-Se glasses show that a variety of physical properties such as ΔC_P [112, 113], thermal diffusivity [114], density [115, 116], optical bandgap [114] etc., exhibited anomalous behaviour at the MCCR composition. The reported work on chalcogenide glasses clearly shows that even physical properties of non-electronic origin are often sensitive to the MCCR phenomenon in these glasses. This has lent support to arguments that structural changes accompany the electronic transition in these glasses. Attempts have been made in this thesis to find out if the properties of V_2O_5 based glasses exhibiting MCCR show any anomalous feature close to the composition at which MCCR occurs.

Chapter 2

Experimental Techniques

In this chapter, the experimental techniques used in the current investigations are discussed together with the relevant theory associated with these techniques. Specific instruments used and the measurement methodology employed are also discussed. The experimental results presented in chapters 3, 4 and 5 are based on the experimental procedures outlined in this chapter.

2.1. X-ray diffraction

A commercial X-ray powder diffraction system (Seifert XRD 3003 T/T) was used for the verification of the amorphous nature of the as-quenched glass samples. Cu K_α radiation (1.541 Å) with a Nickel filter was used. The X-ray generator was operated with an acceleration voltage of 40 kV and tube current of 30 mA. The theta-theta goniometer was used in the reflection (Bragg-Brentano) geometry {figure 2.1}. A thick layer of powdered sample spread over a perspex plate coated with a thin layer of high vacuum grease was used for recording the X-ray diffraction (XRD) patterns. The XRD data provides the variation of intensity/counts per second (cps), recorded by the detector (scintillation counter) as a function of 2θ, where θ is the glancing angle. A typical XRD pattern of a glass sample is shown in figure 2.2. The absence of sharp crystalline (Bragg) peaks in the XRD pattern with broad humps is the typical signature of an amorphous material. This experimental technique was used to confirm the amorphous nature of all the samples prepared for the present investigations.

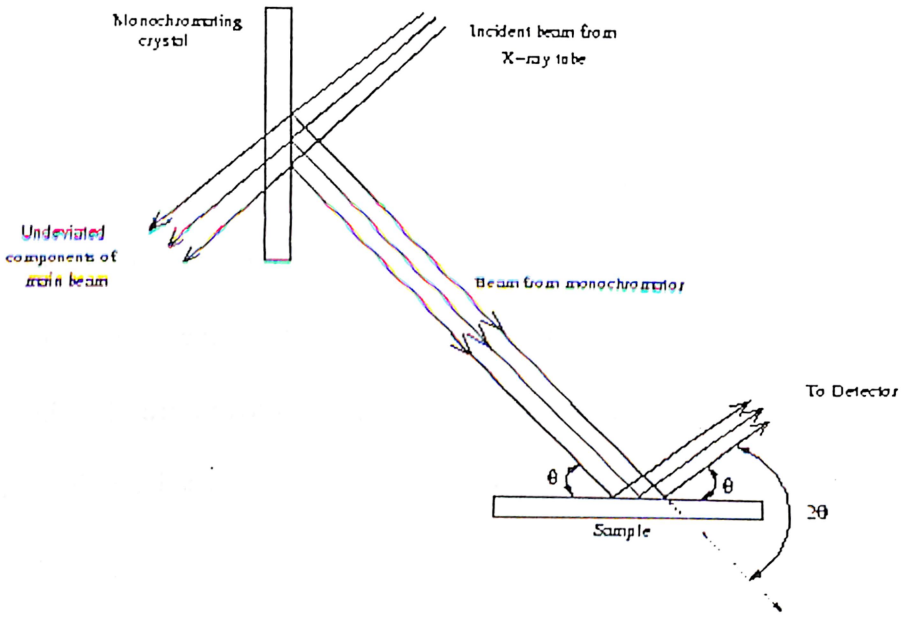

Figure 2.1: Ray diagram for X-ray diffractometer.

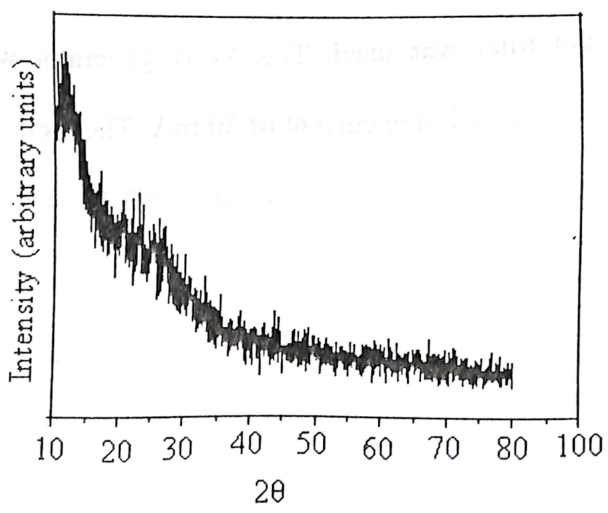

Figure 2.2: A typical XRD pattern of a glass sample.

2.2. Differential Scanning Calorimeter

Differential scanning calorimeter (DSC) is a thermal analysis technique, with which the thermal behavior of a sample can be studied over a wide temperature range, under

isothermal as well as non-isothermal conditions. This thermal technique was commercially developed by Watson et al [117]. In this technique, the sample and reference are maintained at the same temperature with respect to each other by proper application of electrical energy. The heat flow, dH/dt to the sample and a reference at the same temperature is recorded as a function of temperature. The reference is an inert material such as alumina or just an empty aluminum sample pan. In non-isothermal measurements, the temperature of the sample and reference are increased at a constant heating rate. Thermal changes in a sample may be of exothermic or endothermic nature. Some of the endothermic transitions are the glass transition, reduction, dehydration and some decomposition reactions. Crystal-crystal structure transformation, glass-crystal transition, oxidation and some decomposition reactions are the most frequently studied exothermic transitions.

A commercial instrument (Perkin-Elmer, DSC 7) was used in the present investigations. This is a power compensation differential calorimeter in which the heat to be measured is almost totally compensated with electric energy, by increasing or decreasing an adjustable Joule heat. The measuring system consists of two thermally insulated microfurnaces made of a platinum-iridium alloy. A temperature sensor (platinum resistance thermometer) and a heater (made of platinum wire) are embedded in each of these microfurnances {figure 2.3}. The measuring range could be extended from −175 °C (liquid nitrogen cooling) to 725 °C. In the present studies, the instrument was calibrated for optimal operation from room temperature to 500 °C. High purity zinc (m.p. = 418.6 °C) and indium (m.p. = 156 °C) were used to calibrate the instrument's temperature scale. Measurements were done with weighed quantities (~ 20 mg) of glass

samples taken in crimped aluminium sample pans. High purity nitrogen gas was continuously purged during the entire duration of the experiment. DSC curves were recorded at constant heating rates of 10, 15, 20 and 30 °C min^{-1} .

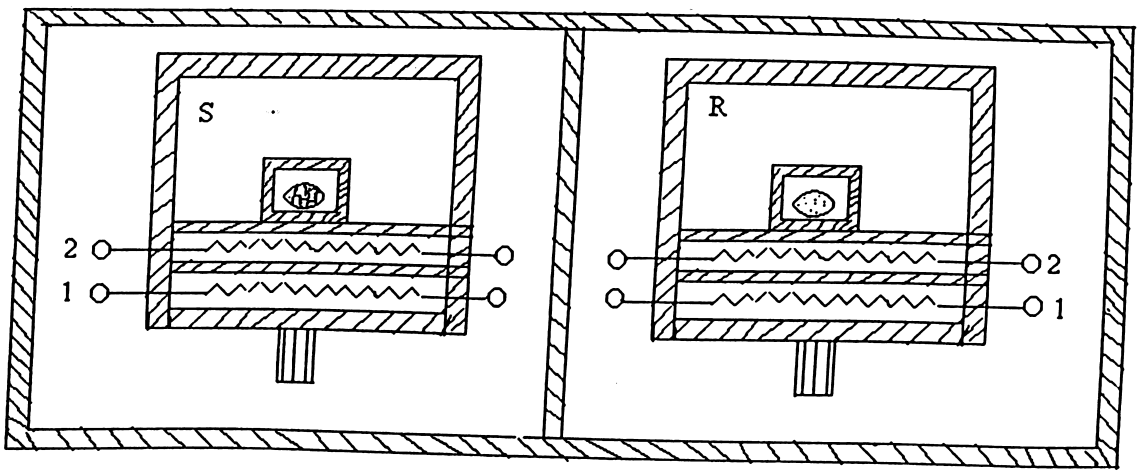

Figure 2.3: Power compensation DSC. S is the sample measuring system with sample crucible, R is the reference sample system, 1 is the heater and 2 is the platinum resistance thermometer.

A typical DSC trace of a glass is shown in figure 2.4. As a glass is heated at a constant heating rate in a DSC, the heat flow exhibits an endothermic base line shift at the glass transition temperature (T_g), followed by an exothermic crystallization peak at T_c. Further heating results in melting of the sample at T_m, which is an endothermic transformation. Generally, it has been observed that glasses, which are unstable, show one or more exothermic peaks corresponding to devitrification of various phases. Such glasses may sometimes show multiple melting endotherms as well. The T_g values reported in the present studies correspond to the on-set of the glass transition {figure 2.4}. The crystallisation temperature reported correspond to the value at the maximum of the exothermic peak.

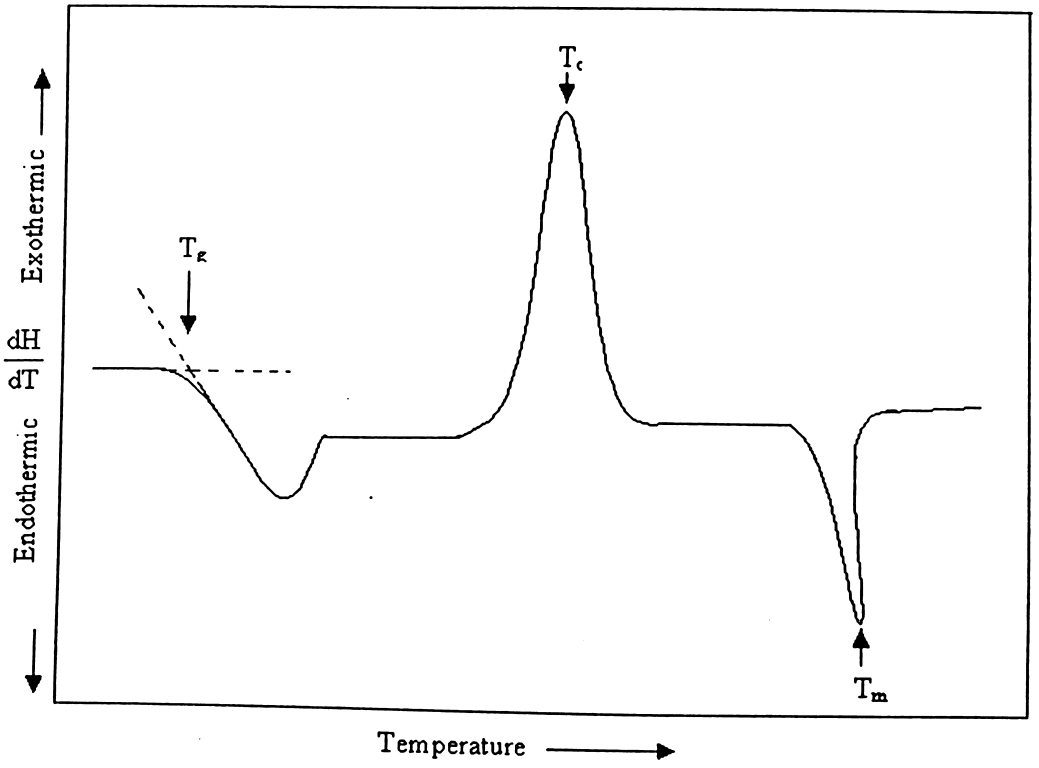

Figure 2.4: A typical DSC curve of a glass

A kinetically controlled reaction temperature (such as T_g or T_c) shifts with heating rate. Once the data on T_g and T_c at different heating rates are available, the activation energy of the reaction (which is a measure of the inhibition to the process) could be estimated using the Kissinger's method or Augis–Bennett method or Thakor's method [118, 119]. These methods provide Arrhenius relations from which the activation energy could be determined. The Kissinger, Augis-Bennett and Thakor relations are given in equations (2.1), (2.2) and (2.3) respectively.

$$\frac{d\left[\ln\left(\frac{\varphi}{T_g^{\,2}}\right)\right]}{d\left[\frac{1}{T_g}\right]} = -\frac{E_K}{R} \qquad (2.1)$$

$$\frac{d\left[\ln\left(\frac{\varphi}{T_g}\right)\right]}{d\left[\frac{1}{T_g}\right]} = -\frac{E_{A-B}}{R} \qquad (2.2)$$

$$\frac{d\left[\ln\left(\varphi\right)\right]}{d\left[\frac{1}{T_g}\right]} = -\frac{E_T}{R} \qquad (2.3)$$

where φ is the heating rate, E_K, E_{A-B}, and E_T are the activation energy obtained from the Kissinger, Augis-Bennett and Thakor equations, respectively, and R is the universal gas constant. Further, $E_T > E_{A-B} > E_K$ [120, 121]. Kissinger's and Thakor's methods are commonly used as shown by several reports in the literature. In the present investigation both Kissinger's and Thakor's methods are used to elucidate the activation energy of glass transition. A form of equation (2.3), which is referred to as Bartenev's equation [29] is obtained by replacing E_T by E_η, the activation energy for viscous flow in the glass transition. The degree of fragility m, is related to E_η by the relation [122],

$$m = \frac{E_\eta}{2.3RT_g} \qquad (2.4)$$

where R is the universal gas constant. The relation between the excess heat capacity ΔC_P at the glass transition and fragility has already been discussed in chapter 1.

2.3. Thermoelectric power measurement

The thermoelectric power (TEP) or Seebeck coefficient (Q) of glasses has been discussed in chapter1. Thermoelectric power measurements were performed on the as-quenched

samples using an indigenously developed set-up. A temperature gradient across a thin slice of glass sample was maintained by passing an electric current through a resistive heater embedded inside a copper block on which the sample was placed {figure 2.5}.

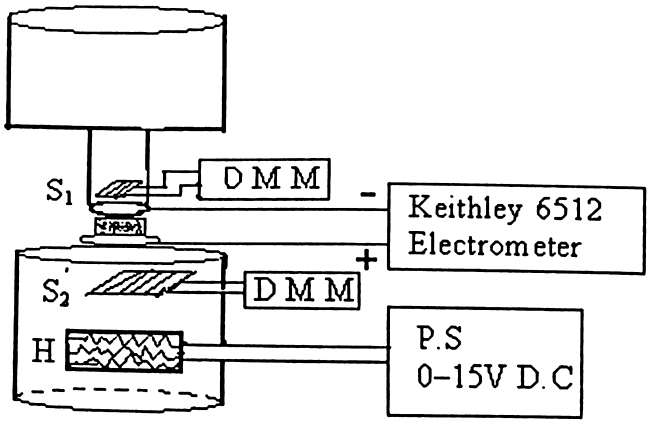

Figure 2.5: Experimental setup for thermoelectric power (TEP) measurements

A spring loaded copper rod, which served as an electrode was placed over the sample. The potential difference developed due to thermal conduction through a thin slice of the sample was recorded using an electrometer (Keithley 6512). The temperature gradient between the lower and upper sample surfaces was monitored using two calibrated thin film PT100 sensors placed on the two sides of the sample. The resistance values of the calibrated sensors were recorded using two digital multimeters (Hewlett Packard 34401A). With this arrangement, the thermoelectric power of the samples could be measured from room temperature to 450K with an experimental error of ±2%. As a convention, the lower surface of the sample (hot probe) is connected to +ve terminal of the electrometer and the upper surface (cold probe) is connected to the common terminal of the electrometer. When a temperature difference, ΔT is established between the upper and lower surfaces, charge carrier moves from the hot probe to cold probe, thus creating a

thermo e.m.f., ΔV across the sample. The Seebeck coefficient is then given by, $Q = -\frac{\Delta V}{\Delta T}$. If the potential difference monitored by the electrometer (using the convention specified above) is negative, then Q is positive and the sample is a p-type semiconductor. On the other hand, if the potential difference is positive then Q is negative and so the sample is an n-type semiconductor. The majority charge carrier type in each glass sample was identified using the TEP measurement.

2.4. Estimation of Vanadium ion concentration

The concentration of vanadium ions (V^{4+} and V^{5+}) present in the glasses can be estimated iodometrically [123] using the following procedure. An accurately measured 0.1 gm of the powdered sample was dissolved in 50ml of distilled water. To the solution, 5ml of 4M H_2SO_4 was added, followed by the addition of ~2 gm of KI under constant stirring. This mixture was then kept in a dark room for 15 minutes. The liberated iodine was then titrated with standard $Na_2S_2O_3$ solution using starch as an indicator. The end point was detected by the appearance of a light blue colour. The volume of the $Na_2S_2O_3$ consumed was noted down and the percentage of V^{5+} in the glass sample was estimated using the relation,

$$V^{5+}\% = \frac{51 * (\text{Strength of } Na_2S_2O_4) * (\text{Volume of } Na_2S_2O_4 \text{ consumed})}{\text{weight of the compound taken}} \times 100 \qquad (2.5)$$

where 51 is the atomic weight of vanadium.

In the next step, V^{tot} % (=V^{4+}+V^{5+}) in the sample was estimated. For this, 0.1 gm of the powdered sample was dissolved in a solution containing 50ml of distilled water

and 5ml of 4M H_2SO_4. An oxidising agent [ammonium peroxo disulphate ($N_2H_8S_2O_8$)] was added to this solution followed by one/two drops of silver nitrate ($AgNO_3$) solution. This oxidises all the V^{4+} ions contained in the compound into V^{5+}. The resultant mixture was boiled for one hour. After this, 10ml of 4M H_2SO_4 was added and the solution was boiled again for 30 minutes. The solution was then allowed to cool down to room temperature and 2gm of KI was added under constant stirring. As before, the solution was kept in a dark room for 15 minutes. The liberated iodine was then titrated with the standard $Na_2S_2O_3$ solution as in the previous titration. From the volume of $Na_2S_2O_3$ solution consumed, the V^{tot} % was estimated from the relation (2.5). Then V^{4+} % can be obtained since V^{4+} % = (V^{tot} % - V^{5+} %.). From V^{4+} % and V^{5+} %, the ratio of the vanadium ions, $\frac{V^{5+}}{V^{4+}}$ in each sample was determined.

2.5. Density Measurement

Density is measured by weighing a suitably selected piece of glass in air and delivering this weight by the buoyancy, when the sample is suspended in water. According to Archimedes principle, the buoyancy equals the weight of the displaced fluid, which, for water, equals the volume. If W_a is the weight of the specimen in air and W_b in water, then the buoyancy is (W_a-W_b) and density (assuming density of water is 1 gm/c.c),

$$\rho = \frac{W_a}{W_a - W_b} \qquad (2.6)$$

Glass samples may react with water, in which case, a suitable inert liquid such as xylene is selected as the immersion fluid (CCl_4 has also been widely used [124], but CCl_4 is a

carcinogen). If W_1 is the weight of the density bottle filled with xylene and W_2 is the weight of the density bottle with xylene and sample outside the density bottle, then the weight of the sample is (W_2-W_1). If W_3 is the weight of the density bottle with the sample immersed in xylene, then the sample weight loss in the immersion medium is (W_2-W_3). Then the specimen volume is,

$$V = \frac{W_2 - W_3}{\rho_m} \tag{2.7}$$

where ρ_m is the density of xylene and the density of the specimen [125] is,

$$\rho = \frac{W_2 - W_1}{W_2 - W_3} \times \rho_m \tag{2.8}$$

The Molar volume [115, 126] of the samples can be calculated from the following expression,

$$\text{Molar volume} = \frac{M}{\rho} \tag{2.9}$$

where ρ is the density of the glasses and M is the molecular weight. For a typical multicomponent oxide glass, say V_2O_5-SnO-TeO_2, M is given by the relation,

$$M = xM(V_2O_5) + yM(SnO) + (1-x-y)M(TeO_2) \tag{2.10}$$

where x, y, and (1-x-y) are the mole fractions of the constituents and $M(V_2O_5)$, M(SnO) and $M(TeO_2)$ are the molecular weights of the constituents. In the present measurements, high purity (analar grade) xylene was used as the immersion fluid and each density value reported is the average of at least three independently measured values.

2.6. Optical band gap measurement

A ultraviotet-visible-near infra-red spectrophotometer permits one to measure [29] the absorbance of a thin slice of glass as a function of wavelength (λ). The optical band gap of semiconducting glasses can be estimated from the optical absorption curves [127]. Depending on the absorption coefficient β(ν), the absorption curve of an amorphous semiconductor can be divided into three regions {figure 1.8}. The optical band gap corresponds to the high absorption region. In high absorption region, the absorption coefficient has the following frequency dependence,

$$\beta(\upsilon) = \frac{B}{h\upsilon}\left(h\upsilon - E_{opt}\right)^{r} \qquad (2.11)$$

where E_{opt} is the optical band gap, B is a constant, hν is the photon energy of the incident radiation and r is an index which can assume values 0.5, 1, 1.5, 2 or 3 depending on the nature of the inter-band electronic transition. The above equation agrees well for chalcogenide and oxide glasses with r=2 (indirect transition) [128, 129]. The optical band gap for indirect transition can be obtained by plotting $(\beta h\nu)^{1/2}$ versus hν. The E_{opt} is the x-intercept of the extrapolated linear fit to high hν data. A typical plot for $(\beta h\nu)^{1/2}$ versus hν for a glass sample is shown in figure 2.6. The procedure for obtaining the optical band gap for indirect transition from such a plot is also illustrated in the figure. The optical band gap obtained by this procedure has an inherent uncertainty since it is not evident whether the band gap corresponds to extended-extended transitions or localized–extended transition. Both the transitions are possible theoretically [1].

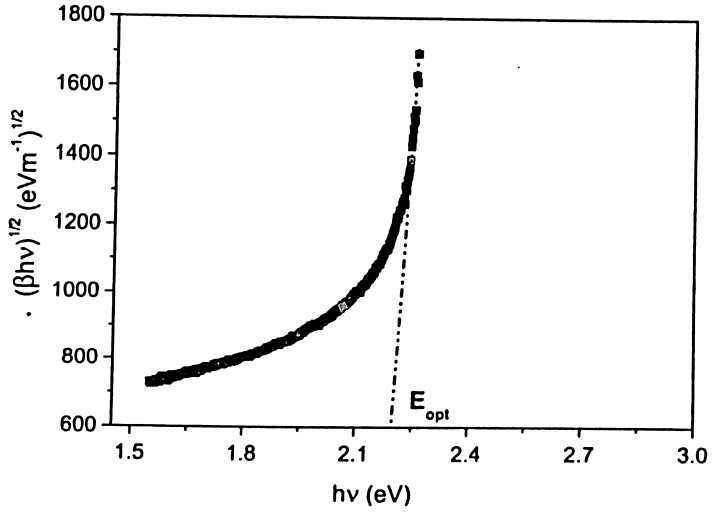

Figure 2.6: Relation between $(\beta h\nu)^{1/2}$ and hν of a typical glass sample.

A commercial dual beam uv-vis-nir spectrophotometer (Shimadzu UV-3101PC) was used for recording the absorption curves of glass samples. This optical system {figure 2.7} consists of a double grating monochromator M, light sources LS (deuterium lamp and halogen lamp) and a detector assembly D (Photomultiplier tube and PbS detector). Wavelength can be continuously varied between 190 nm and 3200 nm for absorption measurements. In the present investigation, a wavelength range of 190 nm – 800 nm was sufficient for the coarse measurement of band gap of the samples studied.

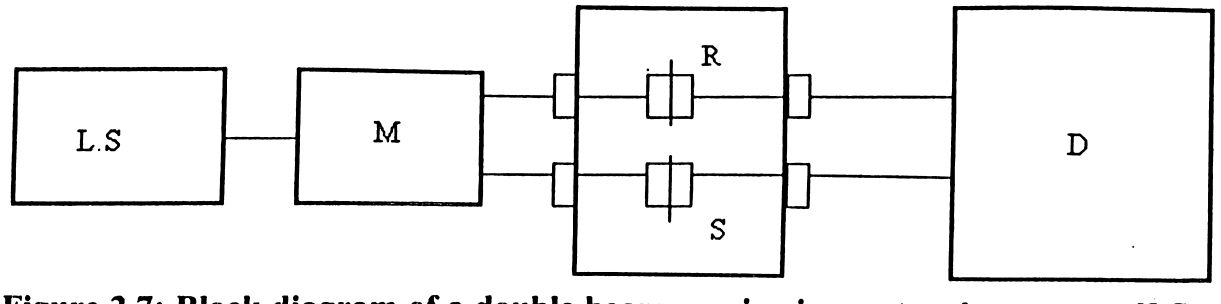

Figure 2.7: Block diagram of a double beam uv-vis-nir spectrophotometer. [LS= Light sources (Deuterium and halogen lamp), M=double grating monochromator, R=Reference, S =Sample, D=Detector (Photomultiplier and PbS detector)

2.7. Microhardness measurement

The microhardness (or simply the hardness measured over a micron distance scale) is a characteristic property of solids. The hardness is a measure of the resistance of a material to being penetrated and eroded by another material's sharp projections. The measurement method involves the use of a diamond micro indenter either in the shape of a square pyramid (Vicker's) or an elongated pyramid (knoop). Figure 2.8 explains the process of a small diamond indenter being pushed into the material under a known load.

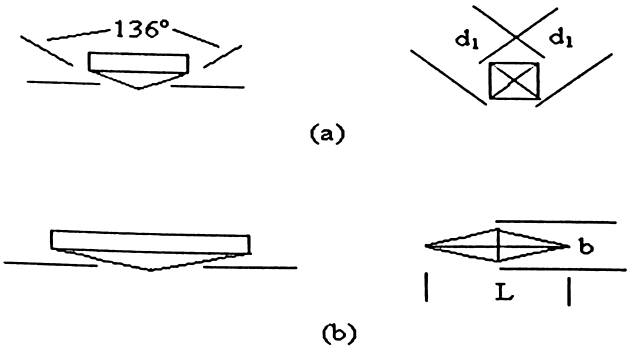

Figure 2.8: Geometry of microhardness indenters (a) Vicker's (b) Knoop.

The size of the indentation is generally of the order of a few microns under 5 to 1,000 g loads and hence the term "microhardness". For the Vicker's indenter,

$$VHN = \frac{force}{area} = \frac{2F\sin\left(\frac{\theta}{2}\right)}{d^2} \qquad (2.12)$$

where F is the force in Kg, θ is the inclined angle of Vicker's pyramid and d is the average diagonal of the impression in mm. Since $\theta = 136^0$ for the Vicker's pyramid, VHN (expressed usually in units of kg/mm^2) may be written as

$$VHN = \frac{1.8544F}{d^2} \qquad (2.13)$$

Generally, a total indentation time of 15-25 seconds is used for the measurement, which is sufficient for the load to gradually descend onto the surface and reach an equilibrium penetration depth.

When an indentation is made in a glass, initially the glass is elastically compressed (by the hydrostatic component) and sheared (by the shear component). Next, after reaching the elastic limit, the balance of the hydrostatic stress component permanently densifies the glass under the indentation, whereas the balance of the shear stress component causes the glass to undergo plastic deformation [130, 131]. When the indenter is withdrawn, the elastic portion recovers, i.e., a slight shrinkage of the impression size is expected. Clearly, the hardness number cannot be independent of the applied load. Also, when large loads are used, cracking from the diagonals is likely to develop. The cracking implies the occurrence of a fracture.

Careful preparation of the sample surface is necessary prior to indentation. For this, the samples are mounted on a resin and polished to a mirror finish. The polished samples are then indented using a Vicker's diamond pyramidal indenter and the length of the diagonals of the indents are measured using a microscope. A typical indent made on a polished glass sample is shown in figure 2.9. The indent corresponds to an applied load of 100gm and loading time of 15 seconds. The microhardness values reported in this thesis are the average values of at least 10 independent indents made on each sample composition under identical loading conditions. In the present study, a Buehler Simplet 2 mounting press, a Buehler Ecomet 6 variable speed grinder/polisher and a Buehler

Micromet 2100 automated microhardness tester were used. All measurements were made at room temperature.

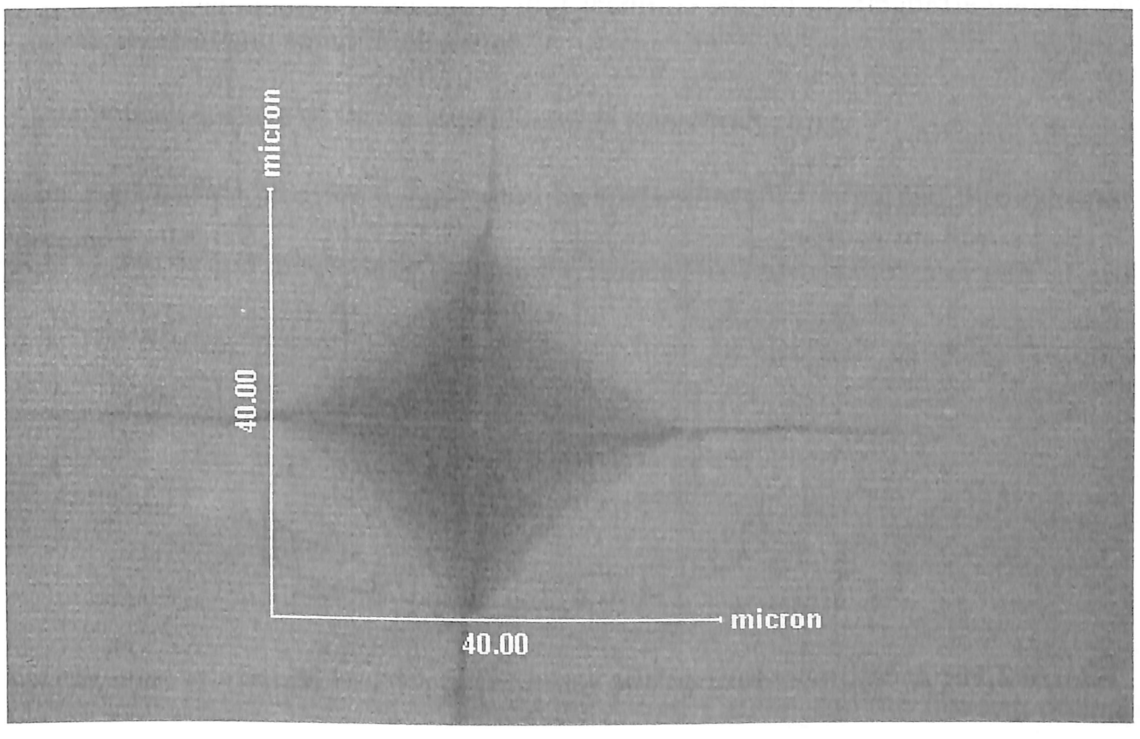

Figure 2.9: A typical indent made on a polished glass surface using a Vicker's pyramidal indenter.

2.8. d.c. electrical conductivity measurement

Many conventional methods for measuring electrical resistivity are unsatisfactory for semiconductors because metal-semiconductor contacts are usually rectifying (non ohmic) in nature [132]. There is also the possibility of minority carrier injection by one of the current carrying contacts. An excess concentration of minority carriers will affect the potential of other contacts and modulate the resistance of the material [19]. The collinear four-probe method used as experimental technique for measuring resistivity overcomes the difficulties mentioned above and also offers several other advantages. It permits

measurements of resistivity [133] in samples having a wide variety of shapes, including the resistivity of small volumes within bigger pieces of semiconductor. The basic experimental arrangement for the collinear four probe measurement is indicated in figure 2.10.

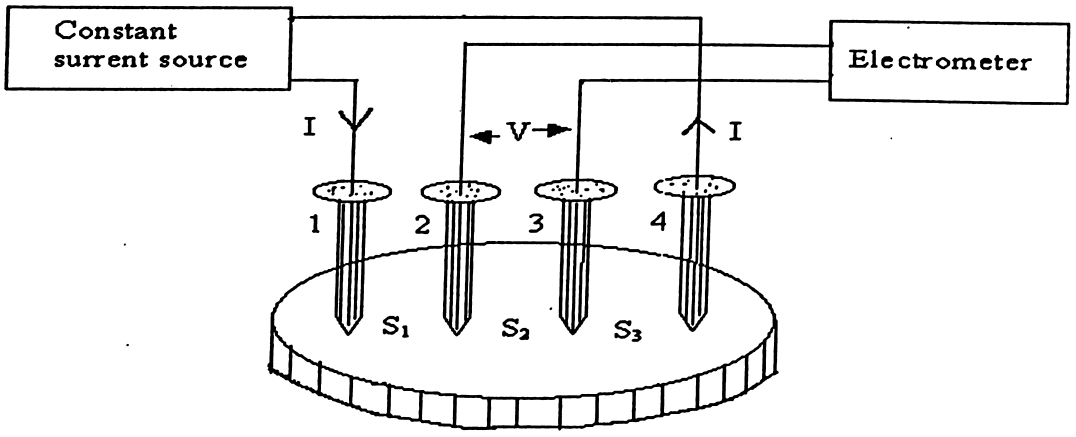

Figure 2.10: A collinear four probe setup for electrical resistivity measurement.

Four sharp probes are placed on a flat surface of the material to be measured. Current is passed through the outer electrodes and the floating potential is measured across the inner pair. If the flat surface on which the probes rest is adequately large and the sample is big, the semiconductor may be considered to be a semi-infinite volume [134, 135]. To prevent minority carrier injection and make good contacts, the surface on which the probes rest may be mechanically capped. The experimental circuit used for measurement is illustrated in figure 2.10, and the following points are assumed :

- The resistivity of the material is uniform in the area of measurement.
- There is no minority carrier injection into the semiconductor by the electrodes.
- The surface on which the probes rest is flat with no surface leakage.
- The four probes used contact the surface at points that lie in a straight line.

- The diameter of the contact between the metallic probes and the semiconductor is small compared to the distance between the probes.
- The boundary between the current carrying electrodes and the bulk material is hemispherical and small in diameter.
- The bottom surface of the semiconductor is non-conducting.

Let the four probes be spaced S_1, S_2 and S_3 apart. Current I is passed through the outer probes (1 and 4) and the floating potential V is measured across the inner pair of probes 2 and 3. The floating potential V_f at a distance r from an electrode carrying current I in a material of resistivity ρ_o is given by

$$V_f = \frac{\rho_o I}{2\pi r} \tag{2.14}$$

There are two current carrying electrodes numbered 1 and 4 and the floating potential V_f at any point in the semiconductor is the difference between the potential induced by each of the electrodes, since they carry currents of equal magnitude but in opposite directions [136, 137]. Thus

$$V_f = \frac{\rho_o I}{2\pi}\left(\frac{1}{r_1} - \frac{1}{r_4}\right) \tag{2.15}$$

where r_1 = distance from probe number 1 and r_4 = distance from probe number 4. The potentials at probe 2, V_{f2} and at probe 3, V_{f3} can be calculated from relation (2.15) by substituting the proper distances as follows

$$V_{f2} = \frac{\rho_o I}{2\pi}\left(\frac{1}{S_1} - \frac{1}{S_2 + S_3}\right) \tag{2.16}$$

$$V_{f3} = \frac{\rho_o I}{2\pi}\left(\frac{1}{S_1 + S_2} - \frac{1}{S_3}\right) \tag{2.17}$$

The potential difference V between probes 2 and 3 is

$$V = V_{f2} - V_{f3} = \frac{\rho_0 I}{2\pi}\left(\frac{1}{S_1} + \frac{1}{S_3} - \frac{1}{S_2 + S_3} - \frac{1}{S_1 + S_2}\right) \tag{2.18}$$

and the resistivity ρ_o is computable as

$$\rho_o = \frac{V}{I}\frac{2\pi}{\left(\frac{1}{S_1} + \frac{1}{S_3} - \frac{1}{S_1 + S_2} - \frac{1}{S_2 + S_3}\right)}$$

When the point spacing is equal, that is $S_1 = S_2 = S_3 = S$, the above relation simplifies to

$$\rho_o = \frac{V}{I} 2\pi S \tag{2.19}$$

If the sample is in contact with a non conducting medium, a correction factor G_7 [which is a function (w/S)] is applied to ρ_0, in order to obtain the actual resistivity ρ, given by,

$$\rho = \frac{\rho_o}{G_7\left(\frac{w}{S}\right)} \tag{2.20}$$

where, $$G_7\left(\frac{w}{S}\right) = 1 + 4\frac{S}{w}\sum_{n=1}^{\infty}\left[\frac{1}{\sqrt{\left(\frac{S}{w}\right)^2 + (n)^2}} - \frac{1}{\sqrt{\left(\frac{2S}{w}\right)^2 + (2n)^2}}\right] \tag{2.21}$$

The function G_7 is tabulated in table [2.1] and plotted in figure 2.11. For smaller values

of w/S, the function G_7 approaches the case for an infinitely thin slice, or

$$G_7\left(\frac{w}{S}\right) = \frac{2S}{w}\log_e 2 \qquad (2.22)$$

Appropriate values of G_7 corresponding to the required w/S ratio were obtained from the polynomial fit shown in figure 2.11.

Table. 2.1: Correction factor G_7 as a function of w/S ratio.

Sl.no.	w/S	G_7(w/S)
1	0.1	13.863
2	0.141	9.704
3	0.2	6.931
4	0.33	4.159
5	0.5	2.78
6	1	1.504
7	1.414	1.223
8	2	1.094
9	3.333	1.0224
10	5	1.007
11	10	1.00045

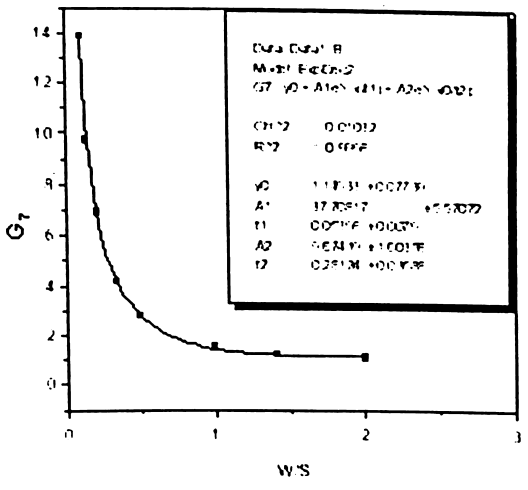

Figure 2.11: G_7 for nonconducting surface.

Experimental setup

A compact and low cost dip-stick type cryostat has been designed and fabricated [138] for performing electrical studies on semiconductors. In this type of cryostat, the sample chamber is immersed in a cryogenic liquid (such as liquid nitrogen) [139]. In our design, a hollow brass cylinder measuring 45 mm in diameter and 110 mm in length is suspended from a brass flange by a thin walled seamless stainless steel tube of 20 mm bore and 0.2 mm wall thickness. The top end of the tube terminates in a KF 25 vacuum coupling. This cryostat assembly could be inserted into any standard liquid nitrogen cryocan (with neck aperture of 50mm). A schematic diagram of the cryostat assembly is shown in Figure

2.12. The sample holder which is inside the brass cylinder, consists of a copper block of 20 mm diameter and 25 mm length and a collinear four probe of distance less than 1mm. A 20 W nichrome heater is embedded in a niche carved out inside of the copper block. A calibrated micro PT-100 temperature sensor is embedded in the copper block. 34 SWG enameled copper wires provide the necessary electrical connections between a high vacuum electrical feed-through at the top flange and the sample holder. An indium O-ring between the bottom flange and the brass cylinder constitutes a demountable vacuum coupling. Tests showed that the cryostat assembly could be evacuated $3x10^{-2}$ mbar with the help of a rotary pump. The sample holder could be cooled down to 90K using a liquid nitrogen bath. Passage of 350 mA current from a 15V d.c. power supply was sufficient to raise the temperature of the sample holder to 480 K. The resistivity data on glassy semiconductors could be collected from 90 K to 480 K using this set-up.

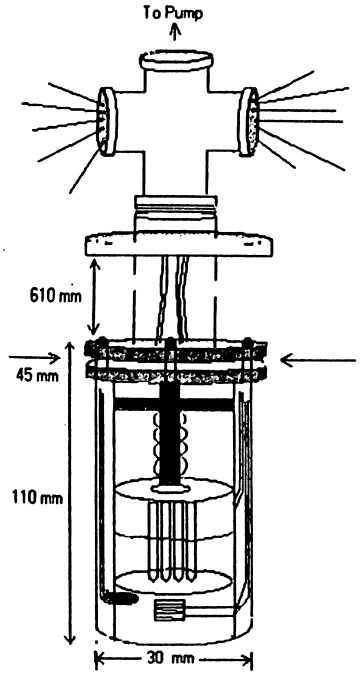

Figure 2.12: Schematic diagram of cryostat with a collinear four probe (not to scale).

Chapter 3

Investigations on V_2O_5-SnO-TeO_2 glasses

3.1. Introduction

It has already been pointed out in chapter 1 that literature survey shows that all known V_2O_5 based binary glasses are n-type semiconductors without exception [140, 141]. A recent report on the thermoelectric power measurements on V_2O_5-SnO-TeO_2 glass system revealed the possibility of obtaining a p-type semiconductor in this ternary glass system [70]. A single glass composition, namely, $20V_2O_520SnO60TeO_2$ prepared by them exhibited a small positive Seebeck coefficient of + 5μV K^{-1}, indicating that it was a p-type semiconductor in the otherwise n-type glass system. They reported the low temperature d.c. electrical conductivity of two glass compositions, namely, $50V_2O_5.20SnO.30TeO_2$ and $40V_2O_5.10SnO.50TeO_2$ [72]. From this study they showed that both the glass compositions exhibited small polaron hopping mechanism at high temperatures and a cross-over to variable range hopping mechanism at low temperatures. They studied the d.c. electrical conductivity of the two glass samples after annealing the samples at a temperature below T_g for periods ranging from 6 hours to 48 hours and analyzed the data using the Mott-Austin model [72]. The analysis of the low temperature data showed that there was only a small variation in the values of the Mott parameters $N(E_F)$ and R_{VRH} when the annealing time was changed from 6 hours to 48 hours. Annealing had no effect on the high temperature electrical conductivity [111]. However, the high temperature d.c. electrical conductivity study revealed that glasses with V_2O_5 mol % ≥ 50 exhibited adiabatic small polaron hopping (SPH) mechanism where as the rest showed non-adiabatic SPH mechanism. T_g of $60V_2O_5.10SnO.30TeO_2$ and

$50V_2O_5.20SnO.30TeO_2$ glasses was reported as 497 K and 501 K respectively (without any mention of the heating rate under which these T_g measurements were made). Thus, there is no systematic study of any property of V_2O_5-SnO-TeO_2 glasses albeit the few performed by Mori et al. Johnson et al [142] have summarized the results of the earlier structural studies on tellurite glasses. They concluded that $90V_2O_5.10TeO_2$ glass contained structural units (distorted trigonal bipyramids) similar to crystalline β-TeO_2.

3.2. Exploration of the glass-forming region

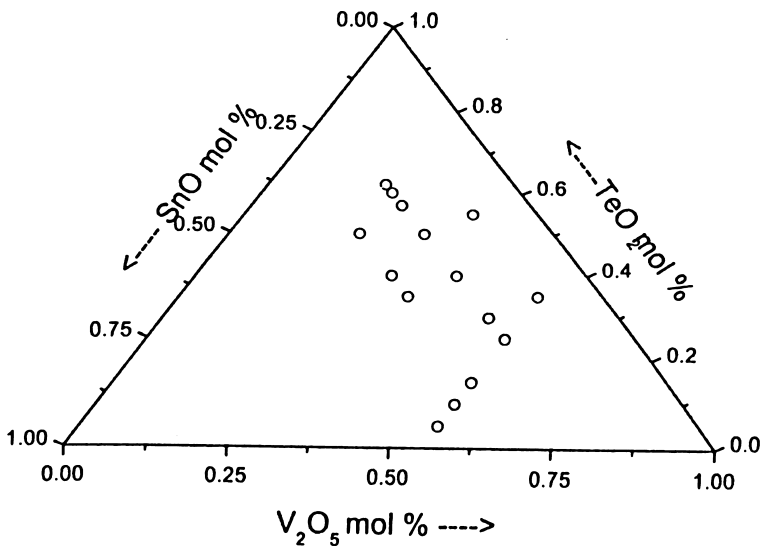

Figure 3.1: Glass forming region of $xV_2O_5.ySnO.(100-x-y)TeO_2$ glasses explored.

The extent of the glass-forming region (GFR) of the V_2O_5-SnO-TeO_2 system is not known. As part of the present investigations, a wide range of $xV_2O_5.ySnO.(100-x-y)TeO_2$ glasses with $18 \leq x \leq 50$; $10 \leq y \leq 35$ were prepared with an intention to explore the variation of thermo electric power (Q) in these glasses. Measurements showed that glasses with increasing values of negative Q (n-type) were obtained as one increased x (V_2O_5 content) keeping y (SnO content) constant. The same observation was also made

when y (SnO content) was varied between 10 and 35 mol % SnO. This was sufficient to establish the trend in Q with a variation of x and y in these glasses. This led to the conclusion that p-type could be prepared only in $xV_2O_5.20SnO.(80-x)TeO_2$ glasses for $x \leq 20$. However, homogeneous glasses could not be prepared with $x<18$ mol % V_2O_5. Figure 3.1 shows the glass-forming region of V_2O_5-SnO-TeO_2 system explored in the present investigation.

3.3. Preparation

Glass samples of the system $xV_2O_5.20SnO.(80-x)TeO_2$ ($18 \leq x \leq 50$) used in the present investigations were prepared by melt quenching technique. Appropriate amounts of high purity V_2O_5 (99.9 % purity), SnO (99.9% purity) and TeO_2 (99.99% purity) were weighed in an analytical balance with 0.01mg resolution and thoroughly mixed by continuously kneading for about 15 to 20 min. The well-mixed oxide mixture was then transferred to a porcelain crucible and melted at about 750 °C in an electric furnace. The melt was held at this temperature for about 3 hours before press quenching the same between two thick copper plates. The as quenched sample was in the form of a platelet of about 1 mm thickness. Identical preparation conditions such as furnace temperature and quenching procedure were followed while preparing the entire series of glasses. Glass samples of the sample composition were repeatedly prepared to ensure repeatability.

3.4. Characterisation

Prior to further investigations, all the V_2O_5-SnO-TeO_2 glasses prepared were checked for amorphous nature by studying their X-ray powder diffraction (XRD) patterns. In the present investigations, a Seifert XRD 3003 T/T X-ray powder diffraction system was

used as explained in chapter 2. A typical XRD pattern from a V_2O_5-SnO-TeO_2 glass is shown in figure 3.2.

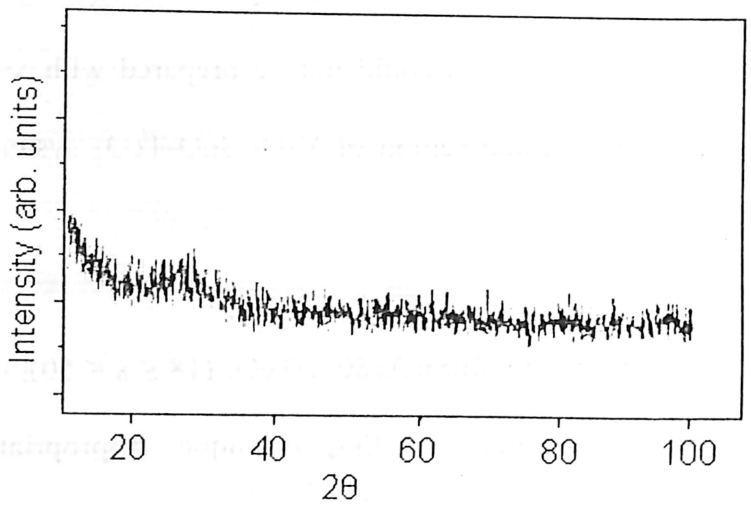

Figure 3.2: X-ray diffraction pattern of a typical V_2O_5-SnO-TeO_2 glass

The diffractogram of the as quenched glass samples showed no sharp peaks signifying the lack of crystallinity. All the glasses studied in this chapter showed amorphous nature in their XRD patterns. XRD patterns can only show if the sample is crystalline or amorphous. The experimental observation of the glass transition temperature (T_g) is necessary to classify the sample as a glass. The DSC curves were recorded for all the glasses. The DSC curves showed an endothermic base line shift corresponding to the glass transition temperature. It confirmed that the prepared samples are good glasses. All the V_2O_5-SnO-TeO_2 glasses showed a glass transition temperature in between 200 °C and 300 °C, when heated at a constant heating rate of 10 °C min^{-1}. The DSC data and results will be presented in the sub-chapter on DSC studies. Thermoelectric power (TEP) measurements were performed on all the V_2O_5-SnO-TeO_2 glass samples in order to

identify the majority charge carrier type. The TEP data is presented and discussed in the following sub-chapter.

3.5. Thermoelectric power and vanadium ion concentration

Thermoelectric power (TEP) measurements were performed on the $xV_2O_5.20SnO.(80-x)TeO_2$ glasses with x = 18, 20, 23, 30 40, 50 using the experimental technique discussed in the second chapter. The TEP data was used to determine the majority charge carrier type in the glasses. The TEP data is shown in table 3.1. The data given in parenthesis in the second column correspond to the data reported by Mori et al [70]. Q values obtained for $xV_2O_5.20SnO.(80-x)TeO_2$ glasses showed that for glasses with x = 18 mol % V_2O_5 and x = 20 mol % V_2O_5, the Seebeck coefficient, $Q > 0$ indicating that these two compositions are p-type semiconductors. The rest of the glasses (x = 23, 30, 40, 50) showed $Q < 0$ and hence they are n-type semiconductors. Q is related to the high and low vanadium ion concentration ratio (V^{5+}/V^{4+}) as defined by the relation (1.32).

In order to verify the applicability of relation (1.32), the concentration of the vanadium ions was estimated for all the glasses by iodometry method following the titration procedure described in second chapter (data shown in table3.1). From these estimations it was concluded that compositions with x = 18 and 20 mol % V_2O_5 glasses showed (V^{5+}/V^{4+}) < 1 and hence these two glasses are p-type semiconductor. The rest of the glasses (x = 23, 30, 40, 50 mol % V_2O_5) showed (V^{5+}/V^{4+}) >1 and hence these glasses are n-type semiconductors. A comparison of Q and Q' {Seebeck coefficient calculated from relation (1.32)} shows that the empirical relation (1.32) between Q and (V^{5+}/ V^{4+}) ratio is valid for this glass system (shown in table 3.1). This leads to the conclusion that V_2O_5-SnO-TeO_2 glasses with excess V^{4+} ions would invariably be p-type

semiconductors. Although it is difficult to control the ratio of the vanadium ions during preparation, glasses prepared under a reducing atmosphere would probably be p-type semiconductors.

The highest positive Q value that could be obtained in this glass system was +7 $\mu V.K^{-1}$. Figure 3.3 shows the composition dependence of the Seebeck coefficient measured at 473 K. The solid line in the figure represents a straight line fit (least squares fit) to the data. From the TEP data, it could be concluded that the majority charge carrier reversal (MCCR) occurs at a composition in between 20 and 23 mol % V_2O_5 in the $xV_2O_5.20SnO.(80-x)TeO_2$ glass system.

Table 3.1: Seebeck coefficient Q(measured), Q′(calculated), activation energy for thermal conduction ΔE_s and vanadium ion ratio of V_2O_5-SnO-TeO_2 glasses (values given in parenthesis are those reported by Mori et al [70])

Glass composition (mol %) V_2O_5 : SnO : TeO_2	Q (μVK^{-1})	$\frac{V^{5+}}{V^{4+}}$	Q′ (μVK^{-1})	ΔE_s (meV)
18 : 20 : 62	+7 (--)	0.91 (--)	+8	0.58
20 : 20 : 60	+5 (+5)	0.93 (0.94)	+6	0.56
23: 20 : 57	-21 (--)	1.23 (--)	-18	0.53
30 : 20 : 50	-44 (-42)	1.58 (1.60)	-39	0.52
40 : 20 : 40	-64 (-67)	2.16 (2.10)	-66	0.50
50 : 20 :3 0	-175 (-178)	7.97 (7.55)	-179	0.49

Q verses 1000/T plots for various compositions of $xV_2O_5.20SnO.(80-x)TeO_2$ glasses are shown in figure 3.4. The dotted lines are the least squares fit to the data. It is evident from figure 3.4 that Q exhibits a weak dependence on temperature. This weak temperature dependence of Q has been observed in a host of V_2O_5 based glasses [13] and appears to be a typical characteristic of this class of glassy semiconductors. Figure 3.5 shows the variation of E_s (determined from the slope of figure 3.4) as a function of V_2O_5 mol %.

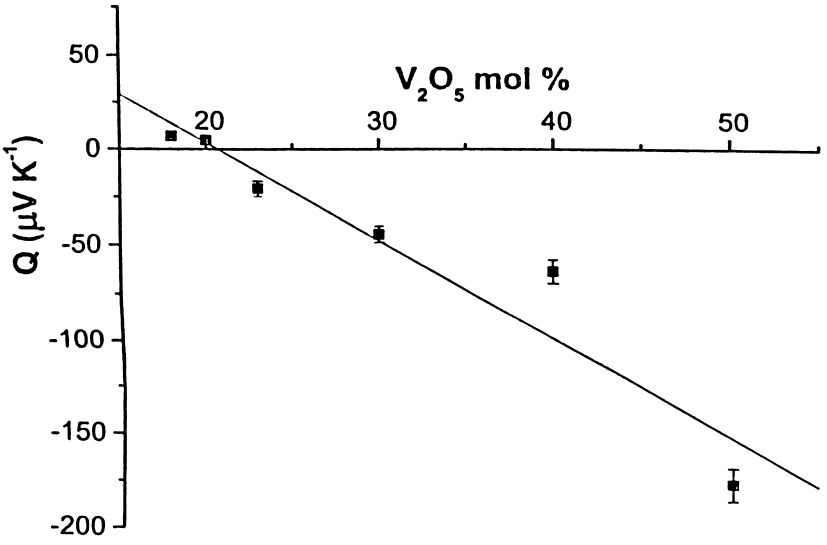

Figure 3.3: Variation of Q of $xV_2O_5.20SnO.(80-x)TeO_2$ glasses (measured at 473 K) with V_2O_5 mol %. The solid line is the least squares fit to the data.

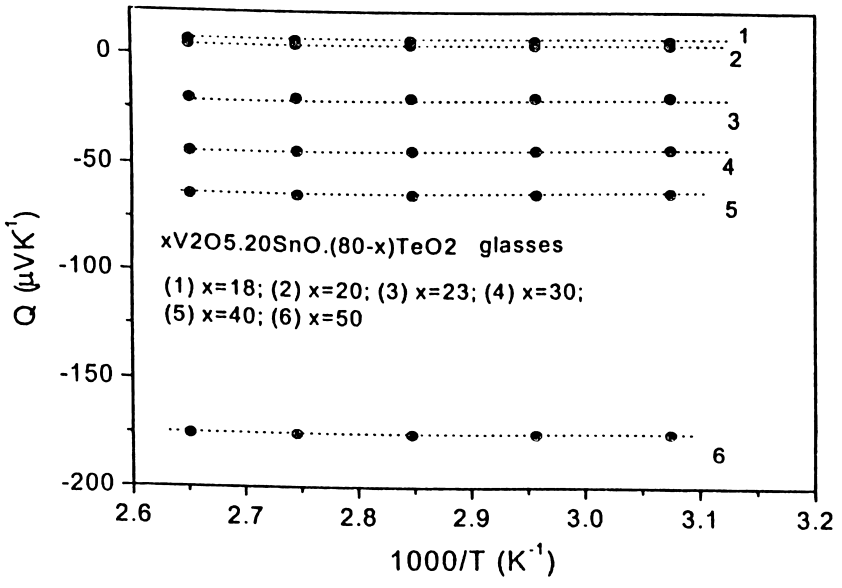

Figure 3.4 Q verses 1000/T for $xV_2O_5.20SnO.(80-x)TeO_2$ ($18 \leq x \leq 50$) glasses. Dotted lines correspond to the least squares fit to data.

The thermal activation energy decreases as V_2O_5 mol % increases. This observation predicts that the thermal conduction of the glasses increases as V_2O_5 mol % increases in the $xV_2O_5.20SnO.(80-x)TeO_2$ ($18 \leq x \leq 50$) glass system. It is interesting to note a subtle

change of slope in the E_s data at x = 23 mol % V_2O_5. One can conclude that the thermal conductivity of the glasses in this system shows a subtle but perceptible change when the carrier type changes from p-type to n-type. In other words, this can be inferred as a subtle signature of the MCCR phenomenon. This is not surprising since thermal conductivity and electrical properties are both structure sensitive properties.

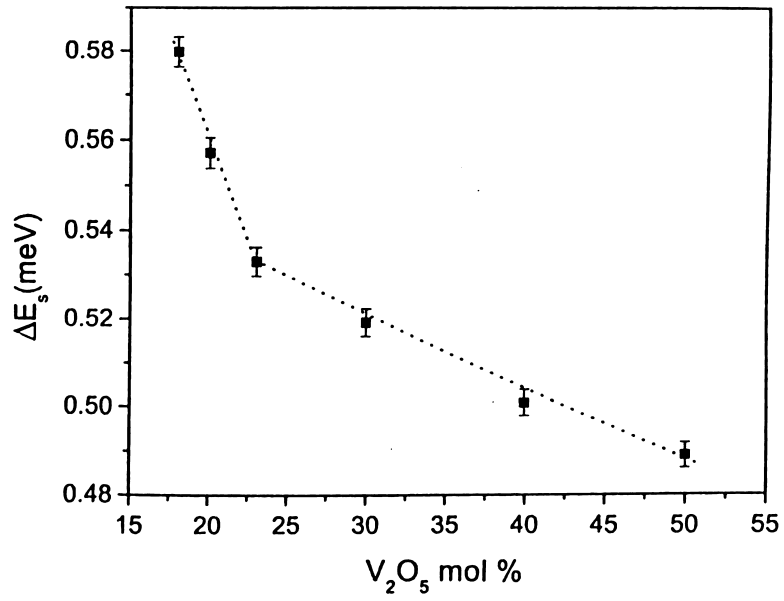

Figure 3.5: Thermal activation energy ΔE_S of $xV_2O_5.20SnO.(80\text{-}x)TeO_2$ glasses.

3.6. Other physical properties

Since the physical properties of the $xV_2O_5.20SnO.(80\text{-}x)TeO_2$ glasses have not been systematically studied, attempts were made to measure a few physical properties relevant to the context of the present investigations. Density of the glass is required as an input for the estimation of the molar volume of oxygen ion. Knowledge of the variation of the optical band gap of these glasses with composition is relevant since these samples are amorphous semiconductors. Microhardness is a simple experimental technique that

provides information on the mechanical strength of the glass. With these issues in mind, physical properties such as density, optical band gap and microhardness of these glasses were measured.

3.6.1. Density

The density (ρ) measurements on V_2O_5-SnO-TeO_2 glasses were based on the Archimedes principal and were carried out using a density bottle with xylene as the immersion liquid. Each value reported is the average of at least three independent measurements (table 3.2). From the density data, the molar volume of the glasses were calculated (table 3.2) using equations (2.8) and (2.9). Figure 3.6 shows the composition dependence of density and molar volume of $xV_2O_5.20SnO.(80-x)TeO_2$ glasses. When V_2O_5 mol % increased, V_2O_5 molecules replace TeO_2 molecules. As the molecular weight of V_2O_5 (181.876) is more than the molecular weight of TeO_2 (159.598), one may expect the overall density of the glass to increase. But the molar volume increases as V_2O_5 mol % increases in the sense that the glassy network becomes expanded [35]. Hence on the whole, the density of the glass decreases as V_2O_5 mol % content increases.

Table 3.2: Optical band gap, density, molar volume and microhardness of $xV_2O_5.20SnO.(80-x)TeO_2$ glasses.

Composition (mol %) V_2O_5 : SnO : TeO_2	E_{opt} (eV)	Density (gm cm^{-3})	Mol.vol. (cm^3/mol)	VHN (kg mm^{-2})
18 : 20 : 62	2.95	4.61	34.41	246
20 : 20 : 60	2.94	4.54	35.04	232
23: 20 : 57	2.92	4.43	36.06	223
30 : 20 : 50	2.87	4.22	38.22	217
40 : 20 : 40	2.80	3.93	41.61	200
50 : 20 :3 0	2.75	3.66	45.29	169

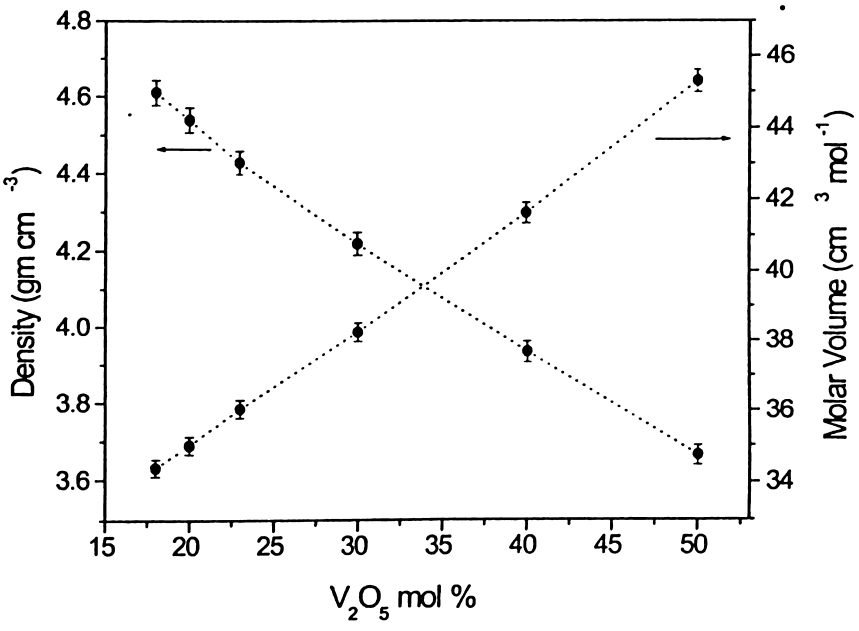

Figure3.6: Composition dependence of density and molar volume of $xV_2O_5.20SnO.(80- x)TeO_2$ ($18 \leq x \leq 50$) glasses.

3.6.2 Optical band gap

The optical band gap of $xV_2O_5.20SnO.(80- x)TeO_2$ glasses with x = 18, 20, 23, 30, 40, 50 has been measured using a dual beam uv-vis-nir spectrophotometer as explained in chapter 2. It was already pointed out that in high absorption region, the absorption coefficient $\beta(\nu)$ follows a power law behaviour {relation (2.11)}. The absorption coefficient data for the entire wavelength region mentioned above was used to plot $(\beta h\nu)^{1/2}$ versus $(h\nu)$ curves corresponding to r = 2. A typical plot is shown in figure 2.6. The linear fit to the high hν data was extrapolated to $(\beta h\nu)^{1/2} = 0$. The x-intercept gives the optical band gap of the semiconducting glass. The optical band gap calculated for the V_2O_5-SnO-TeO_2 glasses are shown in table 3.2. The optical band gap of $xV_2O_5.20SnO.(80-x)TeO_2$ ($18 \leq x \leq 50$) glasses varied from 2.95 eV to 2.75 eV. The

variation of the optical band gap with V_2O_5 mol % is shown in figure 3.7. The optical band gap decreases as the average molecular weight increases for $xV_2O_5.20SnO.(80-x)TeO_2$ $(18 \leq x \leq 50)$ glasses. Decrease in band gap with increase in average molecular weight has been observed in chlorophosphate glasses [127]. Neena Chopra et al [143] have obtained the electron paramagnetic resonance (EPR) spectra of vanadium tellurite glasses. They reported a decrease in the covalency of the V-O bond with an increase in V_2O_5 content in this glass system. In the $xV_2O_5.20SnO.(80-x).TeO_2$ series of glasses, SnO content remains constant while V_2O_5 is increased at the expense of TeO_2. Hence one can say that the covalency of the V-O bond in $xV_2O_5.20SnO.(80-x).TeO_2$ decreases as V_2O_5 mol % is increased. The decrease in covalency increases the number of non bridging oxygens in the glass [35]. An increase in the number of non-bridging oxygens reduces the average chemical bond strength of the glass which in turn shifts the absorption edge to longer wavelength side [18]. Thus, the optical band gap decreases as V_2O_5 content increases in the V_2O_5-SnO-TeO_2 glasses.

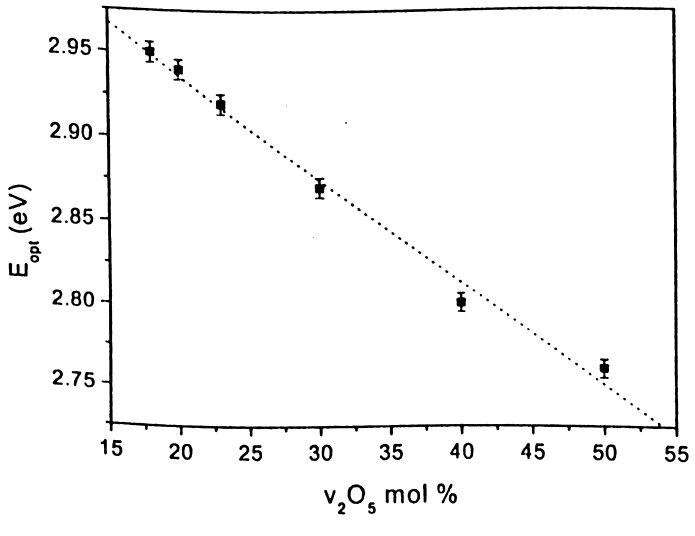

Figure 3.7: Variation of optical band gap of V_2O_5-SnO-TeO_2 glasses.

3.6.3. Microhardness

The microhardness of glasses has been measured following the procedure outlined in second chapter. All glass samples were uniformly subjected a load of 100 gm for a duration of 15 seconds. Figure 3.8 shows a typical indentation made on a V_2O_5-SnO-TeO_2 glass.

The measured microhardness values are tabulated in table 3.2. Each value quoted is the average of at least ten independent measurements. Figure 3.9 shows the variation of hardness value with the V_2O_5 mol % content in the $xV_2O_5.20SnO.(80- x)TeO_2$ ($18 \leq x \leq 50$) glasses. It shows that the VHN decreases as the V_2O_5 mol % content is increased. It has already been pointed out in the discussion on the optical band gap of these glasses that it is expected that the number of non-bridging oxygens increases in $xV_2O_5.20SnO.(80- x)TeO_2$ glasses when the V_2O_5 content in the glass is increased. When the number of non-bridging oxygens in a glass increases, the elastic moduli of the glass decreases [35]. From equation (1.42) it is obvious that a decrease in the elastic moduli decreases the microhardness, which the behaviour exhibited by the $xV_2O_5.20SnO.(80-x)TeO_2$ depicted in figure 3.9.

The composition dependence of microhardness can also be interpreted from the thermodynamic view-point. The lower the softening point T_d, the lower is the microhardness value [107]. Since softening point follows the same behavior as the glass transition temperature T_g (table 3.3), a decrease in T_g with an increase in V_2O_5 mol % results in a decrease in the microhardness as shown in figure 3.9. It is interesting to note the subtle slope change observed in the microhardness data (figure.3.9) near the glass composition with 23 mol % V_2O_5. A slope change in microhardness indicates changes occurring in the glassy network in the vicinity of this composition.

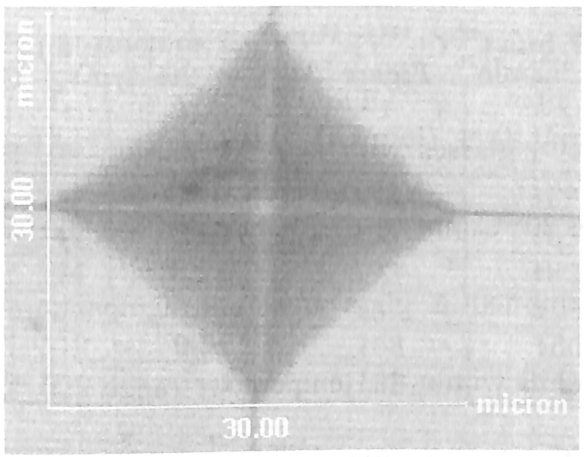

Figure 3.8: A typical indentation made on $50V_2O_5.20SnO.30TeO_2$ glass.

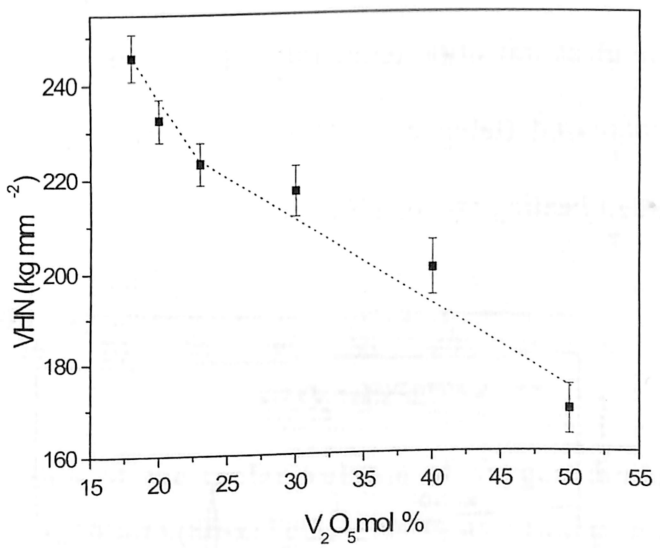

Figure 3.9: Composition dependence of VHN of $xV_2O_5.20SnO.(80- x)TeO_2$ glasses.

3.7. DSC studies

DSC studies on $xV_2O_5.20SnO.(80-x)TeO_2$ glasses with x = 18, 20, 23, 30, 40, 50 have been performed following the procedure explained in the chapter 2. The experiments were performed with ~ 20 mg samples. The DSC curves were recorded over a

temperature range of 50 °C to 450 °C for different heating rates 10 °C.min^{-1}, 15 °C.min^{-1}, 20 °C.min^{-1} and 30 °C.min^{-1}. Figure 3.10 is the typical DSC curve obtained for $xV_2O_5.20SnO.(80\text{-}x)TeO_2$ glasses with x = 18, 20, 30, 40, 50 mol % V_2O_5 under a constant heating rate of 20 °C.min^{-1}.

All glasses exhibited a glass transition temperature marked by a distinct endothermic baseline shift within the temperature range 200 °C to 300 °C. On heating beyond the glass transition temperature, the glass sample with composition x = 50 mol % exhibited a sharp crystallization peak, where as the other glass compositions showed weak crystallization peaks. Such multiple crystallization exotherms and melting endotherms have been observed in multi component oxide glasses such as V_2O_5-SrO-B_2O_3 [144, 145]. The glass transition temperature (T_g) of these glasses decreased as the V_2O_5 content was increased (table 3.3). The T_g and ΔC_P values shown in table 3.3 correspond to a constant heating rate of 10°C/min.

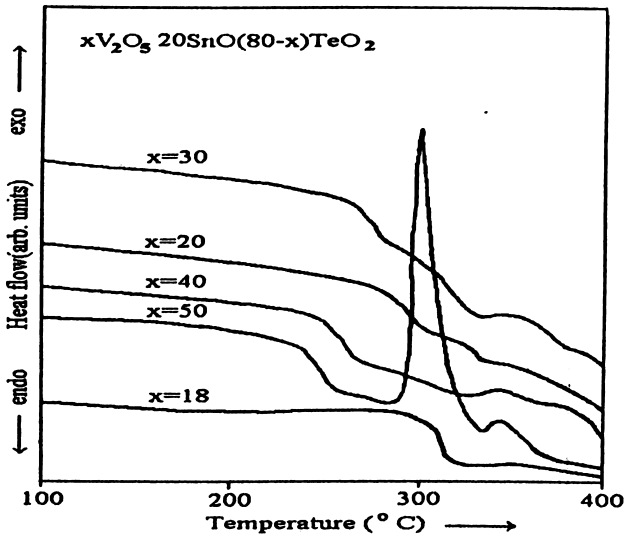

Figure 3.10: DSC curves for $xV_2O_5.20SnO.(80\text{-}x)TeO_2$ glasses (φ = 20 °C.min^{-1}).

Table 3.3: Calorimetric parameters, $C_V = V^{4+}/(V^{4+}+V^{5+})$ and V_o^* data.

Composition (mol. %) V_2O_5 : SnO : TeO_2	T_g (K)	ΔCp ($Jg^{-1}deg^{-1}$)	E_T (KJ/mol)	E_K (KJ/mol)	C_V	V_o^* ($cm^3.mol^{-1}$)
18 : 20 : 62	552	0.49	198	189	0.524	15.2
20 : 20 : 60	549	0.50	195	185	0.518	15.1
23: 20 : 57	544	0.51	192	182	0.448	14.9
30 : 20 : 50	534	0.52	181	173	0.388	14.6
40 : 20 : 40	519	0.81	168	160	0.317	14.3
50 : 20 :3 0	504	0.94	158	149	0.111	13.9

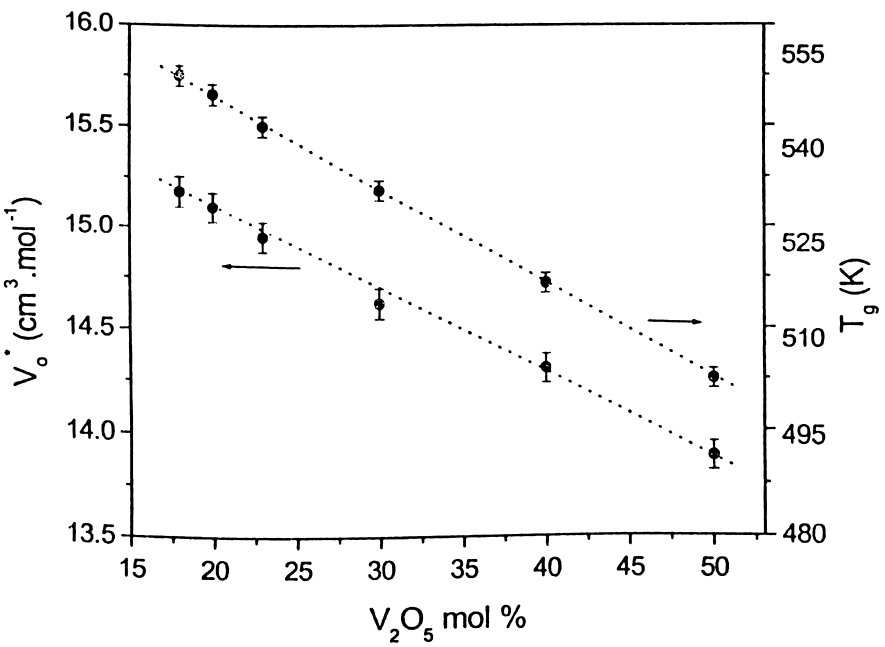

Figure 3.11: Variation of the molar volume of oxygen ion and glass transition temperature of $xV_2O_5.20SnO.(80-x)TeO_2$ glasses as a function of V_2O_5 mol %.

The molar volume of oxygen ions V_o^* for $xV_2O_5.20SnO.(80-x)TeO_2$ glasses with x = 18, 20, 23, 30, 40, 50 was calculated using the equation,

$$V_o^* = \frac{[M(V_2O_5) - 16C_v]x + M(TeO_2)y + M(SnO)z}{[\rho(5 - C_v)x + 2y + z]} \qquad (3.1)$$

where ρ is the density of the glass composition, $C_V = V^{4+} / (V^{5+}+V^{4+})$, x,y,z and $M(V_2O_5)$, $M(TeO_2)$, M(SnO) are the molar fraction and molecular weight of V_2O_5, TeO_2

and SnO respectively. The calculated V_o^* values of the V_2O_5-SnO-TeO_2 glasses are shown in table 3.3. V_o^* values varied from 15.2 to 13.9 $cm^3.mol^{-1}$ as V_2O_5 content was varied from 18 to 50 mol %. T_g of the glasses increased with an increase in V_o^* (and TeO_2 mol. %). In the case of $V_2O_5.4Sb_2O_3.(96\text{-}x)TeO_2$ glasses [71], V_o^* decreased from 14.6 cm^3mol^{-1} to 13.1 cm^3mol^{-1} when TeO_2 mol. % was varied from 62 to 11 mol. %. T_g of $V_2O_5.4Sb_2O_3.(96\text{-}x)TeO_2$ glasses increased with an increase in TeO_2 mol. % mimicking the behavior reported in the present studies. The increase in T_g with an increase in the value of V_o^* {figure 3.11} indicates that the glass structure turns more loosely packed with an increase in TeO_2 mol. %. Similar trend in T_g has been observed in other loosely packed tellurite glasses [147, 147]. A comparison of V_o^* of $V_2O_5.20SnO.(80\text{-}x)TeO_2$ glasses (13.9 to 15.2 cm^3mol^{-1}) with that of $xV_2O_5.6Bi_2O_3.(94\text{-}x)TeO_2$ glasses (13.0 to13.7 cm^3mol^{-1}[148]), $V_2O_5.10ZnO.(90\text{-}x)TeO_2$ glasses (13.3 to 14.5 cm^3mol^{-1} [13]) and $V_2O_5.4Sb_2O_3.(96\text{-}x)TeO_2$ glasses (13.1 to 14.5 cm^3mol^{-1} [72]) shows that the V_2O_5-SnO-TeO_2 glasses with relatively higher V_o^* values are thermally more unstable as compared to the rest.

Kissinger's {equation (2.1)} and Thakor's {equation (2.3)} methods were used for estimating the activation energy for the glass transition of various glass compositions. Kissinger's and Thakor's plots are shown in figure 3.12 and 3.13 respectively. The activation energies for glass transition E_K (Kissinger) and E_T (Thakor) were calculated (table 3.3, figure 3.14) from the slope of the least squares fit of the corresponding plots. It can be seen that $E_T > E_k$ for all the glasses as expected from theoretical predictions [118, 149]. The activation energies E_K and E_T decrease with an increase in V_2O_5 mol %. This

indicates that the glass-supercooled liquid transition becomes less hindered in glasses with higher V_2O_5 content.

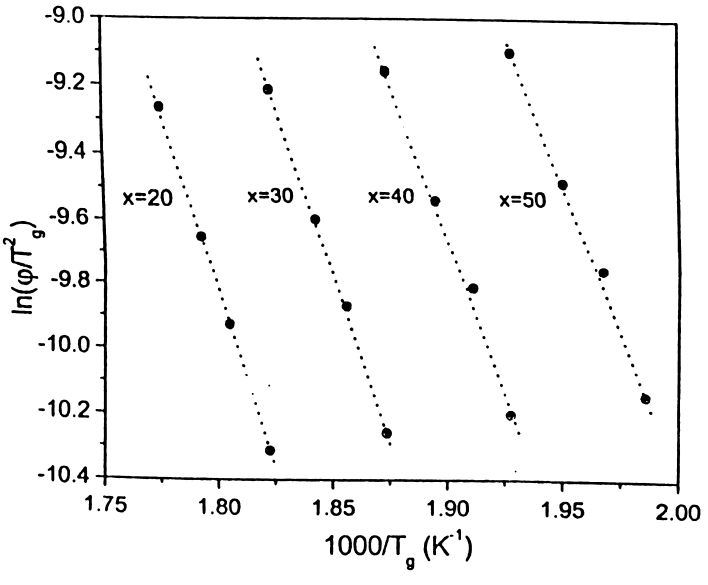

Figure 3.12: Kissinger's plots for $xV_2O_5.20SnO.(80-x)TeO_2$ glasses.

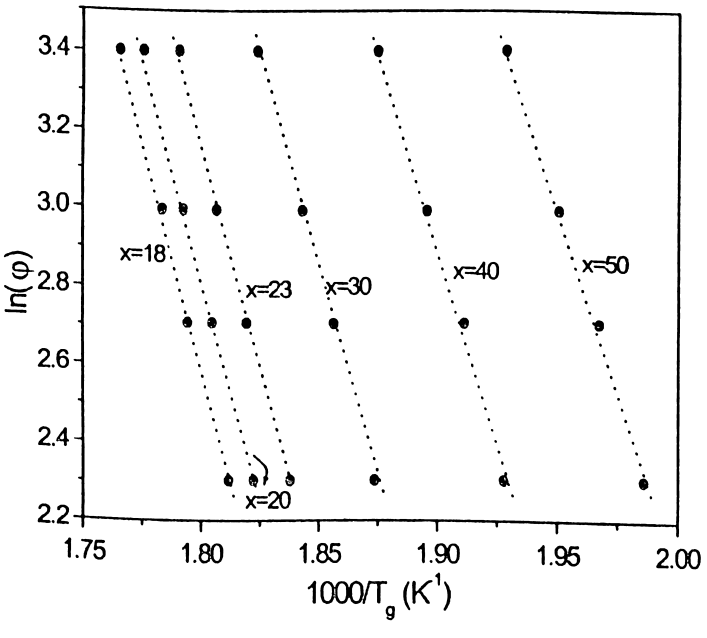

Figure 3.13: Thakor's plots for $xV_2O_5.20SnO.(80-x)TeO_2$ glasses.

Figure 3.15 shows the typical variation of the excess heat capacity at T_g, ΔC_p with V_2O_5 mol %. The dotted line in the figure merely connects the adjacent data points. It can be seen that ΔC_p has a small value for composition with 18 mol % of V_2O_5 and 20 mol % V_2O_5, but increases sharply near the composition with 30 mol % of V_2O_5. The p-type glasses exhibit the smallest ΔC_p whereas the n-type glasses show large ΔC_p values. Using the fragility concept introduced by Angel [21], the present data could be interpreted as follows. The variation of the excess heat capacity at T_g of these glasses with composition shows an abrupt change in the fragility of the glasses at x = 30 mol % V_2O_5. Thus an abrupt change in the fragility of the glass is observed close to the composition at which MCCR occurs in these glasses.

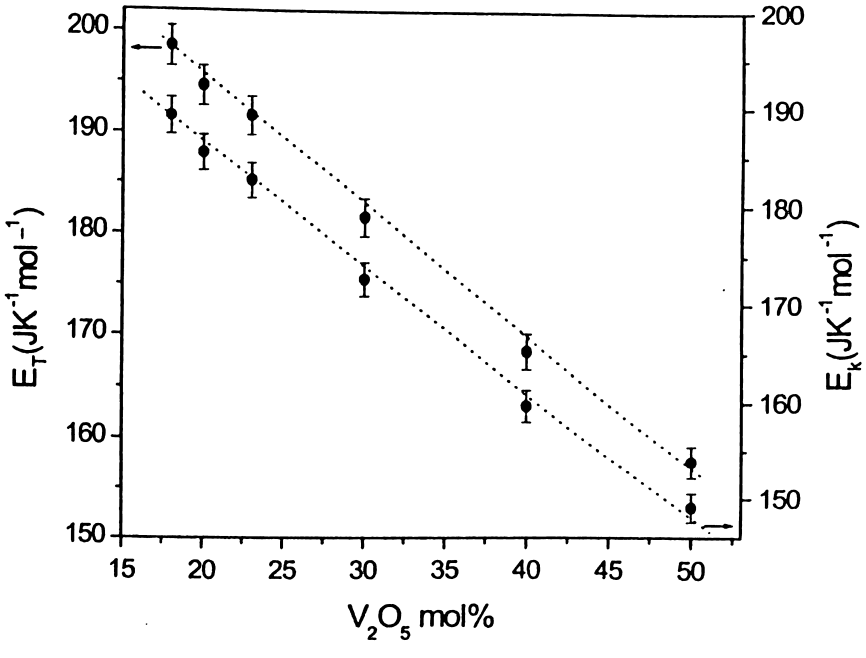

Figure 3.14: Activation energy of glass transition based on Kissinger's and Thakor's method (Dotted lines shown merely connect adjacent data points).

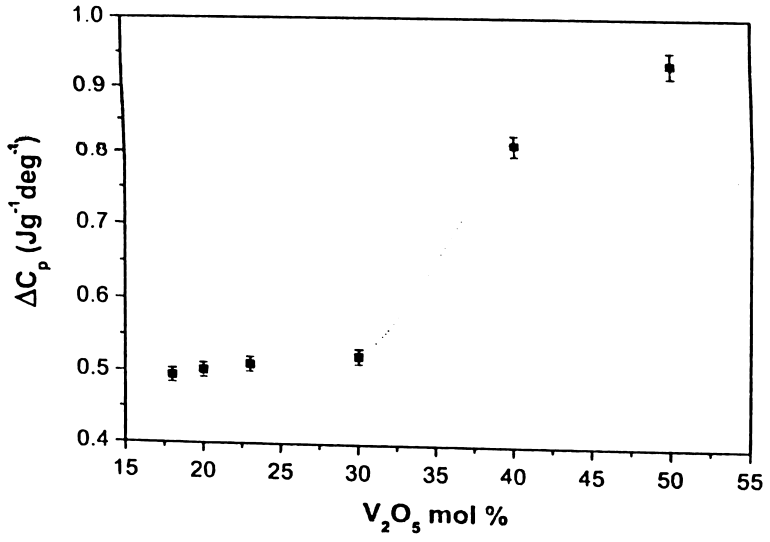

Figure 3.15: Excess heat capacity at glass transition of $xV_2O_5.20SnO.(80-x)TeO_2$ (18x50) glasses (Dotted line merely connects adjacent data points).

It is interesting to note that a structural parameter such as fragility undergoes an appreciable change near the composition at which the carrier reversal occurs. This leads one to suggest that the electronic phenomenon is associated either directly or indirectly with structural features of the glass.

3.8. d.c. electrical conductivity

The d.c. electrical resistivity data of $xV_2O_5.20SnO.(80- x)TeO_2$ with x = 18, 20, 23, 30, 40, 50 was collected from 100 K to 480 K. The data collection and analysis were carried out as per the procedure explained in chapter 2. To understand the conduction mechanism in the glasses of this system the data is analysed in terms of the Mott and Austin model {equation (3.2)}. From equation (3.2), a plot of $\ln(\sigma T)$ versus T^{-1} is expected to be linear. $\ln(\sigma T)$ versus T^{-1} plots for all the glasses covering a temperature range of 100 K to 480 K are shown in figure 3.16. Figure 3.16 indicates that a linear relationship exists in the plot only above room temperature. As the temperature goes down, the data show a deviation

from linearity. This clearly shows that the conductivity data below room temperature cannot be fitted to equation (3.2). Hence the conduction mechanism in these glasses is different in the low temperature and high temperature regions. Since the conduction mechanisms are different in these two temperature regimes, both these regimes would be treated separately.

Conduction in high temperature (SPH) regime

Mott-Austin proposed the variation of conductivity with temperature for small polaron hopping (SPH) mechanism in the high temperature region as

$$\sigma T = \sigma_o e^{-\frac{W}{k_B T}} \qquad (3.2)$$

where, W is the activation energy for conduction, T is the absolute temperature, k_B is the Boltzmann constant and the pre-exponential factor σ_o is given by ,

$$\sigma_o = \frac{C_V(1-C_V)\upsilon_o e^2}{R k_B} e^{(-2\alpha R)} \qquad (3.3)$$

where, ν_o (~ 10^{13} sec^{-1}) is the optical phonon frequency, C_V the ratio of the amount of reduced transition metal ion to that of total transition metal ion (V^{4+}/V^{tot}, $V^{tot} = V^{4+}+V^{5+}$), and α is the rate of wave function decay for the hopping electron, R the average spacing between transition metal ions.

To start the data analysis in SPH region, the activation energy for conduction (W, in equation 3.2) and the average spacing between transition metal ions (R, in equation 3.3) are needed. The average ion spacing R was estimated from the relation,

$$R = \left(\frac{1}{N}\right)^{\frac{1}{3}} \qquad (3.4)$$

where N is the density of metal ions. The density of metal ions N was calculated using the relation,

$$N = 2\left[\text{density} \times \left(\frac{\text{wt.}V_2O_5}{\text{Mol.wt.}V_2O_5}\right)N_A\right] \qquad (3.5)$$

The calculated N and R values are given in table 3.4 (the glass density values required in the calculation have been taken from table 3.2)

Table 3.4: Density of metal ion sites N, average ion spacing R, conductivity σ (at 473K), polaron band width j and the parameter Φ for V_2O_5-SnO-TeO_2 glasses.

Composition (mol. %) V_2O_5 : SnO : TeO_2	N ($x10^{27}m^{-3}$)	R ($x10^{-10}m$)	σ (at 473K) ($x10^{-5}\Omega^{-1}m^{-1}$)	j (eV)	Φ (eV)
18 : 20 : 62	6.3	5.4	2.6	0.00043	0.04
20 : 20 : 60	7.6	5.1	3.1	0.00042	0.04
23: 20 : 57	7.7	5.0	5.9	0.00057	0.04
30 : 20 : 50	9.4	4.7	11.3	0.0007	0.04
40 : 20 : 40	11.6	4.4	26.2	0.00083	0.04
50 : 20 :3 0	13.3	4.2	38.4	0.053	0.04

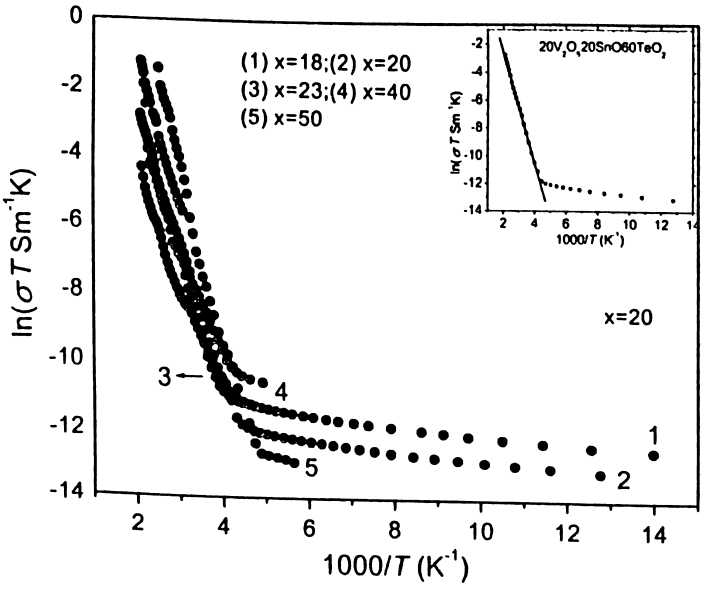

Figure 3.16: ln(σT) versus 1000/T plots for $xV_2O_5.20SnO.(80-x)TeO_2$ ($18 \le x \le 50$) glasses. Inset shows a typical fit of the data to relation (3.2) (Only one out of ten data points has been plotted in order to improve the clarity of the figure).

It was observed that the density of transition metal ions (N) in V_2O_5-SnO-TcO_2 glasses increases and distance between the metal ions decreases as V_2O_5 mol % content is increased. The same trend was reported by Qiu. et al [150] in vanadate glasses. The parameter W can be calculated from the slope of the least squares fit to ln(σT) versus 1000/T plots for all glasses. The SPH conduction mechanism can be either adiabatic SPH or non-adiabatic SPH mechanism, based on the value of polaron bandwidth (j).

The condition for adiabatic and non-adiabatic SPH is,

$$j > \Phi = (2k_B T W_H / \pi)^{1/4} (h\nu_o / \pi)^{1/2} \quad \text{adiabatic} \qquad (3.6)$$

$$j < \Phi = (2k_B T W_H / \pi)^{1/4} (h\nu_o / \pi)^{1/2} \quad \text{nonadiabatic} \qquad (3.7)$$

where $W_H = W - W_D/2$ (as $T > \theta_D/2$), θ_D is the Debye temperature $= h\nu_o/k_B \sim 478$ K for $\nu_o = 10^{13}sec^{-1}$. The value of φ was calculated from equation (3.6) and the value of j from the Holstein relation [68],

$$\sigma = \left(\frac{\pi e^2 j^2}{R h k_B T}\right)\left[\left(\frac{\pi}{W k_B T}\right)^{\frac{1}{2}} \frac{\mathrm{Sinh}\left(\frac{h\upsilon_o}{2k_B T}\right)}{\left(\frac{h\upsilon_o}{2k_B T}\right)}\right] e^{-\left(\frac{W+GW_P}{2k_B T}\right)} \qquad (3.8)$$

The calculated values of j and φ are shown in table 3.4. For the glass with 50 mol % V_2O_5, the values of j and φ were 0.053eV and 0.04eV. For this case, $j > \Phi$. Hence the conduction in $50V_2O_5.20SnO.30TeO_2$ glass is attributed to adiabatic small polaron hopping. For the rest of the glasses (ie., for x = 20, 23, 30, 40 mol % V_2O_5.), j value ranged from 8.3×10^{-4}eV to 4.3×10^{-4}eV and Φ value was approximately 0.04 eV. So for all these cases, $j < \Phi$. Hence, the conduction in these glass compositions is attributed to non-adiabatic small polaron hopping. Using j value one can calculate the mobility μ of non-adiabatic SPH. μ has different expressions for adiabatic and non-adiabatic SPH.

The adiabatic mobility of $50V_2O_5.20SnO.30TeO_2$ glass was calculated from,

$$\mu = \left(\frac{\upsilon_o c\ R^2}{k_B T}\right) e^{-\frac{W_H}{k_B T}} \qquad (3.9)$$

The adiabatic mobility of the x = 50 mol % V_2O_5 glass was estimated to be 3.1 x 10^{-11} m^2 $V^{-1}scc^{-1}$ at 473 K. The non-adiabatic mobility for the rest of the glasses (shown in table 3.5) was calculated using the relation [68],

$$\mu = \left(\frac{c\,R^2}{k_B T}\right)\left(\frac{2\pi}{h}\right)\left(\frac{\pi}{4W_H k_B T}\right)^{\frac{1}{2}} j^2 e^{-\frac{W}{k_B T}} \qquad (3.10)$$

The non-adiabatic mobility μ for the glasses ranged between 1.2 x 10^{-12} m^2V^{-1} sec^{-1} and 5.3 x 10^{-12} $m^2V^{-1}scc^{-1}$. This μ values could be compared with the values 4.1x10^{-12} to 7.8 x10^{-12} $m^2V^{-1}sec^{-1}$ reported by Mori et al [13] for the non-adiabatic mobility of V_2O_5-ZnO-TeO_2 glasses. Carrier concentration N_C was calculated for all the glasses from the mobility and conductivity data using the relation,

$$\sigma = N_C e \mu \qquad (3.11)$$

Table 3.5 : Activation energy for conduction W, non-adiabatic mobility μ, charge carrier concentration N_C for $xV_2O_5.20SnO.(80- x)TeO_2$ glasses showing non-adiabatic SPH conduction.

Composition (mol %) V_2O_5 : SnO : TeO_2	W (eV)	R (x10^{-10} m)	μ (x10^{-12} $m^2V^{-1}sec^{-1}$)	N_C (x10^{26} m^{-3})
18 : 20 : 62	0.382	5.4	1.21	1.4
20 : 20 : 60	0.380	5.1	1.23	1.7
23: 20 : 57	0.378	5.0	2.12	1.8
30 : 20 : 50	0.373	4.7	3.16	2.2
40 : 20 : 40	0.361	4.4	5.26	3.1

Using the adiabatic mobility of the x = 50 mol% V_2O_5 glass, N_C was found to be 7.83 x 10^{25} m^{-3}. For the rest of the glasses, N_C was calculated using non-adiabatic mobility (table 3.5). Figure 3.17 shows the relation between the vanadium ion average

distance R and activation energy for conduction W (table 3.5) for the glasses (x = 18, 20, 23, 30, 40 mol % V_2O_5) exhibiting non-adiabatic SPH conduction. An increase in W with an increase in R (as depicted in figure 3.17) is the general behaviour expected as per theoretical predictions [151, 152].

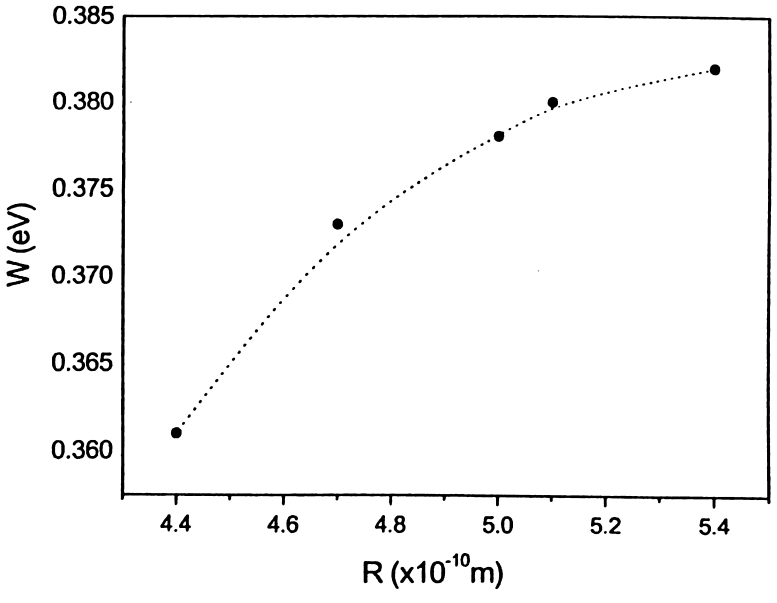

Figure 3.17: Effect of mean vanadium ion spacing R on activation energy W for conduction at T = 473 K for $xV_2O_5.20SnO.(80- x)TeO_2$ glass x = 18, 20, 23, 30, 40 (exhibiting non-adiabatic SPH conductivity)

Conduction in low temperature regime

In the above discussion, it was shown that the entire conductivity data could not be fitted to equation (3.2) for SPH conduction. The deviation from the Arrhenius behaviour at low temperature indicates that the conduction mechanism changes from SPH. The Mott-Austin model suggests that variable range hopping (VRH) mechanism dominates at low temperatures. The conductivity for the variable range hopping is given by,

$$\sigma = Be^{-A/T^{1/4}} \qquad (3.12)$$

where A and B are calculated from the expression,

$$A = 2.06\left[\frac{\alpha^3}{k_B N(E_F)}\right]^{\frac{1}{4}} \qquad (3.13)$$

$$B = \left[\frac{e^2}{2\sqrt{8\pi}}\right]\upsilon_o\left[\frac{N(E_F)}{\alpha k_B T}\right]^{\frac{1}{2}} \qquad (3.14)$$

Evidently, a linear plot of $\ln(\sigma T^{1/2})$ versus $T^{-1/4}$ signifies the occurrence of VRH conduction {equation (3.12)}. Figure 3.18 shows the $\ln(\sigma T^{1/2})$ versus $T^{-1/4}$ plots for glasses with x = 18, 20, 23, 40 and 50 mol % V_2O_5 respectively. The linearity observed in the plots in lower temperature region confirms that VRH conduction mechanism is dominant at these temperatures. Hence, the conductivity data in low temperature region was analyzed in the light of the Mott-Austin VRH mechanism. The slope change in the plots shown in figure 3.18 has been interpreted [73, 78] to be the signature of to the conduction change from SPH to VRH. All V_2O_5-SnO-TeO_2 glasses exhibited a cross-over from SPH to VRH conduction mechanism when the temperature was lowered.

Figure 3.18 highlights the temperature region of 150 K to 300 K, over which the change over from SPH to VRH occurs in these glasses. The transition temperature T_R at which the SPH to VRH cross over occurs was found from the intersection of the linear fits to the low temperature and high temperature data. The transition temperature T_R for the $xV_2O_5.20SnO.(80- x)TeO_2$ $(18 \le x \le 50)$ glasses varied between 207 K to 258 K (table 3.6). T_R exhibits a composition dependence, with the maximum value at x = 23 mol % V_2O_5. α and $N(E_F)$ were calculated from the slope and intercept values obtained from the linear fit to the low temperature ($T < T_R$) data using relations (3.13) and (3.14). The hopping distance R_{VRH} in VRH regime and hopping energy W_o are given by,

$$R_{VRH} = \left[\frac{9}{(8\pi\alpha N(E_F)k_B T)}\right]^{\frac{1}{4}} \qquad (3.15)$$

$$W_o = \frac{3}{(4\pi R^3_{VRH} N(E_F))} \qquad (3.16)$$

Table 3.6: Transition temperature T_R, density of states at Fermi energy $N(E_F)$, variable range hopping distance R_{VRH} and disorder energy W_d.

Composition (mol. %) V_2O_5 : SnO : TeO_2	T_R (K)	$N(E_F)$ ($m^{-3}eV^{-1}$ x10^{26})	R_{VRH} (nm)	W_d (eV)	αR_{VRH}
18 : 20 : 62	229	1.4	4.2	0.02	1.73
20 : 20 : 60	233	2.8	3.2	0.03	1.95
23 : 20 : 57	258	4.4	2.9	0.02	1.75
40 : 20 : 40	237	8.8	2.6	0.02	1.14
50 : 20 : 30	207	15.7	1.8	0.03	1.96

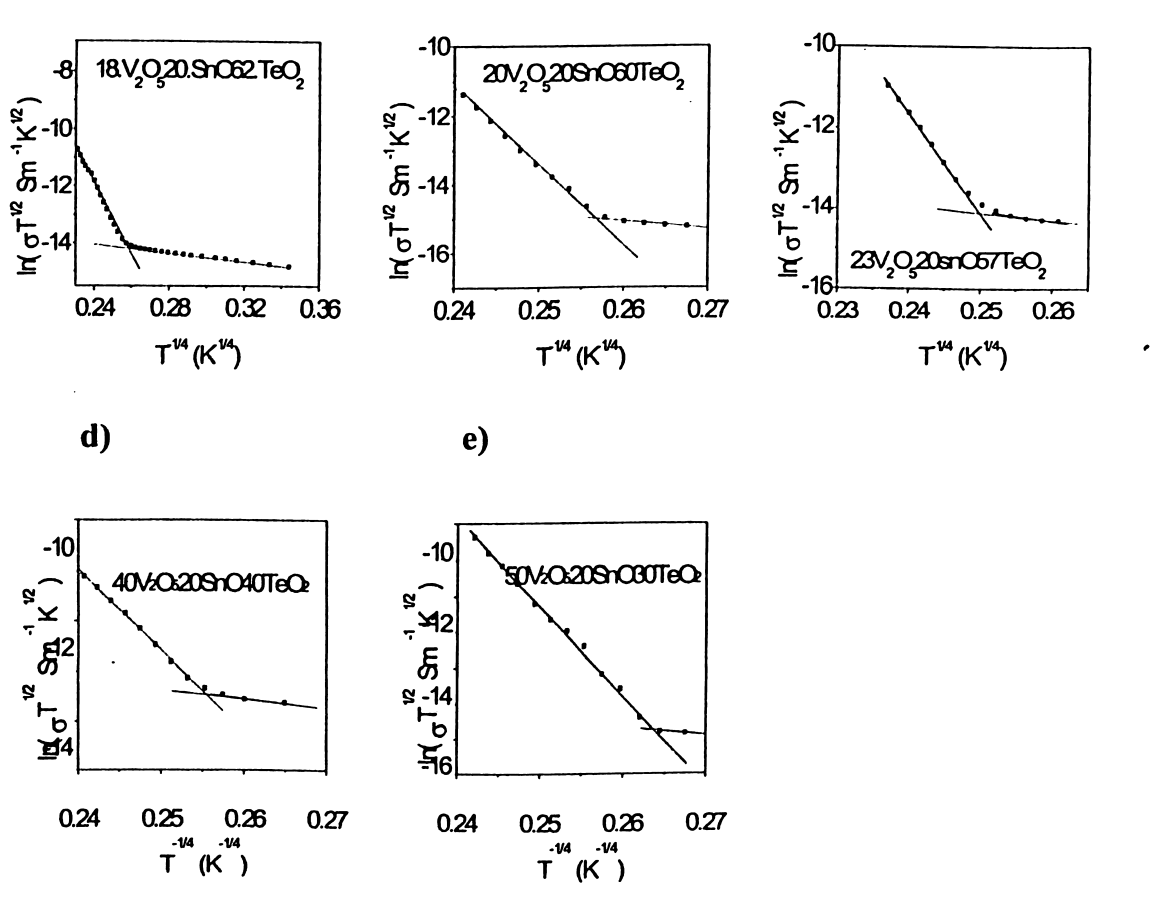

Figure 3.18: $\ln(\sigma T^{1/2})$ versus $T^{-1/4}$ plots for $xV_2O_5.20SnO.(80\text{-}x)TeO_2$ glasses. (Lines are least-squares fit to $T > T_R$ and $T < T_R$ data).

Based on the assumption that $W_o = W_d$ [153, 154, 155], the disorder energy W_d was calculated using equation (3.16). Mott parameters $N(E_F)$ and R_{VRH} for the glasses are

shown in table 3.6. Both $N(E_F)$ and R_{VRH} vary as a function of V_2O_5 mol. %. Figure 3.19 shows the variation of $N(E_F)$ and R_{VRH} with change in V_2O_5 mol %. While $N(E_F)$ increases with an increase in V_2O_5 mol %, R_{VRH} decreases as V_2O_5 mol % increases. The increase in $N(E_F)$ and decrease in R_{VRH} agrees with theoretical predictions [1, 67] and behavior [72] of V_2O_5 based glasses. Further, for the occurrence of VRH conduction, the requirement $\alpha R_{VRH} > 1$ and $W_d \geq k_B T$ (eg. $W_d \geq 0.019$ eV at 230 K) should be satisfied. Evaluation of present data at 230 K gave αR_{VRH} values ranging between 1.14 to 1.96 and W_d values 0.02 eV and 0.03 eV, which showed that the above criteria are satisfied. Hence the conduction mechanism in $xV_2O_5.20SnO.(80\text{-}x)TeO_2$ glasses (mol%) in the low temperature region is attributable to VRH.

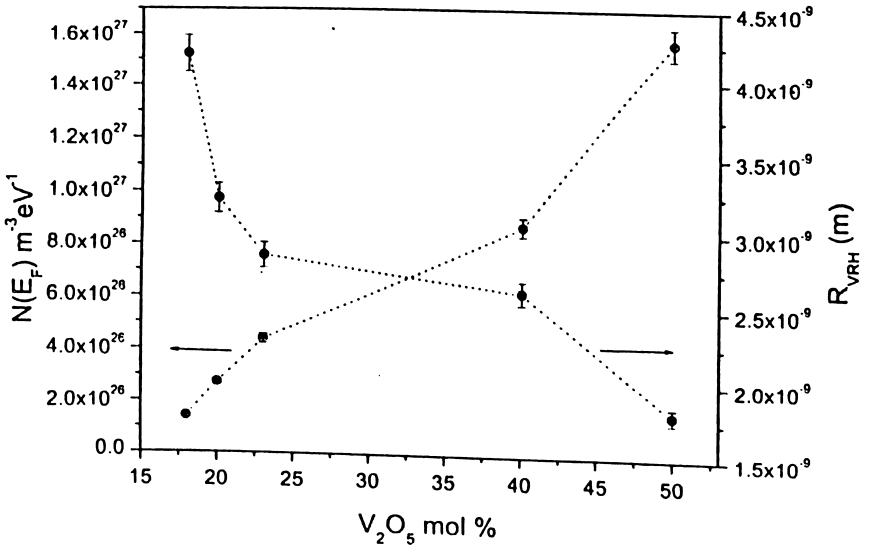

Figure 3.19: Variation of the density of states at Fermi energy $N(E_F)$ and the variable range hopping distance (R_{VRH}) as a function of V_2O_5 mol %.

From figure 3.19 it can be seen that density of states at the Fermi energy shows a gentle slope change near 23 mol % V_2O_5, whereas the hopping distance decreases sharply after this composition. These observations suggest that the low temperature electrical

conduction mechanism is sensitive to the majority charge carrier reversal phenomenon. The signature of the MCCR is more pronounced in chalcogenide glasses such as Bi-Ge-Se [156, 157] and Pb-Ge-Se(-Te) [87, 158, 159], which show large variations in measured physical properties at compositions at which the carrier reversal occurs.

3.9. Summary

The salient features of the studies on $xV_2O_5.20SnO.(80- x)TeO_2$ are summarized below.

I. The thermoelectric power measurements show the following features:

(i) Only glasses with x = 18 and 20 mol % V_2O_5 showed p-type conduction.

(ii) The TEP of all glasses exhibited weak temperature dependence.

(iii) The activation energy for thermo electric power, E_s showed a subtle slope changes close to the MCCR composition.

II. Density, microhardness and band gap measurements show the following features:

(i) Density decreased and molar volume increased with an increase in V_2O_5 content.

(ii) Microhardness decreased with increase in V_2O_5 content. A subtle slope change observed in microhardness at around 23 mol % V_2O_5.

(iii)The band gap E_{opt} decreased as the V_2O_5 mol % increased.

III. DSC studies give the following results:

(i) T_g decreased with a decrease in V_o^* (and V_2O_5 mol. %) indicating the characteristics of a loosely packed structure.

(ii) Activation energy of glass transition showed that the glass-supercooled transition is less hindered for glasses with higher V_2O_5 mol % .

(iii)The variation of the excess heat capacity at T_g of these glasses with composition showed that the fragility of the glasses increased abruptly after the MCCR composition. The p-type glasses showed the smallest ΔC_p values.

IV. d.c. electrical conductivity measurement gave the following results:

(i) The conduction mechanism in the high temperature regime is attributed to adiabatic SPH for x = 50 mol % V_2O_5 glass composition and non adiabatic SPH for the rest.

(i) All the glasses showed a changeover from SPH to VRH at a characteristic temperature when cooled below room temperature. SPH-VRH transition temperature T_R exhibits a composition dependence with the maximum value at x = 23 mol % V_2O_5

(ii) Mott parameter $N(E_F)$ increased and R_{VRH} decreased as V_2O_5 mol % was increased. $N(E_F)$ and R_{VRH} showed subtle changes in their values close to the composition at which the MCCR is observed in these glasses.

Chapter 4

Investigations on V_2O_5-CaO-P_2O_5 glasses

4.1. Introduction

Of the p-type glasses studied in the previous chapter, $18V_2O_5.20SnO.62TeO_2$ glass exhibited the highest Seebeck coefficient of +7 μV/K. Since this Q value is very low, it was attempted to explore P_2O_5-V_2O_5 based glasses exhibiting p-type conduction. Regions of glass formation in binary phosphate glasses showed that the maximum percentage of the second oxide in this glass system such as K_2O, Na_2O, Li_2O, BeO, MgO, CaO, SrO, BaO, Ag_2O, ZnO, CdO, PbO could be varied from 47 to 62 mol % [2, 160]. It was noted that homogeneous P_2O_5-CaO glasses could be prepared with a maximum of 56 mol % CaO. Grechanik and Munakata [161] reported the glass-forming region in V_2O_5-CaO-P_2O_5 system. Kennedy and Mackenzie [7] reported the possibility of obtaining p-type semiconductor glasses in the system V_2O_5-CaO-P_2O_5. Previous investigations have primarily concentration on the dependence of the electrical conductivity on the concentration of transition metal oxide in these glasses. The electrical resistivity of V_2O_5-CaO-P_2O_5 glasses was studied [7] in the temperature range of 25 °C to 400 °C. The resistivity of the glasses at 300 °C was determined to be 9 x 10^4 ohm–cm. The influence of V^{5+}/V^{4+} ratio on the electrical conductivity of these glasses has been pointed. The network former content had no effect on the Seebeck coefficient of these glasses. The reported values of electrical resistivity of the V_2O_5-CaO-P_2O_5 glasses ranged between 1.6 x 10^6 ohm-cm and 2.3 x 10^6 ohm-cm (shown in table 4.4 in terms of conductivity at 400 K). Apart from these, here are no other reports on V_2O_5-CaO-P_2O_5 glasses.

In this chapter, a systematic study of electrical and other physical properties of V_2O_5-CaO-P_2O_5 glasses has been undertaken.

4.2. Preparation

Glass samples of the system $xV_2O_5.40CaO.(60-x)P_2O_5$ with $10 \leq x \leq 30$ were prepared by melt quenching technique. Appropriate amounts of high purity V_2O_5, $CaCO_3$ and P_2O_5 were weighed and mixed by continuously kneading for about 20 min. The well-mixed oxide mixture was then transferred to an alumina crucible and melt at about 1100 °C in an electric furnace. The melt was held at this temperature for about 3 hours before being press quenched between two copper plates. Identical preparation conditions such as furnace temperature and quenching procedure were followed while preparing the entire series of glasses.

4.3. Characterisation

All the glass samples prepared were checked for amorphous nature by obtaining X-ray powder diffraction (XRD) patterns. A typical XRD pattern for a V_2O_5-CaO-P_2O_5 glass is shown in figure 4.1. The XRD pattern of the as quenched glass samples showed no sharp peaks declaring the amorphous nature of the samples. As explained in the previous chapter, the glassy nature of the samples was confirmed from the observation of the glass transition temperature (T_g). Differential scanning calorimeter (DSC) was used for determining the T_g. DSC curves were recorded for all the samples. The DSC curves of the as quenched samples showed a common feature of an endothermic base line shift corresponding to the glass transition temperature (figure 4.6) between 400 K and 500 K when heated at a constant heating rate of 10 °C.min^{-1}. The data analysis and interpretation for the DSC data will be discussed in the sub-chapter on DSC studies. Thermoelectric

power (TEP) measurements were performed on all V_2O_5-CaO-P_2O_5 glass samples in order to identify the majority charge carrier type. The TEP data would be presented and discussed in the following sub-chapter.

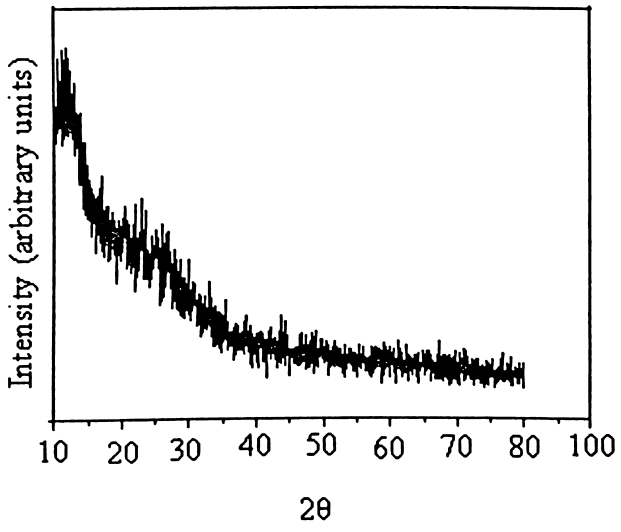

Figure 4.1 XRD pattern of a typical V_2O_5-CaO-P_2O_5 glasses.

4.4. Thermoelectric power and vanadium ion concentration

Thermoelectric power (TEP) measurements were performed on the $xV_2O_5.40CaO.(60-x)P_2O_5$ glasses with x = 10, 15, 20, 25, 30 mol % V_2O_5 using the experimental technique already discussed. The TEP data is shown in table 4.1. Q values obtained for $xV_2O_5.40CaO.(60-x)P_2O_5$ glasses from measurements showed that the compositions with x = 10 mol % V_2O_5 and x = 15 mol % V_2O_5 showed $Q > 0$, indicating that these two compositions are p-type semiconductors. The rest of the compositions, namely, x = 25, 30 mol % V_2O_5 showed $Q < 0$ and hence they are n-type semiconductors. $Q = 0$ for x = 20 mol % V_2O_5 indicating that the majority charge carrier reversal (MCCR) occurred at x = 20 mol % V_2O_5 in $xV_2O_5.40CaO.(60-x)P_2O_5$ glasses. These Q values agreed with the ones reported earlier [7, 162] wherever such a comparison was possible. Figure 4.2 shows the variation of Q with the V_2O_5 mol % in V_2O_5-CaO-P_2O_5 glasses. As already

discussed, Q is related to the high and low vanadium ion concentration ratio (V^{5+}/V^{4+}) {relation (1.32)}. The concentration of the vanadium ions was estimated for all the glasses by iodometry method using the titration procedure outlined in chapter 2. Table 4.1 lists the estimated vanadium ion ratio (V^{5+}/V^{4+}) for the $xV_2O_5.40CaO.(60\text{-}x)P_2O_5$ ($10 \leq x \leq 30$) glasses. Of these, x = 10 mol % V_2O_5 and x = 15 mol % V_2O_5 glass compositions showed $V^{5+}/V^{4+} < 1$. Since $Q > 0$ for these two glasses these are p-type semiconductors. On the other hand, x = 25 mol % V_2O_5 and x = 30 V_2O_5 mol % glasses, showed $V^{5+}/V^{4+} > 1$. Since $Q < 0$ for these glasses, they exhibit n-type conduction. For the x = 20 V_2O_5 mol % glass, $V^{5+}/V^{4+} = 1$ and the corresponding Seebeck coefficient was Q = 0, indicating that the MCCR phenomenon occurred at x = 20 mol % V_2O_5 composition in $xV_2O_5.40CaO.(60\text{-}x)P_2O_5$ ($10 \leq x \leq 30$) glasses. Apart from predicting the sign of Q, Q' (Q calculated from relation 1.32) showed a good agreement with the experimentally obtained Q values. This confirms the applicability of equation (1.32) to $xV_2O_5.40CaO.(60\text{-}x)P_2O_5$ ($10 \leq x \leq 30$) glasses. The relevant data are tabulated in table 4.1 for comparison purpose. The high Q values obtained for the p and n-type glasses shows that this glass system has promising device applications.

Table 4.1: Seebeck coefficient Q(measured), Q'(calculated), activation energy for thermal conduction ΔE_s and vanadium ion ratio of V_2O_5-CaO-P_2O_5 glasses (values given bracket are those reported by Kennedy et al [7])

Composition(mol %) V_2O_5 : CaO : P_2O_5	Q (μVK^{-1})	$\frac{V^{5+}}{V^{4+}}$	Q' (μVK^{-1})	ΔE_s (meV)
10 : 40 : 50	+112	0.36 (0.3)	+90	0.88
15 : 40 : 45	+40	0.70 (--)	+31	0.77
20: 40 : 40	0	1.0 (1.0)	0	----
25 : 40 : 35	-82	2.52 (---)	-80	0.70
30 : 40 : 30	-103	2.79 (2.9)	-88	0.61

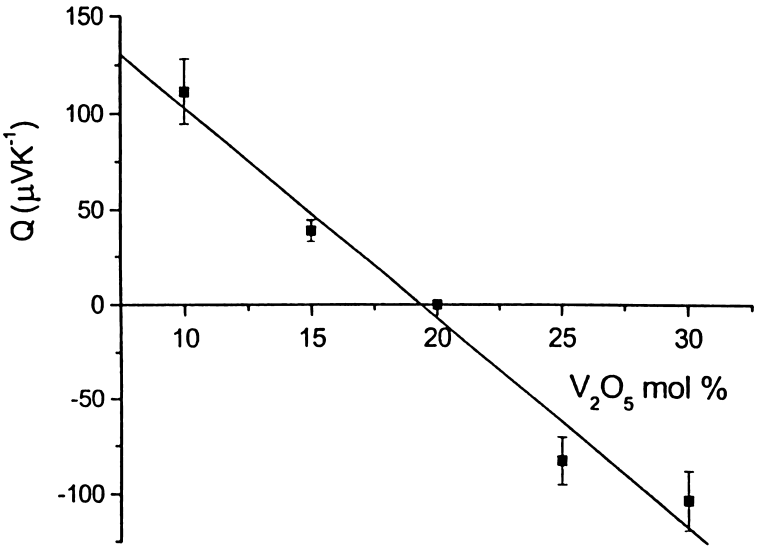

Figure 4.2: Variation of Q of $xV_2O_5.40CaO.(60-x)P_2O_5$ glasses (measured at 400K) with V_2O_5 mol%. The solid line is the least squares fit to the data.

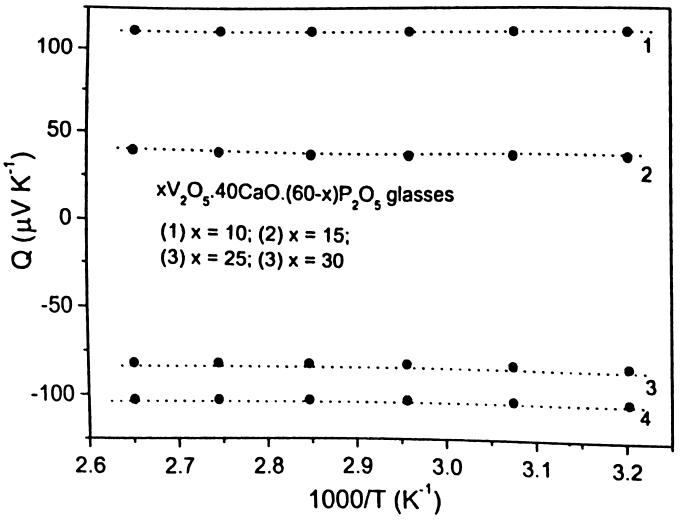

Figure 4.3: Q verses 1000/T for $xV_2O_5.40CaO.(60-x)P_2O_5$ ($10 \leq x \leq 30$) glasses. Dotted lines are the least squares fit to the data.

Q versus 1000/T plots for various compositions of $xV_2O_5.40CaO.(60-x)P_2O_5$ ($10 \leq x \leq 30$) glasses are shown in figure 4.3. The dotted lines are the least squares fit to the data. Figure 4.3 shows the weak dependence of Q on temperature. The variation of thermal activation energy ΔE_S (determined from the slope of figure 4.3) as a function of V_2O_5 mol % is shown in figure 4.4. The thermal activation energy ΔE_S decreases as V_2O_5 content increases in the glass. The same interpretation given for V_2O_5-SnO-TeO_2 glasses is applicable for these glasses as well. It is predicted that the thermal conductivity of the glasses increases as V_2O_5 content increases. ΔE_S data shows a gentle variation across the across the composition at which the MCCR is observed in V_2O_5-CaO-P_2O_5 glasses.

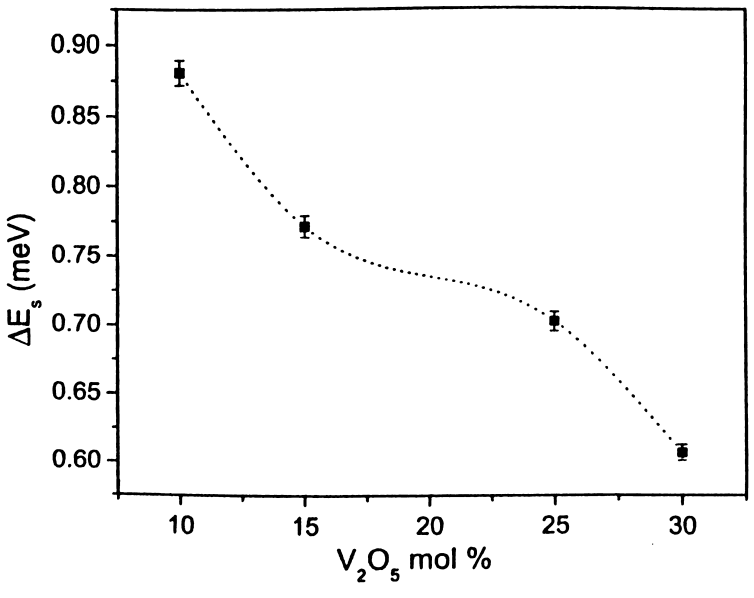

Figure 4.4: Thermal activation energy ΔE_S of $xV_2O_5.40CaO.(60-x)P_2O_5$ glasses.

4.5. other physical properties

4.5.1. Density

Density of $xV_2O_5.40CaO.(60- x)P_2O_5$ glasses was measured utilizing the procedure explained in the previous two chapters. From the density data, the molar volume of the glasses was calculated using the relation (2.9) The gram molecular weight was calculated from the relation,

$$M = x\, M(V_2O_5) + 0.4\, M(CaO) + (0.6-x)\, M(P_2O_5) \qquad (4.1)$$

where x is the mole fractions of V_2O_5, and $M(V_2O_5)$, M(CaO) and $M(P_2O_5)$ are the molecular weights of the constituents. Density and molar volume data of the V_2O_5-CaO-P_2O_5 glasses are shown in table 4.2 (data reported earlier are given within parenthesis).

Table 4.2: Optical band gap, density, molar volume, and microhardness of $xV_2O_5.40CaO.(60-x)P_2O_5$ glasses.

Composition(mol. %) V_2O_5 : CaO : P_2O_5	E_{opt} (eV)	Density(ρ) (gm cm^{-3})	Mol.Vol. (cm^3/mol)	VHN (kg mm^{-2})
10 : 40 : 50	3.46	2.76 (2.799)	40.43	336
15: 40 : 45	3.33	2.84 (----)	39.99	325
20 : 40 : 40	3.23	2.91 (2.963)	39.72	320
25 : 40 : 35	3.12	2.98 (----)	39.45	312
30 : 40 :3 0	3.02	3.05 (3.052)	39.20	299

Figure 4.5 shows the composition dependence of the density and the molar volume of $xV_2O_5.40CaO.(60-x)P_2O_5$ glasses. The density of the glass increases and molar volume decreases as V_2O_5 mol % content increases. When V_2O_5 mol. % increased, V_2O_5 molecules progressively replace P_2O_5 molecules. Since the molecular weight of V_2O_5 (181.876) is more than the molecular weight of P_2O_5 (141.939), one would expect the overall density of the glass to increase. But, the molar volume decreases as V_2O_5 mol %

content increases resulting in a shrinkage of the glassy network. Hence on the whole, the density of the glass increases as V_2O_5 mol % content is increased.

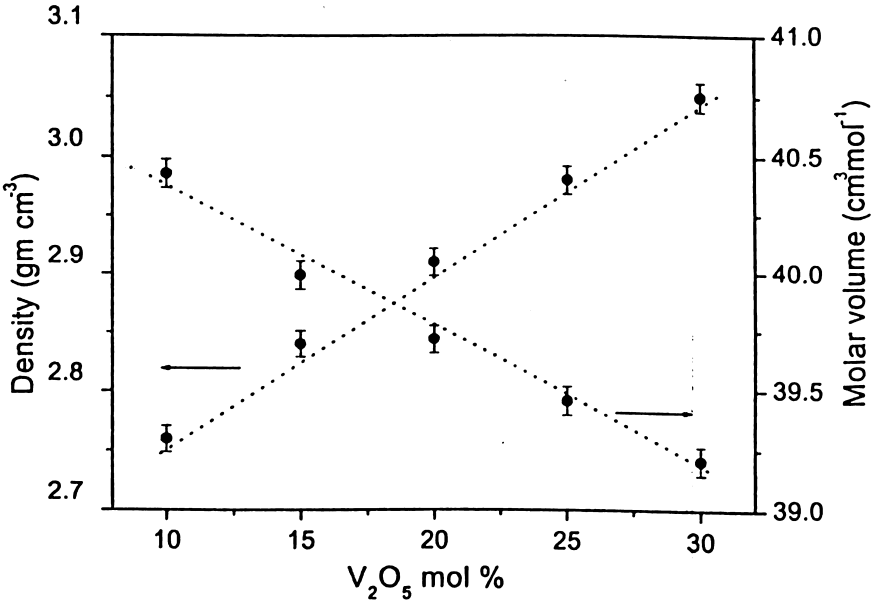

Figure 4.5: Composition dependence of the density and the molar volume of $xV_2O_5.40CaO.(60- x)P_2O_5$ ($10 \leq x \leq 30$) glasses.

4.5.2. Optical band gap

The optical band gap of $xV_2O_5.40CaO.(60- x)P_2O_5$ glasses has been measured using the procedure already discussed. The absorption data of the glasses was recorded in the wavelength range of 190 nm to 800 nm. The optical band gap E_{opt} was estimated from the $(\beta h\nu)^{1/2}$ versus $(h\nu)$ plots. Table 4.2 lists the optical band gap E_{opt} for $xV_2O_5.40CaO.(60-x)P_2O_5$ (x = 10, 15, 20, 25, 30) glasses. The variation of the optical band gap with the V_2O_5 mol % for V_2O_5-CaO-P_2O_5 glasses is shown in figure 4.6. The optical band gap decreases as the V_2O_5 mol % is increased in these glasses. Muncaster et al [163, 164] have studied the electron paramagnetic resonance (EPR) spectra of V_2O_5-P_2O_5 glasses and reported a decrease in the covalency of V-O bond with an increase in V_2O_5 mol %.

The decrease in the covalency is associated with an increase in the number of non-bridging oxygens [18] in the glass. The presence of more non-bridging oxygens reduces the average chemical bond strength of the glass. As a result, the absorption edge shifts towards the higher wavelength region. This explains the decrease in the optical band gap of $xV_2O_5.40CaO.(60- x)P_2O_5$ glasses with the increase in V_2O_5 mol %.

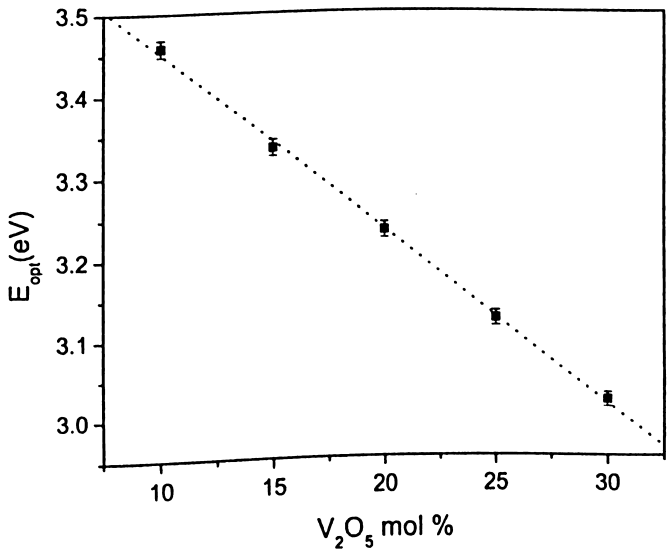

Figure 4.6: Composition dependence of optical band gap of V_2O_5-CaO-P_2O_5 glasses.

4.5.3. Microhardness

Measurements of microhardness were performed on V_2O_5-CaO-P_2O_5 glasses with a 100 g load (and 15 seconds loading time). The VHN values are shown in table 4.2. Figure 4.7 shows the variation of hardness value with V_2O_5 mol % content in $xV_2O_5.40CaO.(60-x)P_2O_5$ glasses with x = 10, 15, 20, 25, 30 glasses. It has already been pointed out that the number of non-bridging oxygens in these glass is expected to increase with an increase in V_2O_5 mol %. This reduces the elastic moduli which leads to a decrease in the microhardness of the glass {equation (1.42)}. Hardness of the glass can also be correlated

with the softening point of the glass [107]. Since T_g decreases with increasing V_2O_5 content (table 4.3), the microhardness is expected to decrease with increase in V_2O_5 content in this glass system.

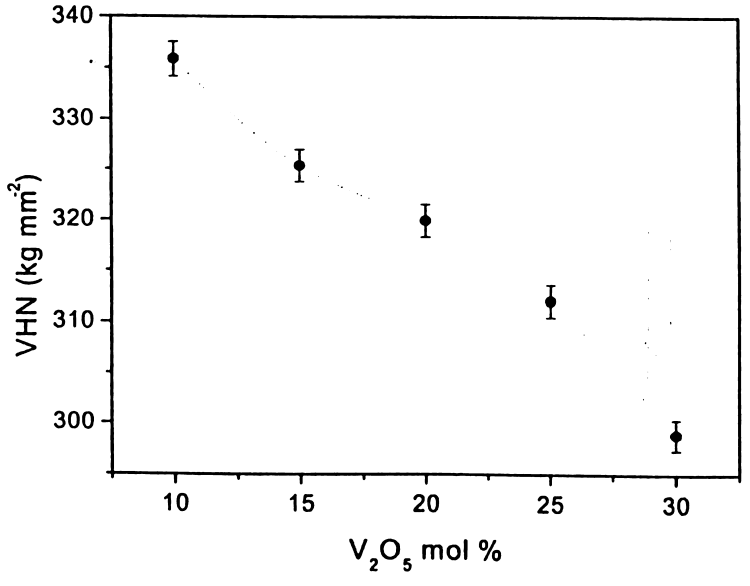

Figure 4.7: Composition dependence of VHN of $xV_2O_5.40CaO.(60- x)P_2O_5$ glasses.

4.6. DSC studies

DSC studies were performed on $xV_2O_5.40CaO.(60-x)P_2O_5$ glasses with x = 10, 15, 20, 25, 30. Figure 4.8 shows a typical set of DSC curves obtained for V_2O_5-CaO-P_2O_5 glass under a constant heating rate of 20 °C.min^{-1}. T_g varied between 429 K to 469 K for the glasses studied. The crystallization exotherms were broad and weak as shown by the thermograms. The T_g and ΔC_P (heat capacity jump at T_g) are shown in table 4.2 for a typical heating rate 10 °C/min. The molar volume of oxygen ion in $xV_2O_5.40CaO.(60-x)P_2O_5$ glasses was also calculated (table 4.2) using the empirical relation,

$$V_o^{\bullet} = \frac{[M(V_2O_5) - 16C_v]x + M(P_2O_5)y + M(CaO)z}{\rho[(5 - C_v)x + 5y + z]} \qquad (4.2)$$

where ρ is the density of the glass composition, $C_V = V^{4+} / V_{total}$, x, y, z and $M(V_2O_5)$, $M(P_2O_5)$, M(CaO) are the molar fraction and molecular weight of V_2O_5, P_2O_5 and CaO respectively. The calculated V_o^* values of the glasses are shown in table 4.2. V_o^* decreases from 12.02 cm^3mol^{-1} to 11.68 cm^3mol^{-1} as V_2O_5 mol. % is increased from 10 to 30 mol. %. The increase in T_g with an increase in the value of V_o^* (figure 4.9) indicates that the glass structure turns more loosely packed with an increase in P_2O_5 mol. % in V_2O_5-CaO-P_2O_5 glass system.

Table 4.3: Calorimetric C_V and V_o^* data of V_2O_5–CaO-P_2O_5 glasses.

Composition (mol. %) V_2O_5 : CaO : P_2O_5	T_g (K)	ΔCp ($Jg^{-1}deg^{-1}$)	E_T (KJ/mol)	E_K (KJ/mol)	C_V	V_o^* ($cm^3.mol^{-1}$)
10 : 40 : 50	467	0.85	153	145	0.74	12.02
15: 40 : 45	451	0.06	134	126	0.58	11.92
20 : 40 : 40	447	0.03	128	121	0.49	11.86
25 : 40 : 35	437	0.04	111	104	0.28	11.74
30 : 40 :3 0	429	0.26	105	97	0.26	11.68

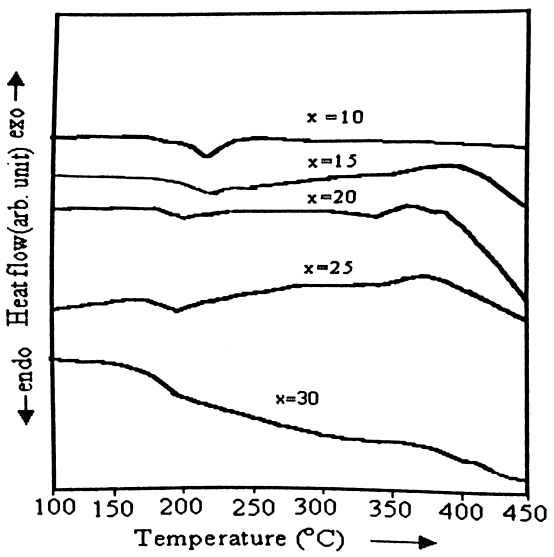

Figure 4.8: DSC curves of $xV_2O_5.40CaO.(60-x)P_2O_5$ glasses recorded at φ= 20 °C.min^{-1}.

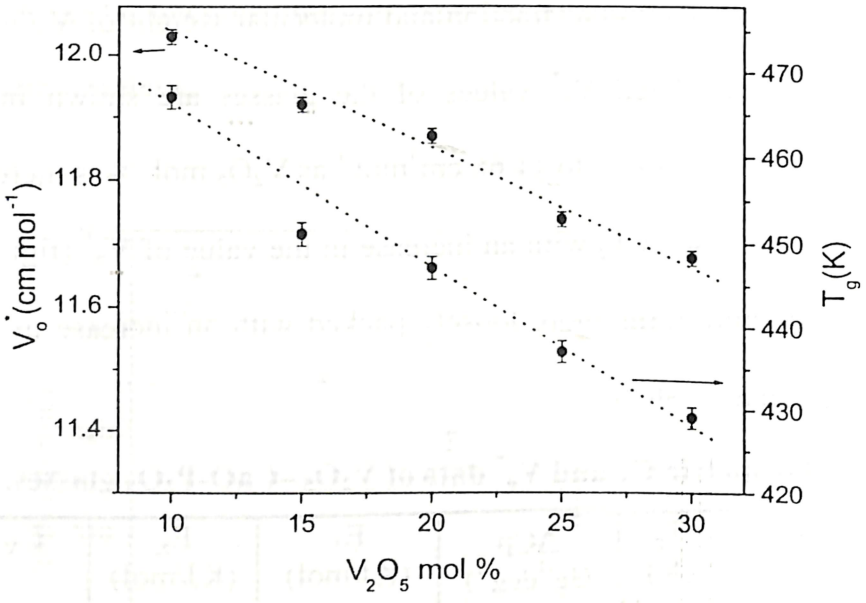

Figure 4.9: Variation of the molar volume of oxygen ion and glass transition temperature of $xV_2O_5.40CaO.(60- x)P_2O_5$ glasses as a function of V_2O_5 mol %.

Kissinger's and Thakor's methods were used for estimating the activation energy for glass transition (since T_g is the only prominent reaction temperature exhibited by all these glasses). T_g for different heating rates (φ) were used to obtain $\ln(\varphi/T_g^2)$ versus $1000/T_g$ (Kissinger's) plots (equation 2.1) and $\ln(\varphi)$ versus $1000/T_g$ (Thakor's) plots (equation 2.3). The Kissinger's plots obtained for these glasses are shown in figure 4.10 and the Thakor's plots in figure 4.11. E_K and E_T data are tabulated in table 4.3. It can be seen that $E_T > E_K$ for all the glasses as expected. The composition dependence of the activation energy for glass transition is shown in figure 4.12. Figure 4.12 shows that the activation energies E_K and E_T decrease linearly with increasing V_2O_5 mol %, indicating that the glass-supercooled liquid transition is less hindered in glasses with higher V_2O_5 content.

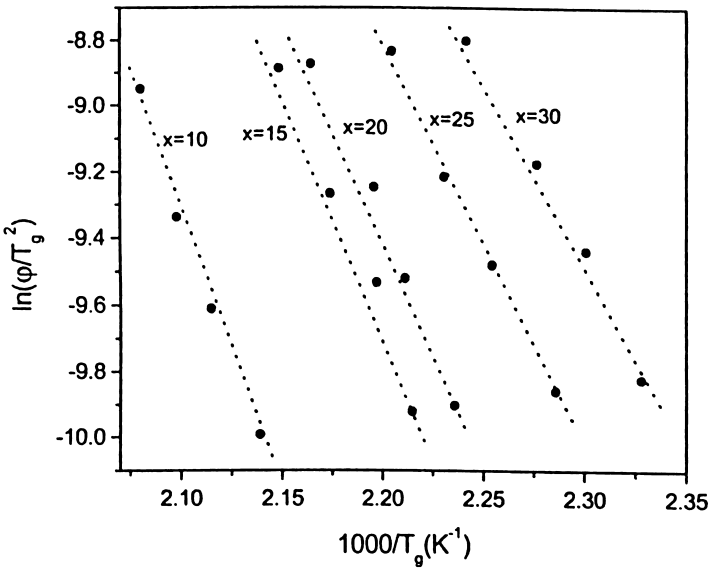

Figure 4.10: Kissinger's plots for $xV_2O_5.40CaO.(60- x)P_2O_5$ glasses.

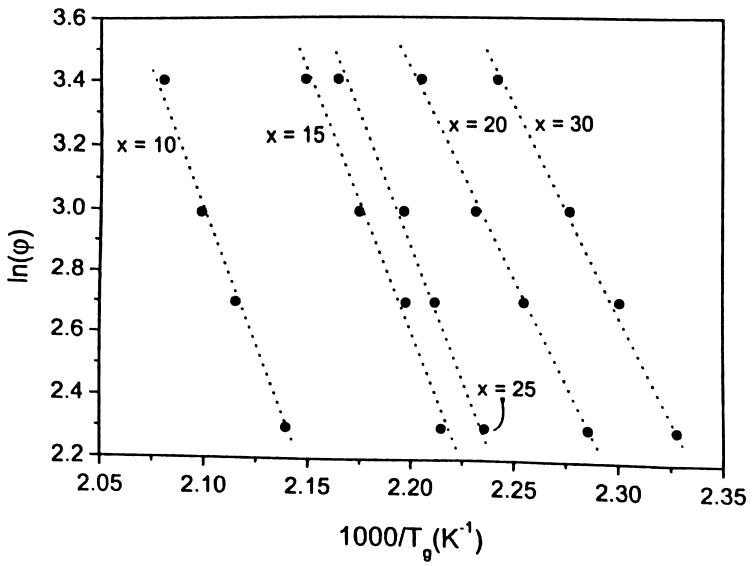

Figure 4.11: Thakor's plots for $xV_2O_5.40CaO.(60- x)P_2O_5$ glasses.

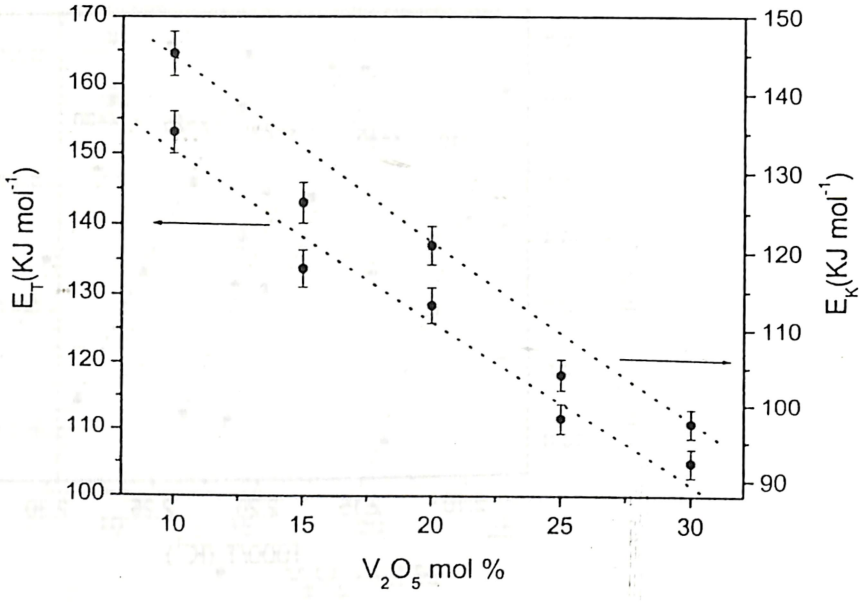

Figure 4.12: Activation energy of glass transition based on Kissinger's and Thakor's method for various compositions of V_2O_5-CaO-P_2O_5 glasses (Dotted lines shown merely connect adjacent data points).

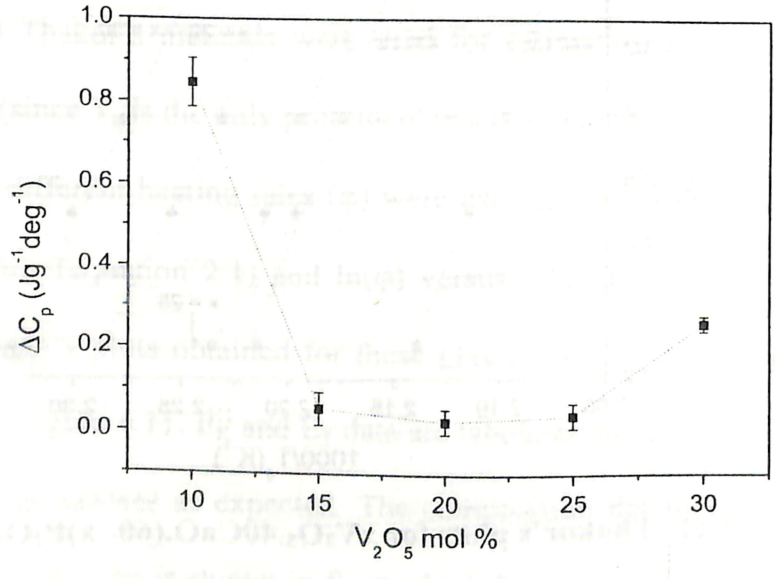

Figure 4.13: Excess heat capacity at glass transition of V_2O_5-CaO-P_2O_5 glasses. Dotted line shown merely connects adjacent data points.

The heat capacity jump (ΔC_P) at T_g for V_2O_5-CaO-P_2O_5 glasses (shown in figure 4.13) shows an interesting composition dependence All the glasses showed a small heat capacity jump, which is typical of "strong" glasses [21]. It has been pointed out by Tatsumisago et al [165] that such "smearing out of heat capacity jump" (which gives an impression that crystallization has occurred), has been observed in Ge-As-Se glasses. Our investigations showed that these glasses have a general inhibition to crystallization and hence this small ΔC_P should be inferred as a signature of a strong glass. One can still see from table 4.3 that the glass with x = 20 mol % V_2O_5 shows the lowest ΔC_P value indicating that the fragility is minimum for the glass with x = 20 mol % V_2O_5.

4.7. d.c. electrical conductivity

The d.c. electrical resistivity data of $xV_2O_5.40CaO.(60- x)P_2O_5$ glasses was collected from 150 K to 480 K. The plot of $\ln(\sigma T)$ versus T^{-1} for all the glasses of this system covering a temperature range of 150 K to 480 K is shown in figure 4.14. Figure 4.14 shows that the plots deviate from linearity as the temperature is lowered, showing that the conduction mechanism in V_2O_5-CaO-P_2O_5 glasses deviates from the SPH mechanism. Conduction mechanism in high and low temperature regime will be discussed separately in the light of the Mott-Austin model for V_2O_5-CaO-P_2O_5 glasses.

Conduction in the high temperature (SPH) region

Mott-Austin proposed the variation of conductivity with temperature for small polaron hopping (SPH) mechanism in the high temperature region as

$$\sigma T = \sigma_0 e^{-\frac{W}{k_B T}} \qquad (4.3)$$

where, W is the activation energy for conduction, T is the absolute temperature and k_B is the Boltzmann constant. The density of transition metal ions (N) in V_2O_5-CaO-P_2O_5 glasses increases and distance between the metal ions (R) decreases as V_2O_5 mol % content is increased.

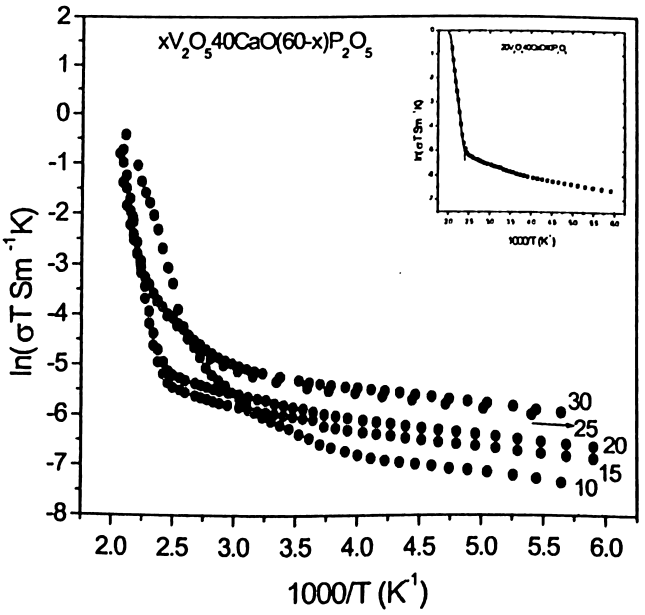

Figure 4.14: ln(σT) versus 1000/T plots for $xV_2O_5.40CaO.(60- x)P_2O_5$ (10x30) glasses. Inset shows a typical fit of the data to relation (4.3) (Only one out of ten data points has been plotted in order to improve the clarity of the figure).

Table 4.4: Density of metal ion sites N, average ion spacing R, conductivity σ (at 400K), polaron bandwidth j, the parameter Φ.

Composition (mol. %) V_2O_5 : CaO : P_2O_5	N ($x10^{27}m^{-3}$)	R ($x10^{-10}m$)	σ (at 400K) ($x10^{-5}\Omega^{-1}m^{-1}$)	j (eV) (10^{-5})	Φ (eV)
10 : 40 : 50	3.0	6.9	4.3	34.2	0.03
15: 40 : 45	4.5	6.0	4.4	25.3	0.03
20 : 40 : 40	6.1	5.5	4.5	6.0	0.03
25 : 40 : 35	7.6	5.1	5.5	2.1	0.03
30 : 40 :3 0	9.2	4.8	6.0	1.8	0.03

The parameter W was calculated from the slope of the least squares fit to ln(σT) versus 1000/T plots (table 4.4). As discussed in the first chapter, SPH conduction mechanism can be either adiabatic SPH mechanism or non-adiabatic SPH mechanism, based on the value of polaron band width (j). The calculated values of j and Φ are shown in table 4.4. For V_2O_5-CaO-P_2O_5 glasses, j value ranged from 3.4 x 10^{-4} eV to 1.8 x 10^{-4} eV and Φ value was approximately 0.03 eV. So for all the glasses, j < Φ. Hence, the conduction is attributed to non-adiabatic small polaron hopping.

Using j value, the non-adiabatic mobility for $xV_2O_5.40CaO.(60- x)P_2O_5$ glasses was calculated (table 4.5) using the relation (1.18). The non-adiabatic mobility ranged between 2.7 x 10^{-12} m^2V^{-1} sec^{-1} and 2.6 x 10^{-13} $m^2V^{-1}sec^{-1}$ for these glasses. Carrier concentration N_c was calculated using non-adiabatic mobility. Figure 4.15 shows the relation between the average vanadium ion distance R and activation energy for conduction W for the V_2O_5-CaO-P_2O_5 glasses. An increase in W with an increase in R (as shown in figure 4.15) is the general behavior expected as per theoretical predictions [151, 152].

Table 4.5: Activation energy for conduction W, non-adiabatic mobility μ, charge carrier concentration N_C for $xV_2O_5.40CaO.(60- x)P_2O_5$ glasses showing non-adiabatic SPH conduction.

Composition (mol. %) V_2O_5 : CaO : P_2O_5	W (eV)	R (x10^{-10} m)	μ (x10^{-13} $m^2V^{-1}sec^{-1}$)	N_C (x10^{26} m^{-3})
10 : 40 : 50	0.31	6.9	27.4	1.0
15: 40 : 45	0.30	6.0	16.0	1.7
20 : 40 : 40	0.23	5.5	5.7	4.9
25 : 40 : 35	0.18	5.1	3.1	11.1
30 : 40 :3 0	0.17	4.8	2.6	14.5

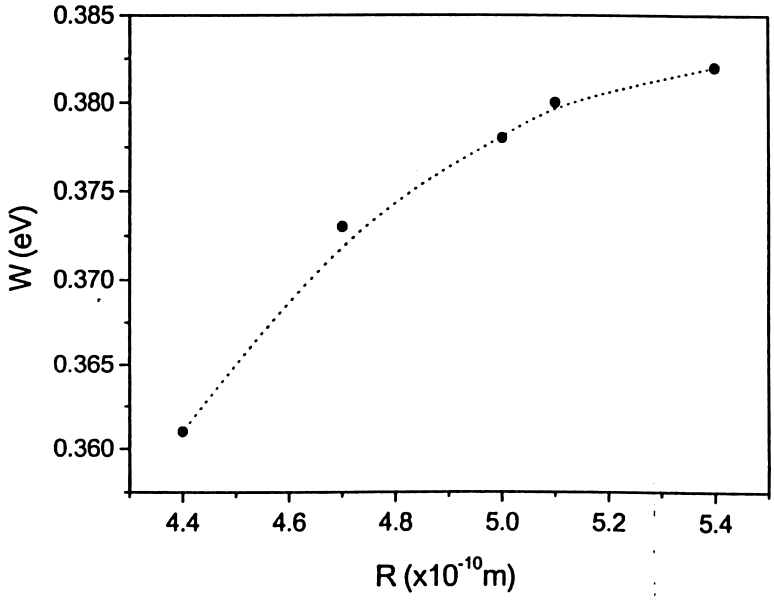

Figure 4.15: Effect of mean vanadium ion spacing R on activation energy W for conduction at 473 K of V_2O_5-CaO-P_2O_5 glasses exhibiting non-adiabatic SPH.

Conductivity in the low temperature region

Mott-Austin model proposed that variable range hopping (VRH) mechanism dominates at low temperatures. A linear plot of $\ln(\sigma T^{1/2})$ versus $T^{-1/4}$ signifies the occurrence of VRH conduction {equation(1.20)}. Figure 4.16 shows the $\ln(\sigma T^{1/2})$ versus $T^{-1/4}$ plots for $xV_2O_5.40CaO.(60- x)P_2O_5$ glasses with x = 10, 15, 20, 25 and 30 mol % V_2O_5 respectively. The linearity observed in the plots in low temperature region confirms that VRH conduction mechanism is dominant at these temperatures. Hence, the conductivity data in low temperature region was analyzed in the light of the Mott-Austin VRH mechanism. The slope change in the plots shown in figure 4.16 has been interpreted [73, 78] to be the signature of to the conduction change from SPH to VRH. All V_2O_5-CaO-P_2O_5 glasses exhibited a cross-over from SPH to VRH conduction mechanism when the temperature was lowered.

The parameters α and $N(E_F)$ were calculated from the slope and intercept values obtained from the linear fit to the low temperature ($T < T_R$) data using relations (1.21) and (1.22). From the calculated values of α and $N(E_F)$, the hopping distance R_{VRH} in VRH regime and hopping energy W_o were obtained using the relations (1.23) and (1.24),

As explained in chapter 1, at low temperatures the polaron binding energy becomes lower than the W_d, and hence it is assumed that Based on the assumption that $W_o = W_d$, the disorder energy W_d was calculated using equation (1.24). Mott parameters $N(E_F)$ and R_{VRH} for the glasses are shown in the table 4.5.

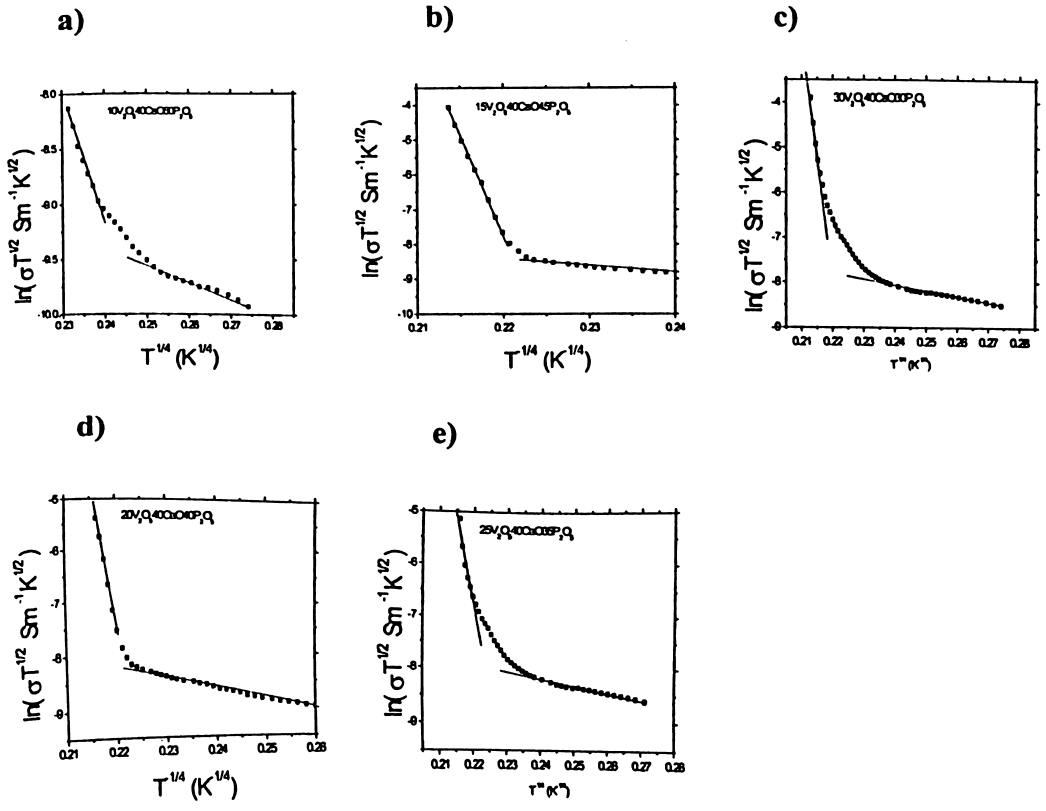

Figure 4.16: $\ln(\sigma T^{1/2})$ versus $T^{-1/4}$ plots for $xV_2O_5.40CaO.(60\text{-}x)P_2O_5$ glasses (Several data points have been skipped in order to improve clarity of the plots. Solid lines are least squares fit to $T > T_R$ and $T < T_R$ data).

Table 4.6: Density of states at Fermi energy $N(E_F)$, variable range hopping distance R_{VRH} and disorder energy W_d.

Composition (mol %) V_2O_5 : CaO : P_2O_5	$N(E_F)$ ($x10^{26}$ $m^{-3}eV^{-1}$)	R_{VRH} ($x10^{-9}$m)	W_d (eV)	αR_{VRH}
10 : 40 : 50	1.7	3.84	0.03	1.86
15: 40 : 45	2.1	3.76	0.03	1.64
20 : 40 : 40	2.4	3.66	0.03	1.51
25 : 40 : 35	3.5	3.46	0.02	1.22
30 : 40 :3 0	3.9	3.41	0.02	1.16

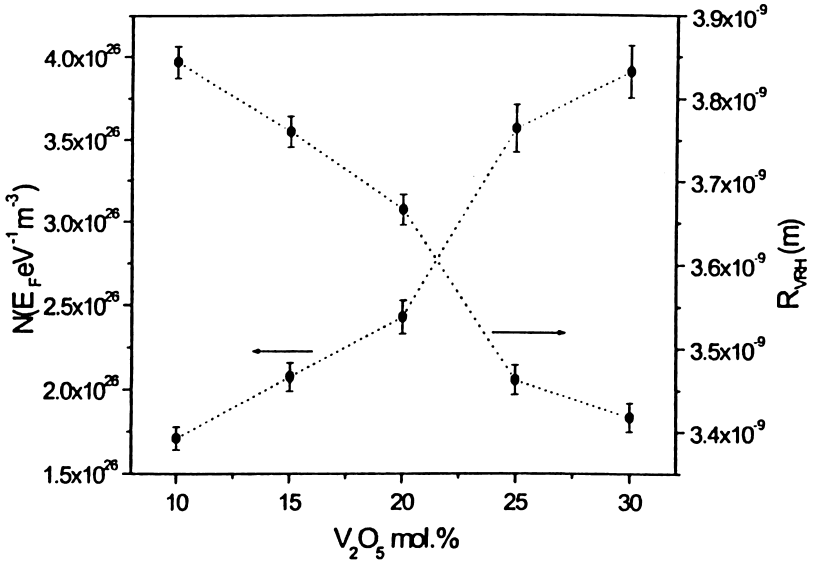

Figure 4.17: Variation of density of states at Fermi energy $N(E_F)$ and the variable range hopping distance (R_{VRH}) as a function of V_2O_5 mol %.

Both $N(E_F)$ and R_{VRH} vary as a function of V_2O_5 mol. %. Figure 4.17 shows the variation of $N(E_F)$ and R_{VRH} with change in V_2O_5 mol %. While $N(E_F)$ increases with an increase in V_2O_5 mol %, R_{VRH} decreases as V_2O_5 mol % increases. The increase in $N(E_F)$ and decrease in R_{VRH} follow the pattern expected from theoretical predictions [1, 67] and agrees with reported behavior [72] of V_2O_5 based glasses. The requirements $\alpha R_{VRH} > 1$ and $W_d \geq k_BT$ (eg. $W_d \geq 0.019$ eV at 230 K) for occurrence of VRH mechanism are also satisfied. Evaluation of present data at 230 K gave αR_{VRH} values ranging between 1.15

and 1.86 and W_d values 0.02 eV to 0.03 eV. Hence the conduction mechanism in V_2O_5-CaO-P_2O_5 glasses in the low temperature region is attributable to VRH. From figure 4.17, it is obvious that there is a subtle variation in $N(E_F)$ and R_{VRH} near the composition (x = 20 mol %) at which the MCCR occurs. These observations suggest that the low temperature electrical conduction mechanism is sensitive to the majority charge carrier reversal phenomenon.

4.8. Summary

I. The thermo electric power measurements on the various compositions of glasses of the V_2O_5-CaO-P_2O_5 glass system show the following features:

(i) Glasses with x = 10 and 15 mol. % V_2O_5 showed p-type semiconductor and glasses with x = 25 and 30 mol % V_2O_5 showed n-type semiconductor behaviour. MCCR occurred at the glass with x = 20 mol. % V_2O_5.

(ii) All glasses exhibited weak Q dependence on temperature.

(iii) The activation energy for thermoelectric power showed a slope change near x = 20.

II. Density, microhardness and band gap measurements showed the following features:

(i) Density increased and molar volume decreased as V_2O_5 content was increased.

(ii) Vicker's microhardness decreases as V_2O_5 content increased.

(iii) The band gap E_{opt} decreased as the V_2O_5 mol % was increased.

III. DSC studies gave the following results:

(i) T_g increased with an increase in P_2O_5 mol. % (decrease in V_2O_5 mol. %) indicating the characteristics of a loosely packed structure.

(ii) The composition dependence of the activation energy of glass transition showed the glass-supercooled transition is less hindered for higher V_2O_5 mol% .

(iii)The excess heat capacity ΔC_p at T_g of all the glasses was small. Of these, the glass with 20 mol % V_2O_5 showed the minimum ΔC_p value.

IV. d.c. electrical conductivity measurements gave the following results:

(i) The conduction mechanism in the high temperature region is attributed to non adiabatic SPH in $xV_2O_5.40CaO.(60-x)P_2O_5$ ($10 \leq x \leq 30$) glasses. All the glasses showed a changeover from SPH to VRH at a characteristic temperature when cooled below room temperature.

(ii) The Mott paramters $N(E_F)$ increased and R_{VRH} decreased as V_2O_5 content was increased. $N(E_F)$ and R_{VRH} showed subtle changes in their values to the composition with x = 20 mol % V_2O_5 at which the majority charge carrier reversal occurs in $xV_2O_5.40CaO.(60-x)P_2O_5$ glasses.

Chapter 5

Investigations on V_2O_5-CaO-B_2O_3 glasses

5.1. Introduction

In this chapter the possibility of obtaining glasses with positive Seebeck coefficient in vanadium borate based glasses would be explored. V_2O_5-B_2O_3 glasses are known to be amorphous semiconductors [9]. Since glass formation is difficult in the binary V_2O_5-B_2O_3 glass system, a third component (eg., CaO) is added to improve the glass formation [7]. The Seebeck coefficient Q is negative and the vanadium ion ratio, $V^{5+}/V^{4+} > 1$, for V_2O_5-CaO-B_2O_3 glasses. It is evident from the results of chapter 3 and 4 that glasses with $V^{5+}/V^{4+} < 1$ would certainly be p-type semiconductors. It has already been commented that preparing vanadate glasses under reducing conditions may help in obtaining p-type glasses. Kennedy et al [7] showed that it is possible to obtain p-type glasses in V_2O_5-CaO-B_2O_3 system if 0.2% abietic acid ($C_{20}H_{30}O_2$) is added. They demonstrated that addition of small amounts of abietic acid can reduce the vanadium ion ratio V^{5+}/V^{4+} to less than unity in this glass system. This study provided a means of obtaining p-type semiconductors in the otherwise n-type glass system. Kennedy et al explored the glass forming region (GFR) for V_2O_5-CaO-B_2O_3 glass (shown in figure 5.1). They studied the electrical resistivity of these glasses between 25 °C and 400 °C and its relation with V^{5+}/V^{4+} ratio [7]. They proposed the empirical relation (1.32) between V^{5+}/V^{4+} ratio and the Seebeck coefficient of these glasses. They concluded that the Seebeck coefficient of these glasses is dependent only on carrier and site concentrations. In literature, there are no reports of any systematic study on V_2O_5-CaO-B_2O_3 glasses. The xV_2O_5.40CaO.(60-x)B_2O_3 ($10 \leq x \leq 30$) series of glasses was chosen for the current study.

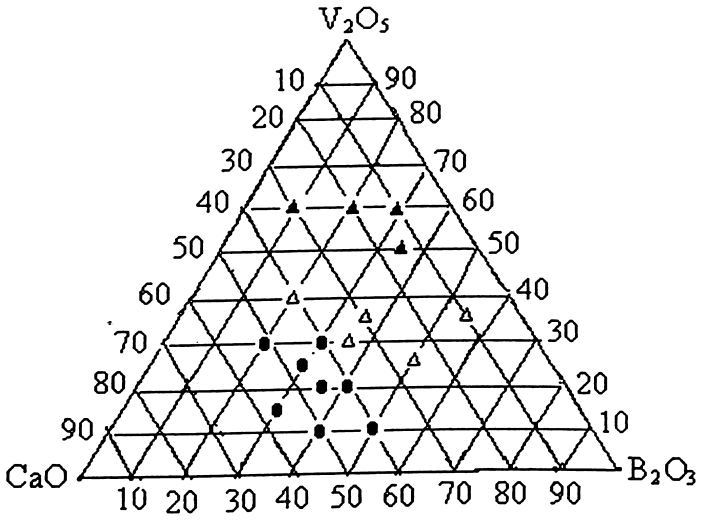

Figure 5.1: Glass forming regions in the V_2O_5-CaO-B_2O_3 system.
Δ Crystalline, ▲ Glass and crystal, ● Glass

5.2. Preparation

Appropriate amounts of high purity V_2O_5, CaO and B_2O_3 were weighed and mixed by continuously kneading for about 20 min. The well-mixed oxide mixture was then transferred to an alumina crucible and melted at about 1100 °C in an electric furnace. The melt was held at this temperature for about 3 hours and then press quenched between two copper plates. Identical preparation conditions such as furnace temperature and quenching procedure were followed while preparing the entire series of glasses. A few glass compositions were prepared without abietic acid in order to verify the effect of abietic acid on the vanadium ion ratio. Glasses prepared without abietic acid showed n-type semiconductor behaviour. Since the primary interest of this thesis work was to study glasses exhibiting MCCR, only V_2O_5-CaO-B_2O_3 glasses with 0.2 % abietic acid are discussed in this chapter.

5.3. Characterisation

X-ray diffraction technique was employed to verify the amorphous nature of the as-quenched glass samples. Figure 5.2 shows a typical XRD pattern for a V_2O_5-CaO-B_2O_3 glass. DSC curves were recorded for all the samples to determine the characteristic glass transition temperature T_g. The DSC curves of all the glasses showed an endothermic base line shift corresponding to the glass transition temperature. The T_g of V_2O_5-CaO-B_2O_3 glasses studied was between 500 K and 600 K when heated at a constant heating rate of 10 °C.min^{-1}. The glasses belonging to this system showed weak glass transition with small enthalpies. The data analysis and interpretation of the DSC data will be discussed in the sub-chapter on DSC studies. The majority charge carrier type in each glass composition was identified using thermoelectric power (TEP) measurements, details of which are discussed in the following sub-chapter.

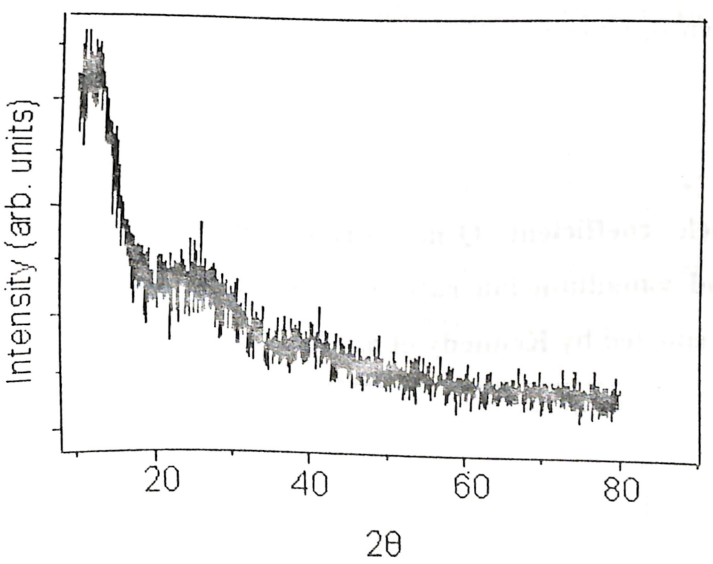

Figure 5.2: XRD pattern for one glass of V_2O_5-CaO-B_2O_3 glasses.

5.4. Thermoelectric power and vanadium ion concentration

The thermoelectric power (TEP) of $xV_2O_5.40CaO.(60\text{-}x)\ B_2O_3$ (x = 10, 15, 20, 25, 30) glasses was measured using the technique already discussed. The TEP data is shown in table 5.1. Q values obtained for $xV_2O_5.40CaO.(60\text{-}x).B_2O_3$ glasses from measurements showed that glass compositions with x = 10 mol % V_2O_5 and x = 15 mol % V_2O_5 have positive Q values, indicating that these two compositions are p-type semiconductors. Glasses with x = 25 and 30 mol % V_2O_5 showed negative Q values, and hence they are n-type semiconductors. For the x = 20 mol % V_2O_5 glass, Q = 0, which showed that the majority charge carrier reversal (MCCR) occurred at this composition in $xV_2O_5.40CaO.(60\text{-}x)B_2O_3$ glasses [7, 162]. Figure 5.3 shows the composition dependence of Q value of various V_2O_5-CaO-B_2O_3 glasses. Vanadium ion ratio V^{5+}/V^{4+} for each glass composition is shown in table 5.1. The values given in brackets are those reported by Kennedy et al [7].

Table 5.1: Seebeck coefficient Q(measured), activation energy for thermal conduction ΔE_s and vanadium ion ratio of V_2O_5-CaO-B_2O_3 glasses (values given bracket are those reported by Kennedy et al [7]).

Composition (mol %) V_2O_5 : CaO : B_2O_3	Q (μVK^{-1})	$\frac{V^{5+}}{V^{4+}}$	ΔE_s (meV)
10 : 40 : 50	+52	0. 55 (0.6)	0.78
15 : 40 : 45	+31	0.70 (--)	0.66
20: 40 : 40	0	1.0 (1.0)	----
25 : 40 : 35	-23	1.30 (---)	0.52
30 : 40 : 30	-36	1.52 (1.40)	0.47

The temperature dependence of Q of $xV_2O_5.40CaO.(60\text{-}x)B_2O_3$ glasses is depicted in figure 5.4. The dotted lines are least squares fit to the data. The weak temperature

dependence of Q which was also observed in V_2O_5-SnO-TeO_2 and V_2O_5-CaO-P_2O_5 glasses clearly shows that this is a typical feature exhibited these glasses. Variation of thermal activation energy ΔE_S with V_2O_5 mol % is shown in figure 5.5.

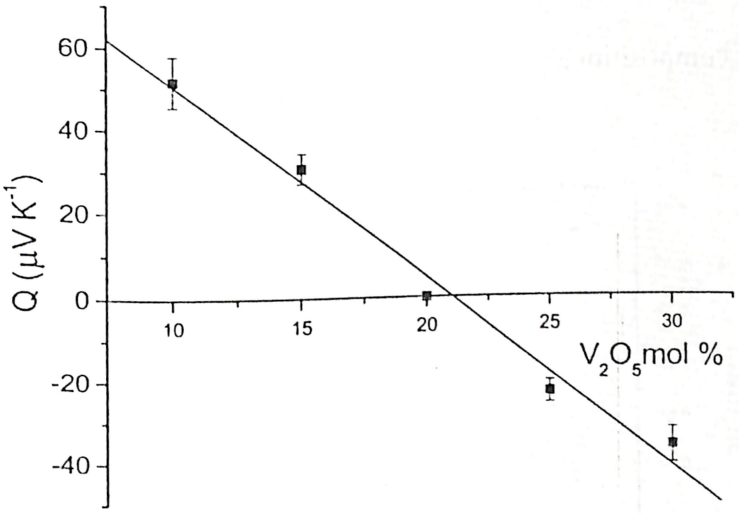

Figure 5.3: Variation of Q of $xV_2O_5.40CaO.(60-x)B_2O_3$ glasses (measured at 400K) with V_2O_5 mol%. The solid line is a least squares fit to the data.

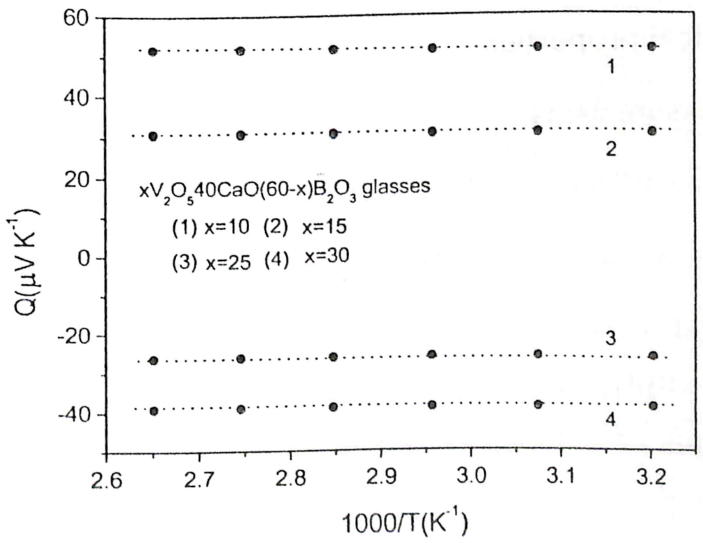

Figure 5.4: Q versus 1000/T for $xV_2O_5.40CaO.(60-x)B_2O_3$ ($10 \leq x \leq 30$) glasses. Dotted lines corresponds to the least squares fit to the data.

The thermal activation energy ΔE_S of these glasses decreased as V_2O_5 content was increased as shown by figure 5.5, suggesting that the thermal conductivity of the glasses increases with an increase in V_2O_5 content. A subtle slope change in ΔE_S is observed at 20 mol % V_2O_5 composition.

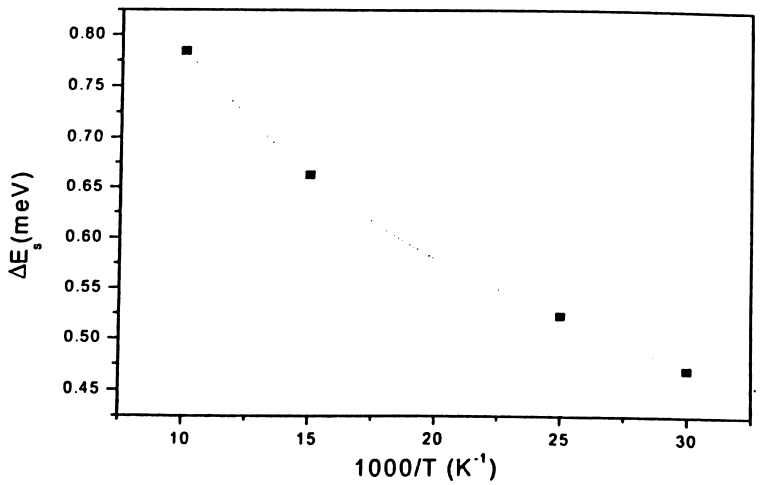

Figure 5.5: Thermal activation energy ΔE_S of $xV_2O_5.40CaO.(60\text{-}x)B_2O_3$

5.5. Other physical properties

5.5.1. Density measurements

The measured density values of $xV_2O_5.40CaO.(60\text{-}x)B_2O_3$ glasses are listed in table 5.2. Molar volume of the glasses was calculated using equation (2.8) and (2.9).

Table 5.2: Optical band gap, density, molar volume, and microhardness of $xV_2O_5.40CaO.(60\text{-}x)B_2O_3$ glasses (Data given within brackets are from ref. [7]).

Composition (mol %) $V_2O_5 : CaO : B_2O_3$	E_{opt} (eV)	Density(ρ) ($gm.cm^{-3}$)	Mol.vol. ($cm^3.mol^{-1}$)	VHN ($kg.mm^{-2}$)
10 : 40 : 50	3.62	2.79 (2.784)	27.07	367
15 : 40 : 45	3.57	2.86 (----)	28.35	329
20 : 40 : 40	3.53	2.93 (2.984)	29.54	309
25 : 40 : 35	3.48	2.9 (----)	31.82	282
30 : 40 :3 0	3.42	2.87 (2.929)	34.10	263

The gram molecular weight for the $xV_2O_5.40CaO.(60\text{-}x)B_2O_3$ glasses is given by the relation,

$$M = x\,M(V_2O_5) + 0.4\,M(CaO) + (0.6\text{-}x)\,M(B_2O_3) \qquad (5.1)$$

where x is the mole fractions of the V_2O_5, and $M(V_2O_5)$, $M(CaO)$ and $M(B_2O_3)$ are the molecular weights of the constituents. Density and molarvolume data of the V_2O_5-CaO-B_2O_3 glasses are shown in table 5.2 (values in brackets were taken from ref. [7].)

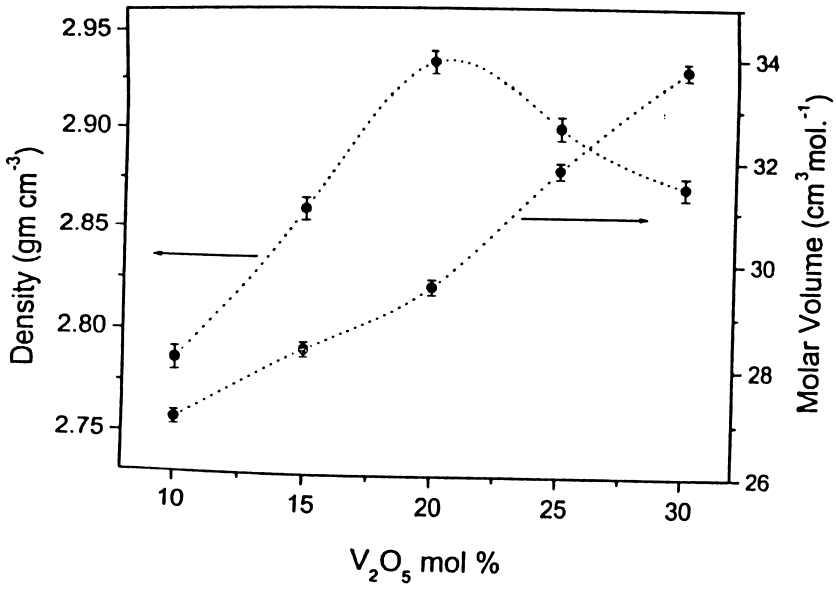

Figure 5.6: Composition dependence of the density and the molar volume of $xV_2O_5.40CaO.(60\text{-}x)B_2O_3$ ($10 \leq x \leq 30$) glasses.

Figure 5.6 shows the composition dependence of the density and molar volume of $xV_2O_5.40CaO.(60\text{-}x)B_2O_3$ glasses. The density of the glass increases as V_2O_5 content in the glass is increased and showed maximum value at the composition with x = 20 mol % V_2O_5. As V_2O_5 mol % increases, the molar volume increases and so one expects the density to decrease. But the molecular weight of the V_2O_5 molecule is approximately

twice the molecular weight of a B_2O_3 molecule. Hence, in spite of an increase in the molar volume when a V_2O_5 molecule replaces a B_2O_3 molecule, the overall mass of the glass increases on the whole. Consequently, the density increases with an increase in V_2O_5 mol %. The molar volume of the glass increases sharply [figure 5.6] after 20 mol % V_2O_5 which shows that glassy network expands faster after this composition. This results in a decrease in the density of the glass as illustrated by the weak maximum in the density at x = 20 mol % V_2O_5.

5.5.2. Optical band gap

The optical band gap of $xV_2O_5.40CaO.(60- x)B_2O_3$ glasses with x = 10, 15, 20, 25, 30 was obtained from $(\beta h\nu)^{1/2}$ versus $(h\nu)$ plots {equation (2.11)}. Table 5.2 lists the optical band gap E_{opt} of $xV_2O_5.40CaO.(60- x)B_2O_3$ glasses.

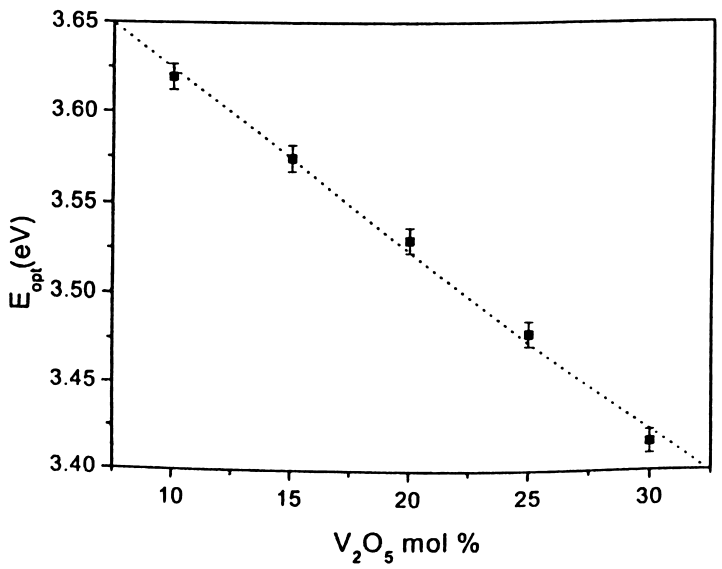

Figure 5.7: Variation in optical band gap of V_2O_5-CaO-B_2O_3 glasses.

The variation of the optical band gap with V_2O_5 mol % is shown in figure 5.7. Khasa et al [164] reported that the covalency of the V-O bond decreases with an increase in V_2O_5

content in vanadium borate glasses. Using the same arguments as given in the case of the V_2O_5-SnO-TeO_2 and V_2O_5-CaO-P_2O_5 glasses, it can be shown that the number of non-bridging oxygens increases in V_2O_5-CaO-B_2O_3 glasses as a function of V_2O_5 content. This reduces the average chemical bond strength of the glass. Hence, optical band gap decreases with increase in V_2O_5 content in the V_2O_5-CaO-B_2O_3 glass.

5.5.3. Microhardness measurements

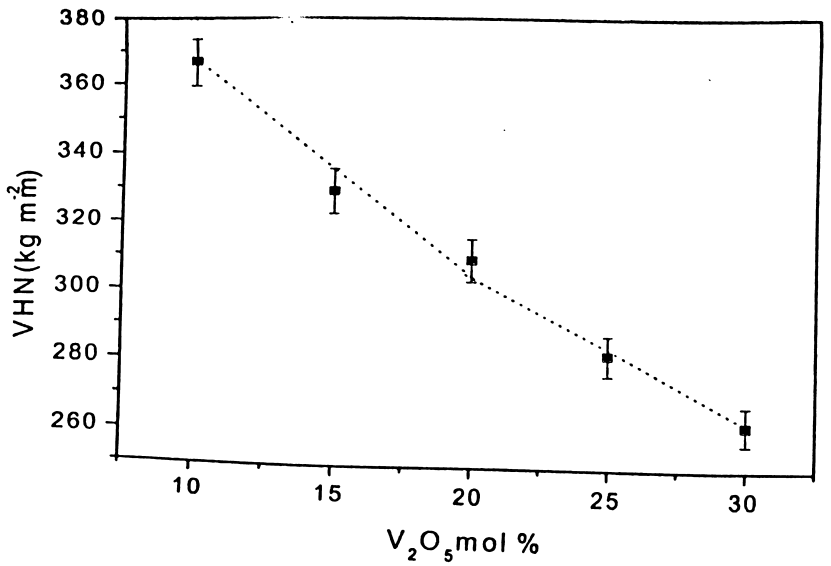

Figure 5.8: Composition dependence of VHN of V_2O_5-CaO-B_2O_3 glasses.

Microhardness measurements were performed on V_2O_5-CaO-B_2O_3 glasses. A 100 g load was applied for 15 seconds in order to obtain a measurable indentation. The microhardness values of the xV_2O_5.40CaO.(60- x)P_2O_5 glasses are given in table 5.2. Figure 5.8 shows the variation of VHN with V_2O_5 mol % content. As already discussed, a decrease in the elastic moduli of the glass can be expected with an increase in V_2O_5 mol % (as a consequence of an increase in the number of non bridging oxygens in the glass [164]). This accounts for the observed variation in microhardness of the V_2O_5-CaO-B_2O_3 glasses with V_2O_5 content plotted in figure 5.8. An interpretation of the microhardness

behaviour shown in figure 5.8 can also be made in terms of the variation of the softening temperature of these glasses as done in the case of the other two glass systems. T_g decreases with V_2O_5 mol % (table 5.3). Hence a decrease in the VHN is expected.

5.6. DSC studies

DSC curves corresponding to $xV_2O_5.40CaO.(60- x)B_2O_3$ (x = 10, 15, 20, 25, 30) glasses were recorded over a temperature range of 50 ^{0}C to 500 ^{0}C for different heating rates such as 10 °C.min^{-1}, 15 °C:min^{-1}, 20 °C.min^{-1} and 30 °C.min^{-1}. Figure 5.9 shows a typical DSC curve obtained for V_2O_5-CaO-B_2O_3 glass under a constant heating rate of 10 °C.min^{-1}. The glass transition temperature T_g for different heating rates was recorded for individual glass samples. The T_g and ΔC_P (specific heat jump at T_g) are shown in table 5.3 for a typical heating rate of 10 °Cmin^{-1}. The molar volume of oxygen ion for $xV_2O_5.40CaO.(60-x)B_2O_3$ glasses was calculated (shown in table 5.3) using the empirical relation,

$$V_o^* = \frac{[M(V_2O_5) - 16C_V]x + M(B_2O_3)y + M(CaO)z}{\rho[(5 - C_V)x + 3y + z]} \qquad (5.2)$$

where ρ is the density of the glass composition, $C_V = V^{4+} / V_{total}$, x, y, z and $M(V_2O_5)$, $M(B_2O_3)$, M(CaO) are the molar fraction and molecular weight of V_2O_5, B_2O_3 and CaO respectively. The calculated V_o^* from equation (5.2) of the glasses are shown in table 5.3. V_o^* varied from 11.43 cm^{3}mol^{-1} to 12.47 cm^{3}mol^{-1} as V_2O_5 mol % was varied from 10 to 30 V_2O_5 mol %. In V_2O_5-CaO-B_2O_3 glasses, the molar volume of oxygen ion V_o^* increased as T_g decreased. This behaviour is in contradiction to that displayed by the V_2O_5-SnO-TeO_2 and V_2O_5-CaO-P_2O_5 glass systems. Although the three glass systems showed the same trend in T_g with variation in V_2O_5 mol %, the composition dependence of V_o^* exhibited by the V_2O_5-CaO-B_2O_3 glasses is different from the ones shown by the

other two glass systems. This shows the limitation of the applicability of V_o^* and its relation to the structure of glass for the interpretation of the composition dependence of T_g. A careful look at the formula used to deduce V_o^* {relations (5.2), (4.2) and (3.1)} shows that the density term in the denominator of these relations is responsible for the disparate behaviour of V_o^* obtained for the case of the V_2O_5-CaO-B_2O_3 glasses. Activation energy for glass transition for the V_2O_5-CaO-B_2O_3 glasses was calculated using Kissinger's (2.1) and Thakor's (2.3) methods.

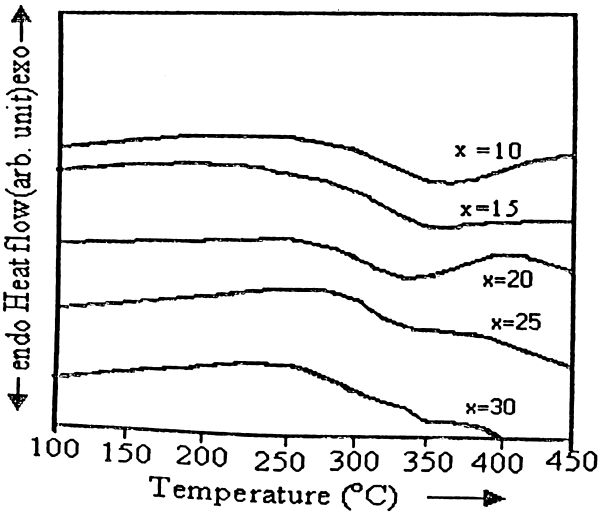

Figure 5.9: DSC curves for $xV_2O_5.40CaO.(60-x)B_2O_3$ glasses x=10, 15, 20, 25, 30 recorded at a constant heating rate of 10 °C.min^{-1}

The activation energies for glass transition E_K (Kissinger) and E_T (Thakor) were calculated from the slope of the least squares fit of the corresponding plots. E_K and E_T data are tabulated in table 5.3. It can be seen that $E_T > E_K$ for all the glasses as expected from theoretical predictions [118, 148]. The composition dependence of the activation energy for glass transition is shown in figure 5.13

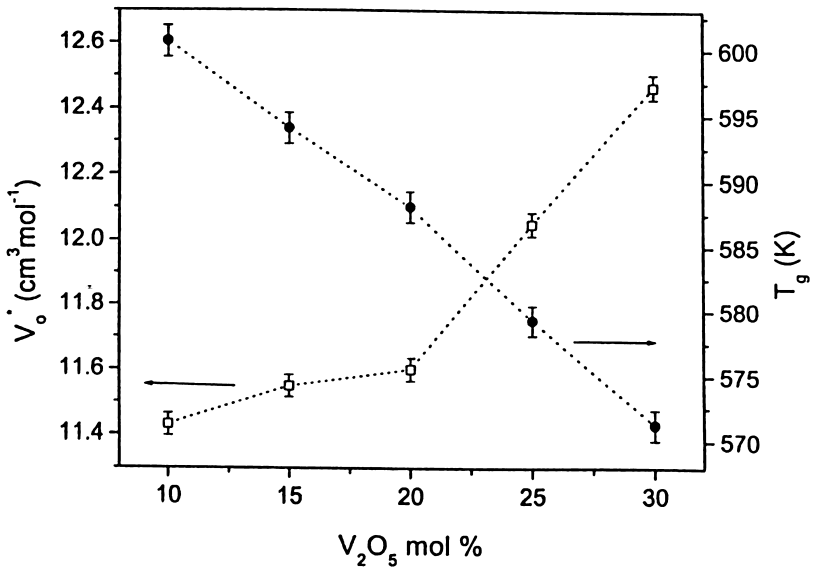

Figure 5.10: Variation of molar volume of oxygen ion and glass transition temperature of $xV_2O_5.40CaO.(60- x)B_2O_3$ glasses with V_2O_5 mol %.

Table 5.3: Glass transition temperature T_g at a constant heating rate of 10 °C.min^{-1}, excess heat capacity at glass transition ΔC_p, activation energy for glass transition E_T, E_K (based on Thakor's and Kissinger's model), reduced vanadium ion ratio $C_V = V^{4+}/(V^{4+}+V^{5+})$, molar volume of oxygen ion V_o^* of V_2O_5-CaO-B_2O_3 glasses.

Composition (mol %) V_2O_5 : CaO : B_2O_3	T_g (K)	ΔCp ($Jg^{-1}deg^{-1}$)	E_T (kJ/mol)	E_K (kJ/mol)	C_V	V_o^* ($cm^3.mol^{-1}$)
10 : 40 : 50	601	0.20	183	173	0.65	11.43
15: 40 : 45	594	0.05	162	152	0.59	11.55
20 : 40 : 40	588	0.04	157	147	0.5	11.60
25 : 40 : 35	579	0.08	150	140	0.43	12.05
30 : 40 :3 0	571	0.25	138	129	0.40	12.47

The activation energies E_K and E_T decrease linearly (figure 5.13) with increased in V_2O_5 mol %. Since a decrease in the activation energy indicates that the reaction is more favoured, it can be inferred that the glass-supercooled liquid transition is less hindered in glasses with higher V_2O_5 content.

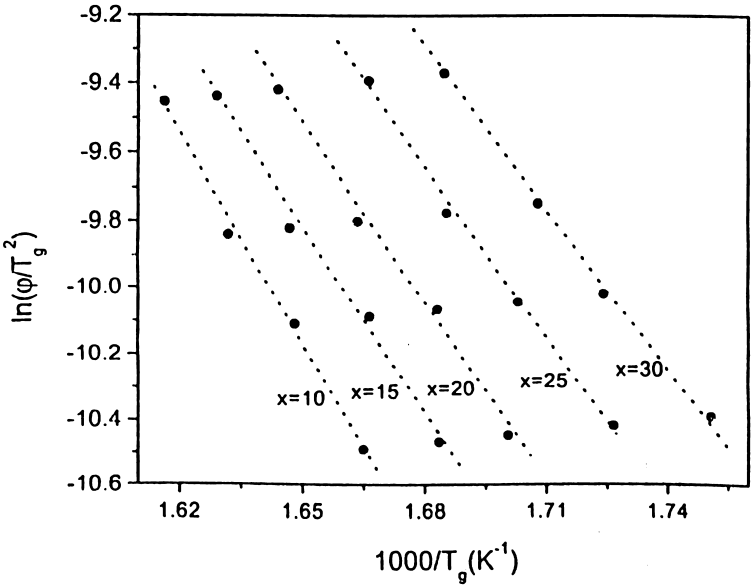

Figure 5.11: Kissinger's plots for $xV_2O_5.40CaO.(60- x)B_2O_3$ glasses.

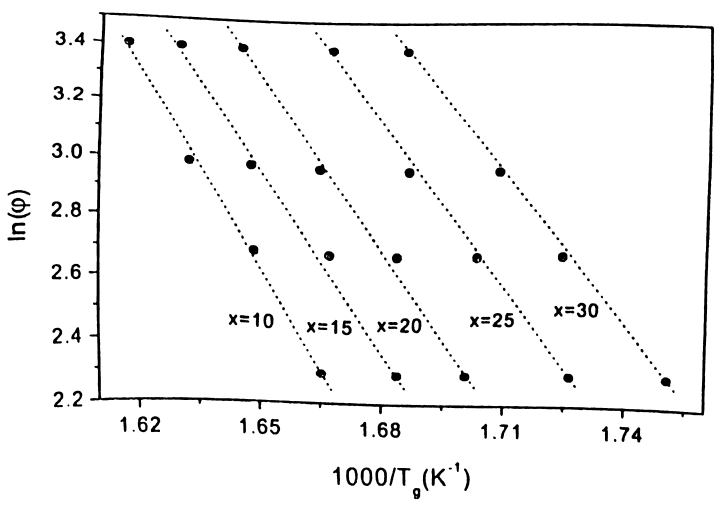

Figure 5.12: Thakor's plots for $xV_2O_5.40CaO.(60- x)B_2O_3$ glasses.

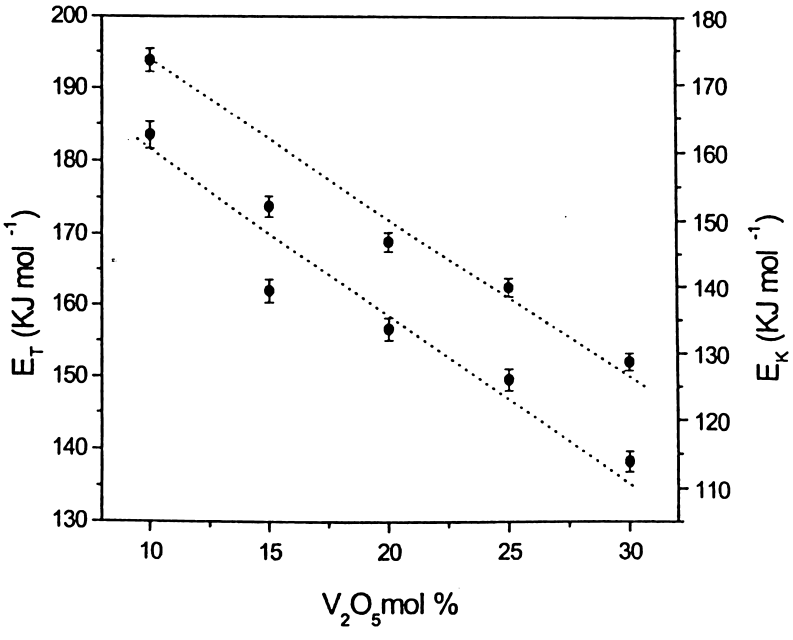

Figure 5.13: Activation energy of glass transition based on Kissinger's and Thakor's method for various compositions of V_2O_5-CaO-B_2O_3 glasses (Dotted lines shown merely connect adjacent data points).

The ΔC_p at T_g (table 5.3) of V_2O_5-CaO-B_2O_3 glasses is very small (similar to the behaviour observed in V_2O_5-CaO-P_2O_5 glasses). This low value of ΔC_p is a consequence of the weak glass transition exhibited by these glasses. These glasses can also be termed as "strong" in the context of Angell's classification [21]. It is however interesting to note that ΔC_p exhibits a composition dependence with a minimum value at correlated 20 mol % V_2O_5. One can argue that among the V_2O_5-CaO-B_2O_3 glasses studied in this chapter, the glass composition with 20 mol % V_2O_5 exhibited the minimum fragility. This observation suggests that the glass with 20 mol % V_2O_5 undergoes the least amount of configuration change while undergoing the glass transition. Such small values of heat capacity jump at T_g have been reported in other oxide glasses [166].

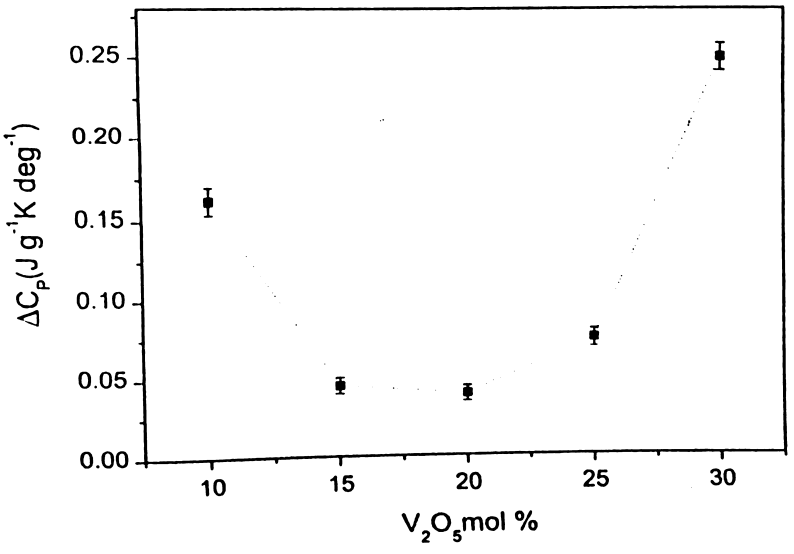

Figure 5.14: Excess heat capacity at glass transition of V_2O_5-CaO-B_2O_3 glasses (dotted line shown merely connects adjacent data points).

5.7. d.c. electrical conductivity

The d.c. electrical resistivity data of $xV_2O_5.40CaO.(60- x)B_2O_3$ with x = 10, 15, 20, 25, 30 was collected from 150 K to 480 K. The entire data was initially analysed on the basis of the Mott-Austin relation {equation (5.3)}. It has already been discussed that a plot of $\ln(\sigma T)$ versus T^{-1} is expected to be linear in order to satisfy equation (5.3). Figure 5.15 shows that a linear relationship exists in the plots of $\ln(\sigma T)$ versus T^{-1} for the conductivity data above room temperature. As the temperature is lowered, the data shows a deviation from linearity. This clearly shows that the conductivity data below room temperature cannot be fitted to equation 5.3. As done in the case of V_2O_5-SnO-TeO_2 and V_2O_5-CaO-P_2O_5 glasses, the high and low temperature conductivity data are analysed separately.

High temperature (SPH) region

Mott-Austin conductivity relation for small polaron hopping (SPH) mechanism in the high temperature region is given as,

$$\sigma T = \sigma_o e^{-\frac{W}{k_B T}} \qquad (5.3)$$

The activation energy W for conduction was calculated from the slope of the squares fits fit of ln(σT) versus 1000/T for all glasses. Density of metal ion sites N and average ion spacing R of the glasses were calculated using equation (3.4) and (3.5). The relevant data are presented in table (5.4). An increase in W with an increase in R is the general behavior expected on theoretical basis. The SPH conduction mechanism is either adiabatic SPH mechanism or non-adiabatic SPH mechanism depending on whether the value of polaron bandwidth (j) is greater or less than the parameter Φ. The polaron bandwidth j and Φ were calculated from the relation (1.13) and (1.15).

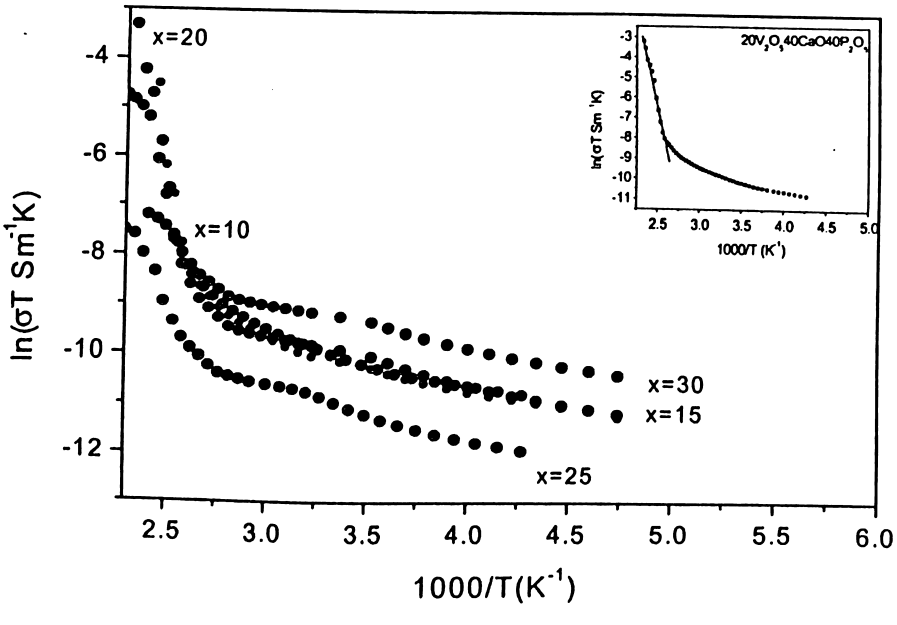

Figure 5.15: ln(σT) versus 1000/T plots for $xV_2O_5.40CaO.(60- x)B_2O_3$ glasses. Inset shows a typical fit of the data to relation (5.3)

The calculated values of j and Φ are shown in table 5.4. j values (calculated at 400 K) for V_2O_5-CaO-B_2O_3 glasses ranged from $1.3x10^{-6}$ eV to $4.2x10^{-6}$ eV and Φ value was

approximately 0.03 eV. Hence the polaron bandwidth j < Φ, for all V_2O_5-CaO-B_2O_3 glasses in high temperature regime. So, the high temperature conduction is attributed to non-adiabatic small polaron hopping mechanism. The non-adiabatic mobility for $xV_2O_5.40CaO.(60- x)B_2O_3$ glasses (table 5.5) was calculated using the relation (1.18). The non-adiabatic mobility for the glasses varied between 2.6 x 10^{-15} m^2V^{-1} sec^{-1} and 7.6 x 10^{-15} $m^2V^{-1}sec^{-1}$. The carrier concentration N_C was determined from the relation, $\sigma = N_C e\mu$, for the glasses using the non-adiabatic mobility and conductivity data.

Table 5.4: Density of metal ion sites N, average ion spacing R, conductivity σ (at 400K), polaron bandwidth j, the parameter Φ.

Composition (mol %) V_2O_5 : CaO :B_2O_3	W (eV)	N ($x10^{27}m^{-3}$)	R ($x10^{-10}m$)	σ (at 400K) ($x10^{-7}\Omega^{-1}m^{-1}$)	j(eV) (10^{-6})	Φ (eV)
10 : 40 : 50	0.21	4.4	6.1	5.9	4.2	0.03
15: 40 : 45	0.20	6.4	5.4	6.6	3.1	0.03
20 : 40 : 40	0.19	8.2	5.0	6.8	3.0	0.03
25 : 40 : 35	0.16	9.5	4.7	7.4	1.6	0.03
30 : 40 :3 0	0.15	10.6	4.5	9.1	1.3	0.03

Low temperature region

The deviation of the lower temperature conductivity data from the Arrhenius behaviour (figure 5.15) suggests that the conduction mechanism is different in lower temperature region. It was attempted to fit the low temperature conductivity data to the variable range hopping (VRH) conduction mechanism suggested by the Mott-Austin model. A linear plot of $\ln(\sigma T^{1/2})$ versus $T^{-1/4}$ signifies the occurrence of VRH conduction. Figure 5.16 shows the $\ln(\sigma T^{1/2})$ versus $T^{-1/4}$ plots for $xV_2O_5.40CaO.(60- x)B_2O_3$ glasses. The linearity observed in the plots in lower temperature region confirms that VRH conduction mechanism is dominant at these temperatures. Hence, the conductivity data in low temperature region was analyzed in the light of the Mott-Austin VRH mechanism. The

slope change in the plots shown in figure 5.16 was interpreted [73, 78] to be the signature of the conduction change from SPH to VRH. All V_2O_5-CaO-B_2O_3 glasses exhibited a cross-over from SPH to VRH conduction mechanism as the temperature was lowered. The parameters α and $N(E_F)$ were calculated from the slope and intercept values obtained from the linear fit to the low temperature ($T < T_R$) data using relations (1.21) and (1.22).

Table 5.5: Non-adiabatic mobility μ, charge carrier concentration N_C, density of states at Fermi energy $N(E_F)$, variable range hopping distance R_{VRH} and disorder energy W_d.

Compostn. (mol %) V_2O_5:CaO:B_2O_3	μ ($m^2V^{-1}sec^{-1}$) (10^{-15})	N_C (m^{-3}) (10^{26})	$N(E_F)$ ($m^{-3}eV^{-1}$) (10^{26})	R_{VRH} (m) (10^{-9})	W_d (eV)	αR_{VH}
10 : 40 : 50	7.7	4.8	0.42	4.9	0.05	3.7
15: 40 : 45	5.1	8.1	1.0	3.7	0.05	3.6
20 : 40 : 40	4.1	10.4	1.7	3.1	0.05	3.5
25 : 40 : 35	2.8	16.6	2.0	3.0	0.04	3.3
30 : 40 :3 0	2.6	22.2	2.2	2.9	0.04	3.2

From the calculated values of α and $N(E_F)$, the hopping distance R_{VRH} in VRH regime and hopping energy W_d were obtained using the relations (1.23) and (1.24). Table 5.5 lists the calculated disorder energy W_d, Mott parameters $N(E_F)$ and R_{VRH} for the $xV_2O_5.40CaO.(60\text{-}x)B_2O_3$ ($10 \leq x \leq 30$) glasses. Evaluation of the present data at 230 K gave αR_{VRH} values ranging between 3.2 to 3.7 and W_d values 0.04 eV to 0.05 eV, which showed that the $\alpha R_{VRH}>1$ criteria and $W_d \geq k_B T$ (0.019 eV at 230 K) were satisfied. Hence the conduction mechanism in V_2O_5-CaO-B_2O_3 glasses in the low temperature region is attributable to VRH.

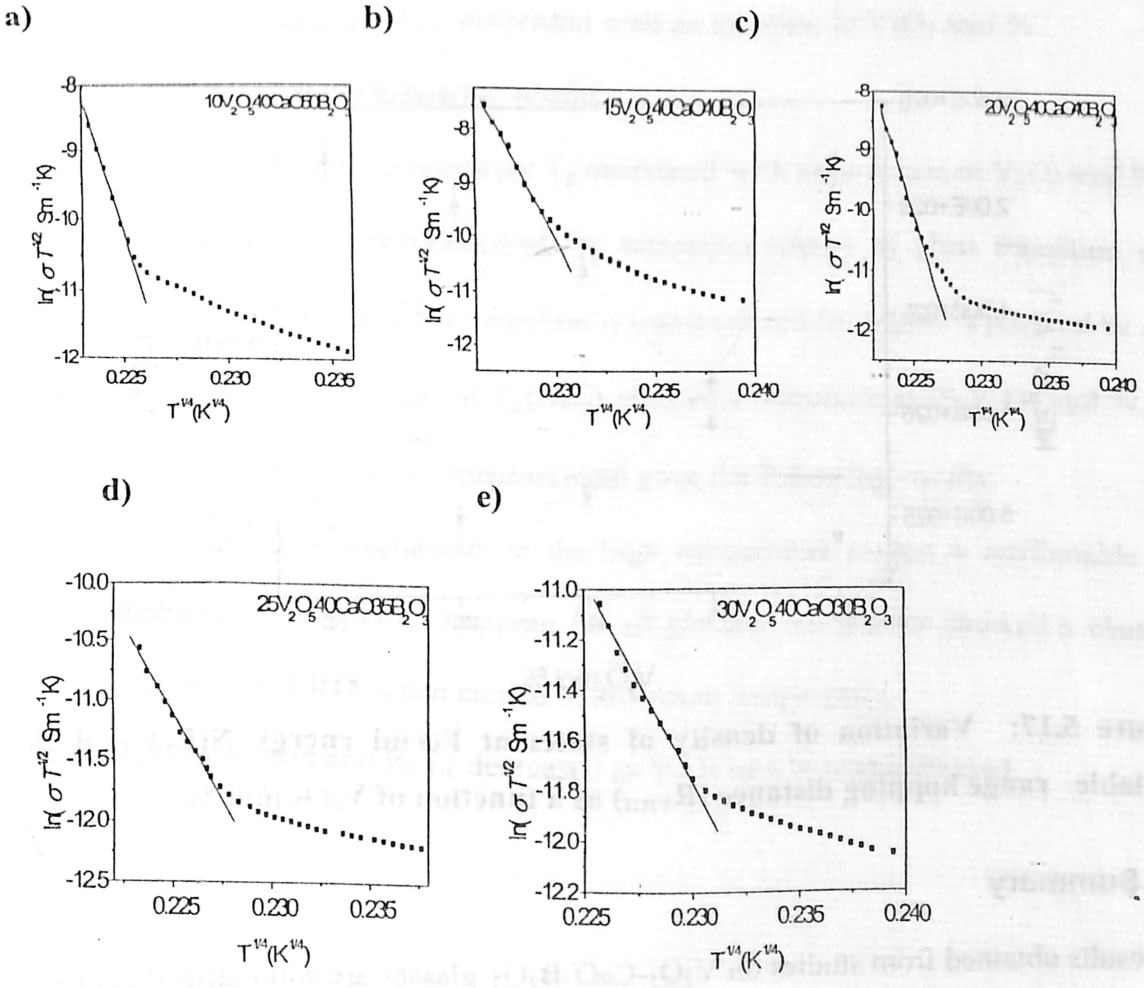

Figure 5.16: $\ln(\sigma T^{1/2})$ versus $T^{-1/4}$ plots for various compositions of $xV_2O_5.40CaO.(60\text{-}x)B_2O_3$ glasses (Several data points have been skipped in order to improve the clarity of figure. Solid lines are least-squares fit to $T > T_R$ and $T < T_R$ data).

Figure 5.17 shows that the variation in the density of states at Fermi level $N(E_F)$ and the average hopping distance in VRH regime R_{VRH} as a function of vanadium pentoxide concentration. It can be seen that $N(E_F)$ increases and R_{VRH} decreases with an increase in V_2O_5 mol %. A slope change $N(E_F)$ and R_{VRH} is observed at the composition x = 20 mol % V_2O_5. This indicates that the Mott parameters are sensitive to the majority charge carrier reversal phenomenon occurring in this glass system.

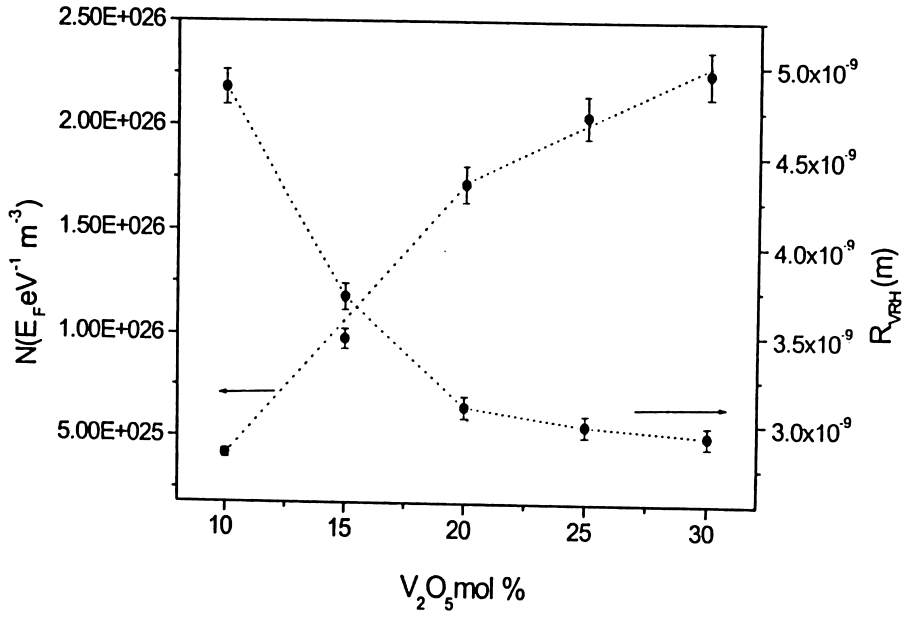

Figure 5.17: Variation of density of states at Fermi energy $N(E_F)$ and the variable range hopping distance (R_{VRH}) as a function of V_2O_5 mol %.

5.8. Summary

The results obtained from studies on V_2O_5-CaO-B_2O_3 glasses are summarized below:

I. The thermoelectric power measurements revealed the following aspects.

(i) Glasses with x = 10 and 15 mol % V_2O_5 showed p-type semiconductor behaviour and glasses with x = 25 and 30 mol % V_2O_5 showed n-type conduction. MCCR occurred at the glass composition with x = 20 V_2O_5 mol %.

(ii) All glasses exhibited weak Q dependence on temperature.

(iii) ΔE_s, the activation energy for thermoelectric power showed a subtle slope change at 20 mol % V_2O_5.

II. Density, microhardness and band gap measurements showed the following features:

(i) Density showed a maximum at 20 mol % V_2O_5 content.

(ii) Vicker's microhardness decreased as V_2O_5 mol % content increased.

(iii) The optical band gap E_{opt} decreased with an increase in V_2O_5 mol %.

III. DSC studies gave the following results:

(i) The glass transition temperature T_g decreased with an increase in V_2O_5 mol %.

(ii) The composition dependence of the activation energy of glass transition showed that the glass-supercooled transition is less hindered for higher V_2O_5 mol % .

(iii) The excess heat capacity at T_g (ΔC_p) showed a minimum at 20 V_2O_5 mol %.

IV. d.c. electrical conductivity measurement gave the following results:

(i) The conduction mechanism in the high temperature region is attributable to non adiabatic small polaron hopping for all glasses. All glasses showed a changeover from SPH to VRH when cooled below room temperature.

(ii) $N(E_F)$ increased and R_{VRH} decreased as V_2O_5 mol % was increased.

Chapter 6

Conclusions

Three semiconducting glass systems, which exhibited a changeover from n-type to p-type conduction behaviour with a systematic change in V_2O_5 mol % were taken up for study in this thesis work. V_2O_5-SnO-TeO_2 glass system investigated first is generally known to be n-type semiconductors. The glass composition with 18 mol % V_2O_5 in the $xV_2O_5.20SnO.(80-x)TeO_2$ series of glasses registered the highest positive Q value of +7 μVK^{-1}. The search for p-type conduction in V_2O_5-CaO-P_2O_5 glass system led to glasses with Q values ranging between +111 μVK^{-1} and –103 μVK^{-1} in the $xV_2O_5.40CaO.(60-x)P_2O_5$ $(10 \leq x \leq 30)$ series of glasses. The third glass system V_2O_5-CaO-B_2O_3 was chosen for two reasons – to look for carrier reversal phenomenon in vanadium borate systems and to verify the proposal that control of vanadium ion ratio could lead to a reversal of the carrier type. The $xV_2O_5.40CaO.(60-x)B_2O_3$ $(10 \leq x \leq 30)$ series of glasses with and without a reducing agent (abietic acid) were studied. n-type to p-type change was observed at x = 20 mol % V_2O_5 in this glass system with 0.2% abietic acid.

The physical properties of the three glass systems showed behaviour typical of the constituents. For example, the d.c. electrical conductivity of the V_2O_5-SnO-TeO_2 glasses was the highest, followed by the V_2O_5-CaO-P_2O_5 glasses and the V_2O_5-CaO-B_2O_3 glasses in that order. The density values of the three glass systems followed the same order. The optical band gap values decreased as one moved from vanadium-borate to vanadium-phosphate and then to vanadium-tellurite glasses. The same trend was shown by microhardness (VHN) indicating that the average bond strength of the glasses decreased when vanadium-borate is replaced by vanadium-phosphate and vanadium-tellurite.

Apart from the specific features arising due to the constitution of the individual glass system, the present studies revealed several features that were commonly observed in all the three glass systems at specific compositions.

The activation energy for thermal conduction ΔE_s, of the three glass systems (figure 3.5, 4.4, 5.5) showed a perceptible slope change at the composition at which the majority charge carrier reversal was observed. It appears that the thermal conduction is facilitated in n-type glasses more than the p-type glasses. In all the three glass systems, the distance between vanadium ions R decreased and the number of metal ion sites N increased when V_2O_5 content was increased, supporting the argument that TEP depends strongly on the site concentration and separation. Analysis of the electrical conductivity on the basis of the Mott-Austin model revealed that all glasses in the three systems showed SPH conduction mechanism at high temperatures and VRH conduction mechanism at low temperatures. The Mott parameters, density of states at fermi energy $N(E_F)$ and variable range hopping distance R_{VRH} showed a slope change at the composition at which MCCR was observed in V_2O_5-SnO-TeO_2, V_2O_5-CaO-P_2O_5 and V_2O_5-CaO-B_2O_3 glass systems (figures 3.19, 4.17 and 5.17). These observations suggest that ΔE_s, $N(E_F)$ and R_{VRH} are sensitive to the MCCR phenomenon occurring in these glasses. This observation is not surprising since the MCCR accompanies a change in the vanadium ion ratio. Since these parameters are sensitive to the vanadium ion ratio, they also carry the signature of the MCCR phenomenon.

What is indeed surprising is the consistent anomaly shown by non-electronic properties such as the excess heat capacity at T_g (ΔC_P) and microhardness at the MCCR composition by all the three glass systems. It has to be pointed out that slope change in

the microhardness at the MCCR composition in the three glass systems is not that well pronounced. This subtle slope change in the microhardness value at the MCCR composition suggests a change in the average bond strength of the glass at this composition. Similar behaviour has been observed in the microhardness of Pb modified Ge-Se and Ge-Se-Te [167] glasses.

ΔC_P on the other hand, shows a much more prominent anomaly at the MCCR composition. Since ΔC_P could be correlated with the fragility of the glass, this observation is quite interesting. In the case of V_2O_5-SnO-TeO_2 glasses, the fragility increases sharply after the MCCR composition (figure 3.15). In the case of V_2O_5-CaO-P_2O_5, (figure 4.13) and V_2O_5-CaO-B_2O_3 (figure 5.14) glasses, the MCCR glass composition has the minimum fragility. The abrupt change in the fragility of the glass at the MCCR composition suggests that the MCCR composition undergoes minimal configuration change at glass transition.

In this thesis work, an attempt has been made to systematically study a few physical properties of certain V_2O_5 based glasses exhibiting carrier reversal phenomenon. The strong dependence of the electrical properties on the ratio of vanadium ions is an interesting out come of this research work. The work on V_2O_5-CaO-B_2O_3 glasses with small amounts of abietic acid showed that the electrical properties of these glasses could be tailored by controlling the vanadium ion ratio. Use of reducing agents in the preparation of high electrical conductivity glasses (such as glasses containing TeO_2) could yield glasses suitable for gas sensing and thermoelectric device applications. Preparation of p- and n-type thin films of these glasses would be useful in view of their practical application in semiconductor devices.

References

1. S.R. Elliot, Physics of Amorphous Materials, Longman, London, 1984.
2. Jerzy Zarzycki, Materials Science and Technology **9**, Weinheim, New York.
3. R. Zallen, The Physics of Amorphous Solids, John Wiley, New York, 1983.
4. D. Alder, Amorphous Semiconductors, CRC, Butterworths, London, 1971.
5. A.F. Ioffe and A.R. Regel, Prog. Semiconductors **4**, 237 (1960).
6. P.L. Bayton, H. Rawson, J.E. Stanworth, J. Electrochem. Soc. **104**, 237 (1957).
7. T.N. Kennedy and J.D. Mackenzie, Phys. Chem. Glasses **8**, 169 (1967).
8. A. Mansingh and A. Dhawan, J. Phys. C. Solid State Phys. **11**, 3439 (1978).
9. M. Sayer and A. Mansingh, Phys. Rev. B **6**, 4629 (1972).
10. A. Ghosh, Phys. Rev. B **42**, 5665 (1990).
11. C.H. Chung, J.D. Mackenzie and L Murawski, Rev. Chim. Miner. **16**, 308 (1979).
12. H.N. Ritland, J. Am. Ceram. Soc. **34**, 370 (1954).
13. H. Mori, J. Igarashi and H. Sakata, J. Ceram. Soc. Jpn. **101**, 1315 (1993).
14. N.F. Mott, Adv. Phys. **16**, 49 (1967).
15. N.F. Mott, J. Non-Cryst. Solids **1**, 1 (1968).
16. I.A. Gohar, Y.M. Moustafa, A.A. Megahed & E. Mansour, Phys. Chem. Glasses **39**, 56 (1998).
17. N.F. Mott and E.A Davis, Electronic Processes in Non-Crystalline Materials, OUP, 1979.
18. A. K. Varshneya, Fundamentals of Inorganic Glasses, Academic Press, New York, 1993.
19. C. Kittel, Introduction to Solid State Physics 7 ed., John Wiley, Singapore, 1996.
20. M.W. Zemansky and R.H. Dittan, Heat and Thermodynamics 6 ed., McGraw Hill, Auckland, 1981.
21. C.A. Angell, J. Non-Cryst. Solids **73**, 1 (1985).
22. G. Adam and J. H. Gibbs, J. Chem. Phys. **43**, 139 (1965).
23. C.A. Angell, W. Sichina, Ann. N.Y. Acad. Sci. **279**, 53 (1976).

24. A.E Owen, in Electronic and Structural Properties of Amorphous Conductors, eds. P. G. LeComber and J. Mort, Academic, New York, 1973.
25. A. Hruby, Czech. J. Phys. B **22,** 1187 (1972).
26. G.W. Scherer, J. Non-Cryst. Solids **123**, 75 (1990).
27. M.H. Cohen and D. Turnbull, J. Chem. Phys. **52**, 3038 (1970).
28. M.H. Cohen and D. Turnbull, J. Chem. Phys. **31**, 1164 (1959).
29. A. Feltz, Amorphous Inorganic Materials and Glasses, VCH, New York, 1993.
30. S.R. Elliot, Nature **354,** 445 (1991).
31. S. Sugai, Phys. Rev. B **35,** 1345 (1987).
32. P.M. Bridenbaugh, G.P. Espinosa, J.E. Grifiths, J.C. Phillips and J.P. Remeika, Phys. Rev. B **20**, 4140 (1979).
33. J. Wong and C.A Angell, Glasses: Structure by Spectroscopy, Marcel Dekker, New York, 1979.
34. U. Hoppe, R. Kranold and E. Gattef, Solid State Comm.**108**, 71 (1998).
35. James E. Shelby, Introduction to Glass Science and Technology, RSC, 1997.
36. W. Vogel, Chemistry of Glasses, Amer. Ceram. Soc., 1985.
37. J. Krogh-Moe, J. Non-Cryst. Solids **1**, 269 (1969).
38. D.L.Griscom, Mat. Sci. Res. **12**, 11 (1977).
39. H.M. Kritz and P.J. Bray, J. Non-Cryst. Solids **6**, 27 (1971).
40. A.H. Silver and P.J. Bray, J. Chem. Phys. **29**, 984 (1958).
41. A.C. Wright, C.A. Yarker, P.A.V Johnson, R.N. Sinclair, J. Non-Cryst. Solids **76**, 333 (1985).
42. S.R. Elliot, J. Phys. Condens. Matter **4**, 7661 (1992).
43. S.R. Elliot, Phys. Rev. Lett. **67**, 711 (1991).
44. D.L. Price, S.C. Moss, R. Reijers, M.L. Saboungi and S. Susman, J. Phys.C. Solid State Phys. **21**, L1069 (1989).
45. L.E. Busse, Phys. Rev. B **29**, 3639 (1984).
46. K. Tanaka, Philos. Mag. Lett. **57**, 183 (1988).
47. S.R Elliot, Phys. Condens. Matter **4**, 7661 (1992).
48. R.J. Dejus, S. Susman, K.J. Volin and D.L. Price, J. Non-Cryst. Solids **106,** 34 (1988).

49. A.C. Wright, R.N. Sinclair, A.J. Leadbetter, J. Non-Cryst. Solids.**71**, 295 (1985).
50. S.C. Moss and D.L. Price, in Physics of Disordered Materials, ed. D. Alder, H. Fritzche, and S.R. Ovshinsky, Plenum, New York, 77 (1985).
51. S. R. Elliot, Phys. Rev. B **51** (13), 8599 (1995).
52. L.E. Busse and S.R. Nagel, Phys. Rev. Lett. **47**, 1848 (1981).
53. W. H. Zachariasen, J. Chem. Soc. **54**, 3841-3851 (1932).
54. B.E. Warren, J. Am. Ceram. Soc. **17**, 249 (1932).
55. R.T. Sanderson, Chemical Bonds and Bond Energy, Academic Press, New York, 1976.
56. A.A Lebedev, Trans.Opt. Inst. Petrograd **10**, 2 (1910).
57. N.N. Valenkov and E.A. Porai-Koshits, Z. Krist. **95**, 195 (1936).
58. N.J. Kredl, Adv. In Fusion and Proc. of Glass III, eds. A.K. Varshneya, D.F. Bickford and P. P. Bihunaik, Ceramic Transactions **29**, 175-189 (1993).
59. A.R Cooper, J. Non-Cryst. Solids **49**, 1-17 (1982).
60. K.H. Sun, J. Am. Ceram. Soc. **30**, 277 (1947).
61. R.M White, J. Non-Cryst. Solids **16**, 387 (1974).
62. G. Lucovsky and T.M Hayes, in Amorphous Semiconductors, ed. M.H Brodskky, Springer Verlag, Berlin, 1985.
63. P.W Anderson, Phys. Rev. B **109**, 1492 (1958).
64. M.H.Cohen, H. Fritzsche and S.R.Ovshinsky, Phys. Rev. Lett. **22**, 1065 (1969).
65. E. A. Davis and N.F. Mott, Philos. Mag. **22**, 903 (1970).
66. J. M. Marshall and A.E. Owen, Philos. Mag. **24**, 1281 (1971).
67. P. Nagels, in Amorphous Semiconductors, 2 ed., ed. M.H. Brodsky, Springer Verlag, New York, 1985.
68. T. Holstein, Am. Phys. N. Y **8**, 34 (1959).
69. L. Murawski, C.H. Chung and J.D. Mackenzie, J. Non-Cryst. Solids **32**, 91 (1979).
70. H. Mori and H. Sakata, J. Ceram. Soc. Jpn. **102**, 560 (1994).
71. H. Mori, T. Kitami and H. Sakata, J. Non-Cryst. Solids **168**, 157 (1994).
72. H. Mori, K. Gotoh and H. Sakata, J. Non-Cryst. Solids **183**, 122 (1995).
73. S.R. Nagel and J. Tauc, Phys. Rev. Lett. **35**, 380 (1975).

74. G.E. Pike, Phys. Rev. B **6**, 1572 (1972).
75. S.R. Elliot, Phil. Mag. **36**, 1291 (1977).
76. S.R. Elliot, Adv. Phys. **36**, 135 (1987).
77. M. Pollak and T.H. Geballe, Phys. Rev.B **122**, 1742 (1961).
78. I. Austin and N.F. Mott, J. Adv. Phys. **18**, 41 (1969).
79. K. Shimakawa, Phil. Mag. B **46**, 123 (1982).
80. A.R. Long, Adv. Phys. **34**, 553 (1982).
81. R.R Heikes, A.A Maradudin and R.C. Miller, Ann. Phys. Paris **8**, 733 (1963).
82. R.R Heikes, Transition metal Compounds: Transport and Magnetic Properties, ed. E. R Schatz, Gordon and Breach, New York, 1964.
83. G.H. Jonker and S. Van Houten, in Halbleiterprobleme, ed. F. Saurer, Vieweg Braunschweig, Germany **6**, 118 (1961).
84. B.T. Kolomiec, Vitreous Semiconductors, Phys. Status Solidi **7**, 359 (1964).
85. J.C. Male, Brit. J. Appl. Phys. **18**, 1543 (1967).
86. L. Friedman, J. Non-Cryst. Solids **6**, 329 (1971).
87. N. Toghe, H. Matsuo and T. Minami, J. Non-Cryst. Solids 95 - **96**, 809 (1987).
88. N. Toghe, T. Minami, Y. Yamamoto and M. Tanaka, J. Non-Cryst. Solids 37, 23 (1980).
89. N. Toghe, T. Minami,Y. Yamamoto and M Tanaka, J. Appl. Phys. **51**,1048 (1980).
90. L. Tichy, H. Ticha and A.Triska, Solid State Comm. **53**, 399 (1985).
91. T. Alersma and J.D. Mackenzie, J. Chem. Phys. **47**, 1406 (1967).
92. D. Weaire and M.F. Thorpe, Phys. Rev. B **4**, 2508, 3518 (1971).
93. Y. Lee and K.B. Lee, J. New Phys. **26**, 259 (1988).
94. Y.M. Moustafa, I.A. Gohar, A.A. Megahed and E. Mansour, Phys. Chem. Glasses **38**, 92 (1997).
95. J. Tauc, in Amorphous and Liquid Semiconductors, ed. J. Tauc, Plenum Press, 1974.
96. J. Tauc, Mat. Res. Bull. 5, 721 (1970).
97. J.D. Dow and D. Redfield, Phys. Rev. B **5**, 5949 (1972).
98. R.A. Street, Solid State Comm. **24**, 363 (1977).

99. Ph.D thesis of A. Srinivasan, 1991, IISc Bangalore (unpublished).
100. J.S. Jen, M. R. Kalinowski, J. Non Cryst Solids **38/39**, 21 (1980).
101. H. Doweidar, Phys. Chem. Glasses **39**, 286 (1998).
102. A.Cousen and W.E.S. Turner,Glastech. Ber. **6**, 393 (1928).
103. R. Jabra, J. Pelous and J. Phalippou, J. Non-Cryst. Solids. **37**, 349 (1980).
104. M. Yamane and J.D. Mackenzie, J. Non-Cryst. Solids **15**, 153-64 (1974).
105. A. Petzold, F. G. Withsmann and H. Von Kampiz, Glasteck Ber. **43**, 56 (1961).
106. J.E. Neely and J.D. Mackenzie, J. Mater. Sci. **3**, 603 (1968).
107. A.R. Hilton, C.E. Jones and M. Baru, Phys. Chem.Glasses **7**, 105 (1966).
108. H. Mori and H. Sakata, IUMRS, ICEM 94 Symp., Proc. Vol. 3, Materials Research Society-Taiwan.
109. Nevill Mott, Conduction in Non-Crystalline Materials, Clarendon Press, Oxford, 1987.
110. M.H. Brodsky, Amorphous Semiconductors 2 ed., Springer-Verlag, New York, 1985.
111. H. Mori and H. Sakata, J. Mater. Sci. **30**, 4389 (1995).
112. A. Srinivasan and K. Nandakumar, Phys. Chem. Glasses **40**, 40 (1999).
113. M.K. Rabinal, N. Ramesh Rao, K.S. Sangunni and E.S.R. Gopal, Phil. Mag. B **70**, 89 (1994).
114. S.H. Thomas and J. Philip, Phys. Stat. Sol. (b) **200**, 359 (1997).
115. B. Vaidhyanathan, S. Murugavel, S. Asokan and K.J. Rao, J. Phys. Chem. B **101**, 9717 (1997).
116. A. Giridhar, P.S.L. Narasimham and Sudha Mahadevan, J. Non-Cryst. Solids **43**, 29 (1981).
117. E.S. Watson, M.J.O'Neil, J.Justin and N. Brener, Anal. Chem. **36**, 1233 (1964).
118. J. Wolny, J. Soltys and R. Kokoszka, J. Non-Cryst. Solids **91**, 209 (1987).
119. N.P. Bansal and R.H. Doremus, J. Thermal Analysis **29**, 115 (1984).

120. B. Indrajit Sharma, A.K. Pattanaik and A. Srinivasan, Phys. Chem. Glasses **43**, 12 (2002)

121. L. Kashif, A.A. Soliman and A.M. Sanad, Phys. Chem. Glasses **39**, 195 (1998).

122. T. Komatsu, R. Ike, R. Sato and K. Matusita, Phys. Chem. Glasses **36**, 216 (1995).

123. Ph.D thesis of P.C. Paul, 1992, NEHU (unpublished)

124. T. Szorenyi, K. Bali and I. Hevesi, J. Non-Crys. Solids **70**, 297 (1985).

125. H. Farouk, F.M. Ezz Eldin, H. Farhan, H.A. El-Batal and I. Kashif, Physics and Chemistry of Glasses **35**, 207 (1994).

126. D. Sudhakar Rao and P.P. Karat, Physics and Chemistry of Glasses **35**, 124 (1994).

127. Y.C. Ratnakaram and A.Viswanadha Reddy, Phys. Chem. Glasses 41, 121 (2000).

128. G.R. Moridi and C.A. Hogarth, In proc. VII Intl. Conf., amorphous and liquid semiconductors, ed. W.E. Spear, Edinburgh, (668)1977,

129. S.K.J. Al-Ani, C.A.Hogarth and R. Malawany, J. Mater. Sci. **20**, 661 (1985).

130. D.M. Sclapp, Phys. Chem. Glasses **6**, 168 (1965).

131. K.W. Peter, J. Non-Cryst. Solids. **5**, 103 (1970).

132. D.K. Schroder, Semiconductor material and device characterization, John Wiley, New York 1990.

133. L.P. Hunter, Hand book of Semiconductor Electronics, McGraw Hill, New York, 1962.

134. A.C. Mellissions, Experiments in Modern Physics, Academic Press, New York 1966.

135. W. Shockley, Electrons and Holes, DVN, New York, 1950.

136. J. Lindmayer and C. Y. Wriegley, Fundamental of Semiconductor Devices, East West Press, 1971

137. D.J. Grifith, Introduction to electrodynamics 2 ed., New Delhi, Prentice Hall, 1995.

138. A.K Pattanaik, C. Borgohain and A. Srinivasan, Ind. J. Phys.**74A**, 307 (2000).

139. R.C. Richardson and E.N Smith, Experimental Techniques in Condensed Matter Physics at Low Temperatures, Addison-Wesley, New York, 1988.
140. J.D. Mackenzie, J. Am. Ceram. Soc. **47**, 211 (1964).
141. H. Mori and H. Sakata, J. Ceram. Soc. Japn. **101**, 1351 (1993).
142. P.A.V. Johnson, A.C. Wright, C.A. Yarker, R.N. Sinclair, J. Non-Cryst. Solids **81**, 163 (1986).
143. Neena Chopra and Abhai Mansingh, J. Non-Cryst. Solids **146**, 261 (1992).
144. N. Ichinose and Y. Nakai, J. Non-Cryst. Solids **203**, 353 (1996).
145. F.C. Eversteijn, J.M. Stevels and H.I. Waterman, Phys. Chem. Glasses **1**, 123 (1960).
146. N. Mochida, K. Takahashi, K. Nakada, and S. Shibusawa, Yogyo-Kyokai-Shi **88**, 583 (1980).
147. H. Hirashima and F. Tanaka Seram. Ronbunshi-Shi **97**, 1150 (1990).
148. H. Mori, T. Kitami and H. Sakata, J. Ceram. Soc. Jpn. **101**, 347 (1993).
149. D. Turbull, in Solid State Physics, Vol.3 ed. F. Seitz and D. Turnbull, 226-306, Academic Press, New York, 1956.
150. H.B. Qiu, H. Mori, H. Sakata and T. Hirayama, J. Ceram. Soc. Jpn. **103**, 32 (1994).
151. H.R. Killias, Phys. Letter **20**, 5-6 (1966).
152. I.G. Austin and E.S. Garbert, Electronic and Structural Properties of Amorphous Semiconductors, ed. P.G. Le Comber and J. Mort, Academic Press, 393-408 (1973).
153. N.F. Mott and E.A. Davis, Electronic Processes in Non-crystalline Materials, Clarendon Press, Oxford 1979.
154. M. Amano, H. Sakata, K. Tanaka and T. Hirayama, J. Ceram. Soc. Jpn. **102**, 424 (1994).
155. H. Sakata, M. Amano, T. Ishiguro and T. Hirayama, Ceram. Soc. Jpn. **100**, 1398 (1992).
156. B. Vaidhyanathan, S. Murugavel, S. Asokan and K.J. Rao, J. Phys. Chem. B **101**, 9717 (1997).
157. R.L Reed, I. Weber and B.S. Gottfried, Ind. Eng. Chem. Fundam. **4**, 38 (1965).

158. N. Toghe, Y. Yamamoto, T. Minami and M. Tanaka, Appl. Phys. Lett. **34**, 640 (1979).

159. S. Murugavel and S. Asokan, Physical Review B **58**, 4449 (1998).

160. M. Imoka, Advances in Glass Technology, New York, Plenum Press, 149, 164 (1962).

161. L.A. Grechanik, N.U. Petrovykh and V.G. Karpechenko, Soviet Phys. Solid St. **2**, 1908 (1961).

162. J. Tauc, Czech. J. Phys.**5**, 297 (1955).

163. R. Muncaster and S. Parke, J. Non-Cryst. Solids **24**, 399 (1977).

164. S. Khasa, V.P. Seth, S.K. Gupta, R. Murali Krishna, Phys. Chem. Glasses, **40**, 269 (1999).

165. M. Tatsumisago, B.L. Halfpap, J.L. Green, S.M. Lindsay and C.A. Angell, Phys. Rev. Lett. **64**, 1549 (1990).

166. U.E. Schnaus, C.T. Moynihan, R.W. Gammon and P.B. Macedo, Phys. Chem. Glasses **11**, 213 (1970).

167.A.K. Pattanaik and A.Srinivasan, (unpublished data).

Research papers published

1. Non isothermal properties of V_2O_5-SnO-TeO_2 glasses exhibiting majority charge carrier reversal,
   B. Indrajit Sharma, A.K. Pattanaik and A. Srinivasan,
   Physics and Chemistry of Glasses **43** (1), 12-15 (2002).

2. Low temperature dc electrical conductivity of V_2O_5-SnO-TeO_2 glasses exhibiting majority charge carrier reversal,
   B. Indrajit Sharma and A. Srinivasan,
   Physica Status Solidi b **229**(3), 1405–1411 (2002).

3. Thermoelectric power and Hall coefficient of V_2O_5-SnO-TeO_2 glasses exhibiting majority charge carrier reversal,
   B. Indrajit Sharma, A.K.Pattanaik and A. Srinivasan
   Proc. 6th ATPC, 8-11 October, 2001 (Gauhati University, India)